UNIVERSITY OF OKLAHOMA

GRADUATE COLLEGE

OKLAHOMA EARTHQUAKES AND THEIR EFFECTS ON HIGHWAY BRIDGES

A THESIS

SUBMITTED TO THE GRADUATE FACULTY

in partial fulfillment of the requirements for the

Degree of

MASTER OF SCIENCE

By

SAMANTHA K. HEINRICH
Norman, Oklahoma
2017

OKLAHOMA EARTHQUAKES AND
THEIR EFFECTS ON HIGHWAY BRIDGES

A THESIS APPROVED FOR THE
SCHOOL OF CIVIL ENGINEERING AND ENVIRONMENTAL SCIENCE

BY

Dr. P. S. Harvey Jr., Chair

Dr. K. K. Muraleetharan

Dr. C. C. E. Ramseyer

To my amazing parents who always have supported my academic endeavours

Acknowledgements

I would like to thank my adviser Dr. Philip S. Harvey Jr. for coming to me two years ago and asking if I wanted to be part of a project for the Oklahoma Department of Transportation (ODOT). I doubt that I would have found a direction for my research without him. Thank you for always pushing me to go out of my comfort zone to present this research at various venues.

I would also like to thank my thesis committee Dr. Kanthasamy K. Muraleetharan and Dr. Christopher C. E. Ramseyer. Their additional input has been invaluable.

Also, I would like to thank the Oklahoma Department of Transportation (ODOT), in particular Mr. Walter L. Peters for providing access to information and as-built plans for the bridge inventory. Financial support from ODOT under award no. EC-1609 is gratefully acknowledged. Any opinions, findings, and conclusions or recommendations expressed in this material are those of the author and do not necessarily reflect the views of ODOT.

Additionally, I would like to thank our partners on the ODOT project, Infrastructure Engineering, Inc. and Kleinfelder. Working with them has provided me a great experience in the real world of engineering and taught me what it means to be part of a team.

I would also like to thank my friends from the organizations I have participated in college, Alpha Gamma Delta, Sigma Alpha Iota, and the Pride of Oklahoma, to name a few. I would not have made it through college without your friendships. Thank you for always listening to my complaints and celebrating my successes with me.

Finally, I would like to thank my parents for their continuous support throughout the years. They have always encouraged my academic pursuits and I'm so thankful they didn't complain when I went to a college so far from home.

Contents

List of Figures

List of Tables

Abstract

Oklahoma is presently experiencing a higher rate of earthquake activity than historically observed. Historical data on earthquake-induced damage to Oklahoma bridges is limited, so the Oklahoma Department of Transportation (ODOT) is concerned about their bridges. The first part of this research develops smart inspection radii for ODOT. These radii incorporate both the demand on and capacity of Oklahoma bridges. Demand is quantified by the ground-motion intensity, in this case spectral acceleration at a period of 1.0 s (S_1). Capacity is characterized by HAZUS fragility curves for bridges. Then, Oklahoma ground motions are compared to current attenuation models. Current models tend to over predict Oklahoma shaking levels, so a bias factor was calibrated to better represent Oklahoma earthquake attenuation. This is followed by performing a seismic response analysis for the Interstate 35 bridge over the Cimarron River located approximately 40 miles north of Oklahoma City in Logan County, Oklahoma. The results from this study can also be used to verify and adjust the fragility curve parameters needed for the development of ShakeCast–OK. Seismic response analysis has shown that the potential for structural damage is low under the considered loading conditions. Finally, ShakeCast–OK is developed. This real-time program sends notifications to ODOT indicating which bridges to inspect after an earthquake. This saves ODOT time and money by reducing the number of unnecessary inspections.

Chapter 1

Introduction

1.1 Overview

In this chapter seismicity in Oklahoma will be introduced. Then, a plan for improving the Oklahoma Department of Transportation's (ODOT) post bridge inspection protocol will be provided. Finally, established methods for developing bridge fragility curves will be discussed.

1.2 Seismicity in Oklahoma

Since 2009, there has been a dramatic increase in the number of earthquakes in Oklahoma (Fig. 1.1). Oklahoma and the surrounding region have not historically experienced earthquakes of this magnitude nor at the rate currently observed (McGarr et al., 2015) (Fig. 1.2). Studies such as by Keranen et al. (2013) have linked the increased rate of seismic activity since 2009 to wastewater injection in disposal wells. The only identified source of natural (tectonic) earthquakes in this region is the Meers fault in southwest Oklahoma, as reflected in the U. S. Geological Survey (USGS) national seismic hazard maps (Petersen et al., 2014) and accordingly the mapped design ground motion data provided by the *2009 AASHTO Guide Specifications for LRFD Seismic Bridge Design* (AASHTO, 2009). In 2016, the USGS made an effort incorporate non-tectonic earthquakes (or "induced seismicity") into the national seismic hazard model (Petersen et al.,

(a)

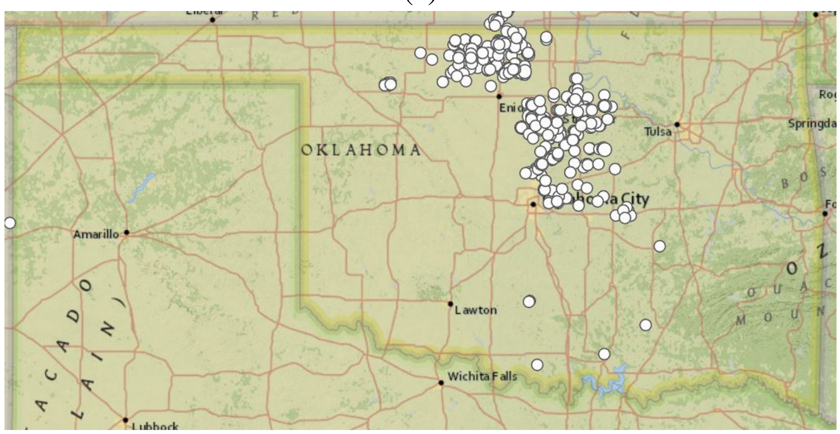

(b)

Figure 1.1: Magnitude 3.0 and larger earthquakes in Oklahoma in (a) 2002 ($\approx$ 4) and (b) 2014 ($\approx$ 585) (USGS, 2015b).

2016), but these are not reflected in seismic design provisions. Therefore, concern has arisen about how Oklahoma's infrastructure will handle the increased seismic demand. In particular, ODOT is concerned about their bridges' response to earthquakes and the potential for damage.

1.2.1 Significant Oklahoma Earthquakes

Over the past decade (2008–2017), Oklahoma experienced over 80 magnitude 4.0 (M4.0) or larger events, including four M5.0 or larger events. The first of these

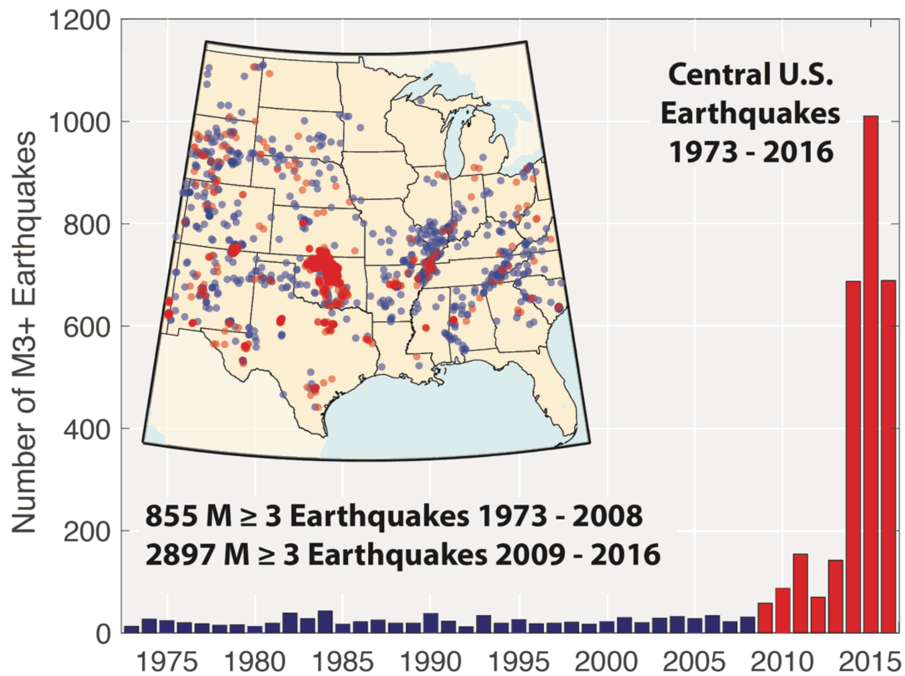

Figure 1.2: Annual Central U.S. Earthquakes 1973-2016 (USGS, 2017a).

events was a M5.7* earthquake that occurred on 6 November 2011, near Prague, Oklahoma (USGS, 2016c). Several years passed before the next significant event, the 13 February 2016, M5.1 earthquake near Fairview, Oklahoma (USGS, 2016b). The largest earthquake Oklahoma has experienced to date would come later that year. At 12:02:44 Coordinated Universal Time (UTC) on 3 September 2016, a M5.8 earthquake struck 15 km northwest of Pawnee, Oklahoma. The event was triggered by strike-slip faulting within the interior of the North America plate (USGS, 2016d), at a focal depth of 5.6 km. A fourth large event (M5.0) occurred on 7 November 2016 near Cushing, Oklahoma (USGS, 2016a). These M5.0 and larger events were felt in the surrounding states, caused damage to residential structures, and resulted in minor injuries (Taylor et al., 2017).

*Prior to 7 September 2016, USGS estimated the 6 November 2011 Prague, Oklahoma earthquake to be M5.6, but updated the estimate following the 3 September 2016 Pawnee, Oklahoma earthquake (USGS, 2016f). Hereinafter, M5.7 will be used when referring to this event, except for in Chapter 2.

1.2.2 History of ODOT's Post-Earthquake Inspection Protocol

When the earthquake activity began to increase, ODOT needed to determine when and how to inspect their bridges after an earthquake. Their initial response was to inspect after every earthquake with a magnitude greater than 3.0. However, as time went on, they found this to be overly conservative.

On 23 January 2015, ODOT changed the protocol to dictate that bridges must be inspected within a 5 mile radius for earthquakes with magnitudes from 4.0 to 4.9, within a 25 mile radius for earthquakes with magnitudes from 5.0 to 5.5, and within a 50 mile radius for earthquakes with magnitudes greater than 5.5. If damage was found within those radii, the inspection radius was expanded by 5 miles (W. L. Peters, personal communication, February 2017).

This inspection protocol resulted in inspections for over 30 earthquakes in 2015, yet no earthquake-related damage to the bridges was found. ODOT felt even this was too much and wanted to establish an evidence-based, rigorous procedure, so in 2015 they hired a team of consultants led by Infrastructure Engineers, Inc. to revise their post-earthquake bridge inspection protocol. This contract consisted of two phases: Phase I, which would establish an interim post-earthquake bridge inspection protocol (Chapter 2), and Phase II, which would develop ShakeCast-OK (Chapter 5). On 1 April 2016, the interim protocol was implemented. ShakeCast-OK will become operational in 2017.

1.2.3 Improving ODOT's Inspection Protocol

California is a leader in earthquake response, so their post-earthquake protocol was a reasonable place to start to find a solution for Oklahoma bridges. After an earthquake in California, the California Department of Transportation (Caltrans) sends prioritized bridge inspection lists to their response teams, optimizing the bridge inspection process and ensuring that the bridges most likely to be damaged are inspected first.

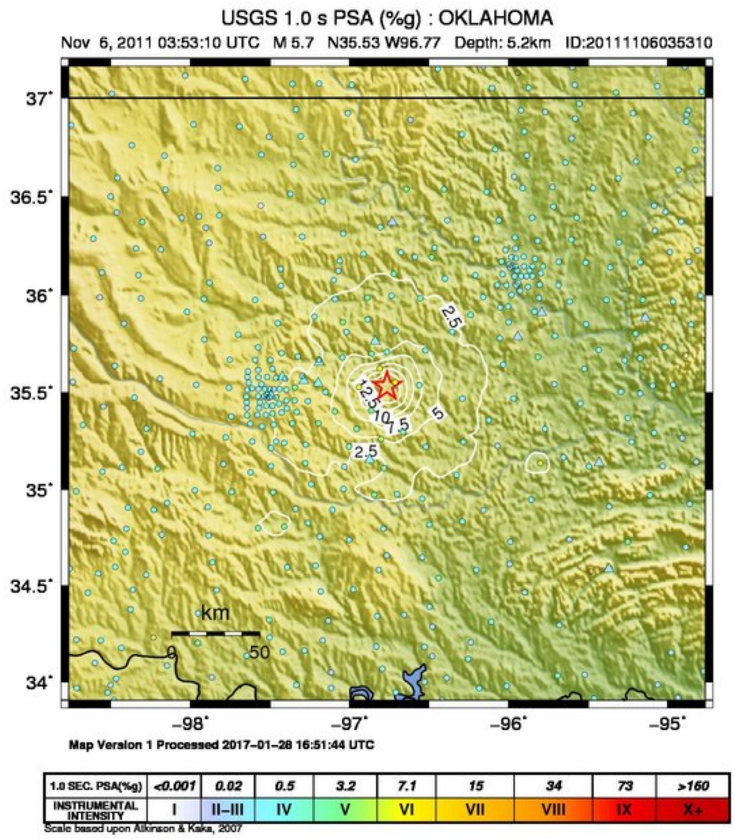

Figure 1.3: A ShakeMap for the 2011 Prague earthquake (USGS, 2015b).

Several steps go into creating these prioritized bridge inspection lists. First, a ground motion attenuation model is chosen for the affected region. This model is used in conjunction with ShakeMap (USGS, 2015b), an online component of the USGS, which creates a map after an earthquake showing the shaking levels in the area (Fig. 1.3). The ShakeMap is then sent to ShakeMap Broadcast (ShakeCast), an online resource from USGS (2017b), and combined with information about the bridges, such as their locations and fragility curves. The shaking intensity at the bridge sites and the bridges' fragility curves are evaluated to create a list that shows the bridges that are most likely to be damaged.

Fragility curves mathematically represent the predicted probability that the demand

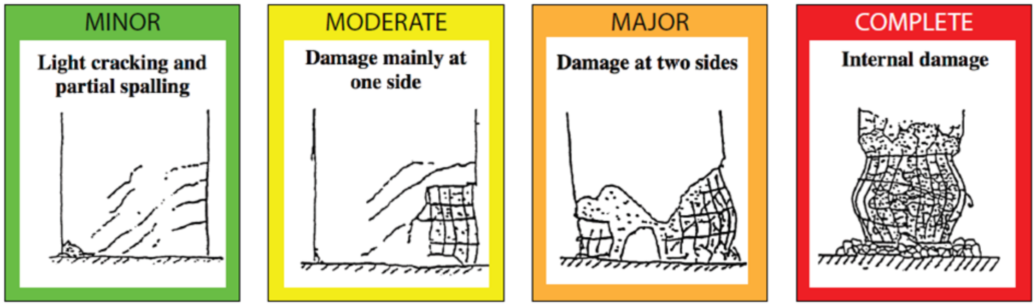

Figure 1.4: Examples of different damage states (adapted from Shinozuka et al. (2003)).

on a bridge will exceed the bridge's theoretical capacity (Mander, 1999). Several different methods are available to calculate fragility curves. One of the simplest methods is to use the Hazard U.S. (HAZUS) generalized bridge fragility curves (FEMA, 2003). However, for a more in-depth analysis of a particular bridge, a more analytical method must be used.

1.3 Bridge Fragility Curves

After an earthquake, it is important to quickly assess how much of the infrastructure has been damaged so that those structures can be closed for public safety. Sending inspectors to examine the structures is the only certain way to check for damage. However, because response crews often have limited personnel in the area that needs to be inspected, it is important to find a way to prioritize the structures. Fragility curves are one way to accomplish this: they estimate the damage level of structures based on the level of ground shaking they experience due to an earthquake (FEMA, 2003). A fragility curve statistically describes where the calculated demand on a structure exceeds the theoretical capacity of the structure. This is shown by plotting the probability of exceeding a given damage (limit) state (Fig. 1.4) as a function of the ground-motion intensity.

1.3.1 History of Fragility Curves

Several different methods have been used to develop structural fragilities, including expert testimony, empirical data, and analytical modeling. A summary of the methodology and a description of the pros and cons are given for each of these approaches.

The expert-based functions presented in the Applied Technology Council 13 (ATC-13) report were one of the earliest examples of fragility functions (ATC, 1985). Because there was very little recorded data available at the time with which to generate damage probability matrices (DPMs), the ATC assembled a panel of 42 experts to fill out a questionnaire concerning the various components of typical Californian infrastructure. Four of these experts were chosen to provide opinions for highway bridges (ATC, 1985). The questionnaire asked the experts to estimate a bridge's probability of being in a certain damage state based on a Modified-Mercalli Intensity (MMI) value. These results were examined and used to create DPMs for the ATC-13 and ATC-25 reports (ATC, 1991).

Expert-based fragility functions are the least reliable of the fragility functions. This is in part caused by the subjectivity of the input received; when the DPMs are compared to actual earthquake damage reports, little, if any, correlation has been found (Nielson, 2005). Additionally, the DPMs make it very difficult to develop accurate predictions for an individual bridge because only two types of bridges, those over 500 ft. and those under 500 ft., are included (Nielson, 2005). Furthermore, this data was based on Californian infrastructure, so its application to the Central and Eastern U.S. (CEUS) is questionable.

Empirical fragility curves are based on actual earthquake data, so they are easier to create and more accurate when a lot data is available. This quantity of data only occurs for earthquakes with large magnitudes that have damaged many bridges of different types. As a result of these limitations, several empirical fragility functions have been developed using data from the 1989 Loma Prieta and 1994 Northridge earthquakes including Basoz and Kiremidjian (1997), Der Kiureghian (2002), Shinozuka et al. (2003), Elnashai et al. (2004), and Shinozukaet al. (2000). This data was compiled into a list of the bridge type, damage state, and level of shaking for all bridges in the affected area and was used to create a damage frequency matrix (Basoz and Kiremidjian, 1997).

While the empirical fragility curves are more accurate than the expert-based functions, there are still some limitations. The variety of bridge construction methods and materials makes it difficult to find enough damaged bridges within a certain type to obtain statistically significant results. Therefore, bridge types are grouped together, which reduces the accuracy of the curves for individual bridges. Another cause of error occurs because of the inconsistency of recorded ground motion levels: maps created by USGS and Woodward-Clyde Federal Services (WCFS) show different shaking levels at the same location (Basoz and Kiremidjian, 1997). Similarly, bridge damage levels varied from inspector to inspector (Basoz and Kiremidjian, 1997). Finally, as previously mentioned, empirical fragility curves can only be created after significant events. The CEUS has not experienced enough large magnitude events to develop their own fragility curves, and the different faulting patterns, bridge types, and soil conditions bring into question the applicability of California-based empirical curves to bridges in the CEUS.

Analytical fragility functions are created when actual ground motion data and bridge damage levels are unavailable or to supplement existing empirical data. Three primary methods exist to find these functions: elastic spectral response, non-linear static analysis, and non-linear time history analysis.

The first of these methods, *elastic spectral response*, is the easiest and quickest of the approaches. Bridge component capacities are found using the Federal Highway Administration's (FHWA) *Seismic Retrofitting Manual for Highway Bridges* (FHWA, 1995b). Demand levels are determined by performing an elastic spectral analysis for the bridge. Then, the capacity-to-demand ratios are calculated, matched to certain damage states for several different peak ground accelerations, and used to create fragility curves (Jernigan and Hwang, 2002).

The second method, *non-linear static analysis*, offers better results than elastic spectral response and does not take an unreasonable amount of time because time-history analysis is not included. This is the method used by HAZUS to calculate its fragility curves for standard bridges (Bosöz and Mander, 1999). The bridge capacity is calculated by developing a non-linear static pushover curve. Demand is modeled by a reduced response spectrum plotted as an acceleration-displacement response spectrum which can be adjusted from an elastic to an inelastic response spectrum to better model the structure's behavior (Nielson, 2005). The intersection of the capacity and demand curves provides the information required to create the fragility curves (Nielson, 2005).

The third and final method, *non-linear time history analysis*, is the most accurate analytical approach, but it also is most computationally expensive. A suite of ground motions is developed for the bridge's region. Then, finite element models of the bridge undergo numerical simulations using the suite of ground motions to generate bridge component responses. This information is used to create a probabilistic seismic demand model. Each component's capacity is found using expert based, experimentally based, and/or analytically based methods. The demand and capacity models are used to create fragility curves (Nielson, 2005).

The following two sections explain options available to develop fragility curves for a large set of bridges, such as ODOT's inventory of bridges. Both of the options discussed rely on analytical fragility curves.

1.3.2 HAZUS Fragility Curves

HAZUS (FEMA, 2003), a standardized methodology for estimating potential losses due to natural disasters, developed "standard bridge" fragility curves for slight, moderate,

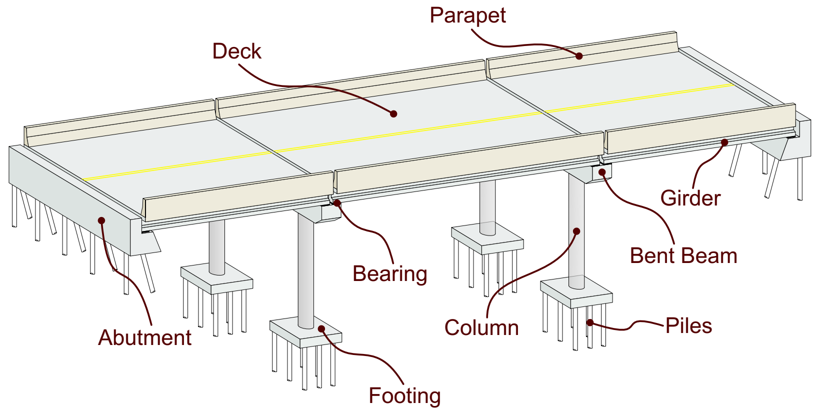

Figure 1.5: Typical bridge components (Nielson, 2005).

extensive, and complete damage (Mander, 1999). The qualitative description of the four damage states is given in Table 1.1 and the mentioned bridge components are shown in Fig. 1.5. The fragility curves are based on a log-normal cumulative distribution function (with a log standard deviation equal to 0.6) parametrized by the median 1.0-sec spectral acceleration (S_1).

There are several metrics to measure ground motion intensity due to an earthquake. Some of the most common include peak ground acceleration (PGA), peak ground velocity (PGV), spectral acceleration at a period of 0.3-sec ($S_{0.3}$), spectral acceleration at a period of 1.0-sec (S_1), and spectral acceleration at a period of 3.0-sec (S_3). HAZUS uses S_1 because most damage states for bridges are most closely governed by the long period case (Bosöz and Mander, 1999).

For each of the 28 bridge classes described by HAZUS (HWB1–HWB28), a median PGA value is given, which is converted to S_1 by a combination of the factors K_{3D}, K_{skew}, and K_{shape} to account for variations among the individual bridges due to the number of spans of the bridge, the skew angle of the bridge, and the estimated period of the bridge, respectively. The skew angle is the angle between the bridge's supports and the line perpendicular to its deck. In an unskewed bridge, the supports are perpendicular to the deck. Fig. 1.6 illustrates the skew angle.

Table 1.1: HAZUS damage (limit) states (FEMA, 2003).

Limit State	Description
Slight	Minor cracking and spalling to the abutment, cracks in shear keys at abutments, minor spalling and cracks at hinges, minor spalling at the column (damage requires no more than cosmetic repair) or minor cracking to the deck.
Moderate	Any column experiencing moderate (shear cracks) cracking and spalling (column structurally still sound), moderate movement of the abutment (< 2 in.), extensive cracking and spalling of shear keys, any connection having cracked shear keys or bent bolts, keeper bar failure without unseating, rocker bearing failure or moderate settlement of the approach.
Extensive	Any column degrading without collapse – shear failure – (column structurally unsafe), significant residual movement at connections, or major settlement approach, vertical offset of the abutment, differential settlement at connections, shear key failure at abutments.
Complete	Any column collapsing and connection losing all bearing support, which may lead to imminent deck collapse, tilting of substructure due to foundation failure.

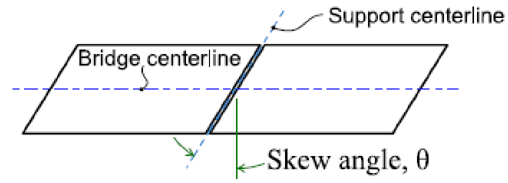

Figure 1.6: Illustration of bridge skew angle (Nielson, 2005).

The information needed from each bridge to complete these calculations includes the year built, number of spans, skew angle, main span material, and maximum span length, all of which can be found in the National Bridge Inventory (NBI) (USDOT, 2015). The *HAZUS MR4 Technical Manual* provides a full description of the calculations used to develop the fragility curves (FEMA, 2003). A condensed version of this procedure is given in Appendix A. These same fragility curves are used by ShakeCast (Wald et al., 2008) to create a priority ranking of bridges that need to be inspected after an earthquake.

The calculated fragility curve is used to predict how the bridge will respond during an earthquake. For instance, given an S_1 value, one can determine the probability of a particular bridge being in each of the damage states. Fig. 1.7 shows sample fragility curves for a bridge described in Mander (1999). If this bridge experiences an S_1 of $0.2g$, as shown on the x-axis, it has a 61% chance of being in the slight damage state, a 38% chance of being in the moderate damage state, a 25% chance of being in the extensive damage state, and a 10% chance of being in the complete damage state.

In the event of an earthquake, Caltrans uses the median (50%) S_1 for each of the damage states to determine a list with the priority ranking of bridges to inspect. For the example in Fig. 1.7, if the bridge experienced an S_1 between $0.10g$ and $0.24g$, it would be flagged green for low inspection priority. Between $0.24g$ and $0.30g$ would be flagged yellow for medium priority, between $0.30g$ and $0.44g$ would be flagged or-

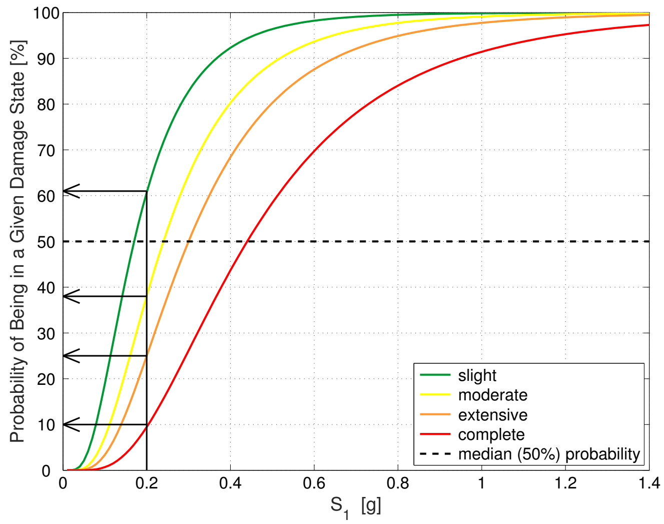

Figure 1.7: Sample fragility curves for a bridge described in Mander (1999).

ange for medium-high priority, and above $0.44g$ would be flagged red for high priority. Within each flagging color, bridges are prioritized by how close their level of shaking is to the damage state. For instance, in the example given above, a bridge that experiences $0.3g$ would have a higher inspection priority than a bridge that experiences $0.25g$, even though both were flagged yellow, because the $0.3g$ bridge is closer to the moderate damage state. However, it is important to remember that this flagging system is not a guarantee that bridges will be damaged because of an earthquake: it is only a means of ranking the bridges most likely to be damaged and prioritizing post-earthquake inspections.

Because the HAZUS fragility curves are based on standard bridges, they cannot take into consideration all of the details of an individual bridge. Therefore, the fragility curves should be used as a guide rather than a definitive, deterministic representation for all bridges. More rigorous analytical methods may be used to get a more accurate representation of a bridge, or component based fragility curves may be utilized.

1.3.3 Component Based Fragility Curves

ShakeCast v2 used HAZUS fragility curves as its default for bridge fragility curves because it required little effort or additional information to calculate the fragility curves. ShakeCast v3 offers the option for additional accuracy of using component-based fragility curves (Lin et al., 2015). These are more accurate, but require additional data about the system's bridges which must be obtained through modeling. California is currently developing these fragility curves for their bridges; however, because of different soil conditions and bridge construction standards, we do not believe they can be directly transferred to other parts of the country.

Nielson (2005) researched creating component-based fragility curves for the central and southeastern United States. He examined the region's bridge inventory using the NBI database, and found the most common types of bridges in this region, listed in Table 1.2. These types are subdivisions of the HAZUS bridge classes, which should allow for more accurate results for individual bridges.

Similar to HAZUS, Nielson (2005) examined the year built, the number of spans, the maximum span length, the total length, the skew angle, and the structure type, but he also included information about deck width, vertical underclearance, deck condition rat-

Table 1.2: Bridge types examined by Nielson (2005) and their HAZUS classes.

Bridge Type	HAZUS Class
Multi-Span Continuous Concrete Girder	HWB10, HWB22
Multi-Span Continuous Slab	HWB10, HWB22
Multi-Span Continuous Steel Girder	HWB15, HWB26
Multi-Span Simply Supported Concrete Girder	HWB5, HWB17
Multi-Span Simply Supported Concrete Box Girder	HWB5, HWB17
Multi-Span Simply Supported Slab	HWB5, HWB17
Multi-Span Simply Supported Steel Girder	HWB12, HWB24
Single-Span Concrete Girder	HWB3
Single-Span Steel Girder	HWB3

ing, superstructure condition rating, and substructure condition rating. Although a large skew angle can significantly reduce the median of fragility curves (i.e. making damage more probable), Nielson (2005) did not model bridges with skew angles because most of the bridges in the area examined had small skew angles.

After examining the various bridges, Nielson (2005) created models of each of these bridges in the finite element software *OpenSees* (McKenna and Feneves, 2000) and chose a suite of ground motions to represent the seismic activity in the region. These ground motions were used to test the bridge models. He also examined the effect of different parameters on the bridge fragility. Nielson (2005) chose to use PGA instead of S_1 as the ground motion intensity measure for his study because he found it to be the most efficient of the measures for use with bridges and the least sensitive to fluctuations in behavior. The medians for fragility curves that Nielson (2005) found were different from the HAZUS medians, some values greater and some smaller. Most significantly, the slight damage states for the multi-span continuous bridges were smaller than the HAZUS values. This is important because the slight damage state marks the point after which bridges should be inspected, and Nielson found that bridges need to be inspected at lower levels of shaking than HAZUS prescribes.

Yang et al. (2015) conducted non-linear time history analyses to explore the effects of skew angle on bridges in the central southeastern United States. He concluded that larger skew angles do indeed make bridges more fragile and developed formulas for these relationships (Yang et al., 2015).

1.4 Summary

Most of the in-depth bridge analyses to date have been based on California bridges. Due to different construction methods and soil conditions, it is important to increase the amount of research for the CEUS. In Chapter 2, smart radii, an improvement on former

ODOT inspection radii, will be developed. In Chapter 3, existing attenuation models will be compared to actual Oklahoma ground motions. In Chapter 4, a case study will be performed on the I-35 bridge over the Cimarron River to validate HAZUS fragility curves. In Chapter 5, work on ground motions and fragility curves from the previous chapters will be combined to create ShakeCast-OK, which will be used as part of ODOT's post-earthquake bridge inspection protocol. The final chapter will summarize conclusions and propose future work.

Chapter 2

Post-Earthquake Smart Bridge Inspection Radii

2.1 Overview

To revise ODOT's inspection radii, both the capacity of and demand on Oklahoma bridges were considered. Bridge capacity was modeled with HAZUS fragility curves. The seismic demand was quantified by ground-motion intensity, which was predicted using a ground-motion attenuation model adjusted for soil amplification and calibrated with measured acceleration records from seismic stations in Oklahoma. The analysis found that bridge inspections were not necessary for earthquakes with a magnitude less than 4.6 (10% probability of slight damage), and ODOT's inspection radii implemented on 23 January 2015 (see Section 1.2.2) could be reduced.

2.2 Trigger S_1 Value for Determining Inspection Radii

In order to determine inspection radii, a trigger S_1 value, below which damage is unlikely to be found, must first be determined. However, the fragility curve for the lowest damage state (slight) cannot be calculated *a priori* because it requires knowledge of the spectral acceleration at 1.0 s and 0.3 s. Because of this, Caltrans uses a trigger S_1 value of $0.10g$ instead of a fragility curve for slight damage. This value comes from their

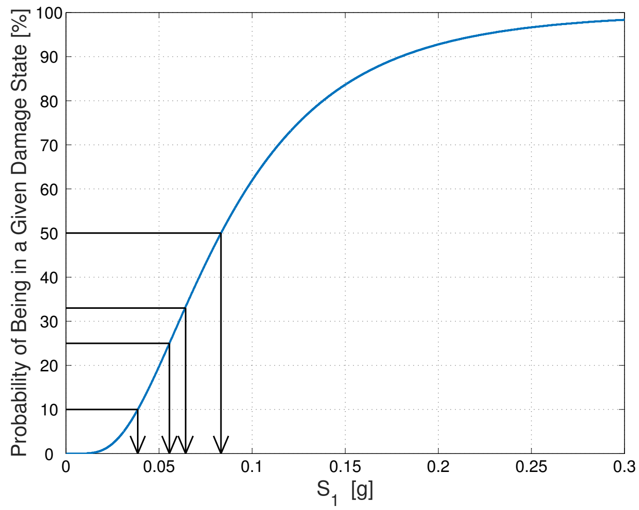

Figure 2.1: Base fragility curve used for Oklahoma.

experience of not seeing damage on bridges that experience an S_1 less than $0.10g$ (L. Turner, personal communication, 2015).

ODOT, however, has not had Caltrans' experience to determine if an S_1 of $0.10g$ is also valid in Oklahoma. Therefore, the median S_1 values for the slight damage state in HAZUS were examined and compared for non-California and California bridges. There were four instances where the same bridge had a different value for a non-CA bridge versus a CA bridge: HWB5 and HWB6, HWB12 and HWB13, HWB17 and HWB18, and HWB24 and HWB25. Each of these instances gave the CA bridge a median S_1 value of $0.30g$ and the non-CA bridge a median S_1 value of $0.25g$ (FEMA, 2003). Using this information, a ratio between the two bridges was determined and applied to the S_1 value of $0.10g$ from Caltrans to give an S_1 value of $0.0833g$ for Oklahoma.

To ensure a greater level of confidence, the value of $0.0833g$ for Oklahoma was used as the median S_1 for a base fragility curve (Fig. 2.1). The trigger S_1 values for 10%, 25%, 33%, and 50% probability of being in the slight damage state, were found to be $0.0386g$, $0.0556g$, $0.0643g$, and $0.0833g$, respectively. This will allow ODOT to choose the probability of being in the slight damage state that they feel most comfortable with.

2.3 Ground-Motion Prediction Equation

Having determined the levels of shaking deemed necessary to inspect for bridge damage, the next step was to find an attenuation model (or ground-motion prediction equation) that could predict at what distance from the epicenter these levels of shaking would occur. Two attenuation models were examined: Campbell (2003) and Kaka and Atkinson (2005). Campbell (2003) was chosen over Kaka and Atkinson (2005) because the latter gives vertical S_1 instead of horizontal S_1. Additionally, ShakeMap currently uses the Campbell (2003) attenuation model for Oklahoma (USGS, 2011). Campbell (2003) was developed for earthquakes with magnitude between 5.0 and 8.2 and is based on ENA (Eastern North America) hard rock.

The Campbell (2003) ground-motion prediction equation is

$$\ln(S_1) = c_1 + c_2 M_w + c_3(8.5 - M_w)^2 + c_4 \ln(R) + f(r_{\text{rup}}) + (c_9 + c_{10} M_w) r_{\text{rup}} \tag{2.1}$$

where

$$R = \sqrt{r_{\text{rup}}^2 + [c_5 \exp(c_6 M_w)]^2} \tag{2.2}$$

$$f(r_{\text{rup}}) = \begin{cases} 0 & \text{for } r_{\text{rup}} \leq r_1 \\ c_7(\ln r_{\text{rup}} - \ln r_1) & \text{for } r_1 < r_{\text{rup}} \leq r_2 \\ c_7(\ln r_{\text{rup}} - \ln r_1) & \\ \quad + c_8(\ln r_{\text{rup}} - \ln r_2) & \text{for } r_{\text{rup}} > r_2 \end{cases} \tag{2.3}$$

and S_1 is the geometric mean of the two horizontal components of spectral acceleration at 1.0 s for Site Class B (hard rock) in g, M_w is the moment magnitude, r_{rup} is the closest distance to fault rupture (hypocentral distance) in km, $r_1 = 70$ km, and $r_2 = 130$ km. The coefficients c_i are given in Table 2.1. Fig. 2.2 shows a graph of the Campbell (2003) attenuation model for three different magnitude events. S_1 is largest closest to

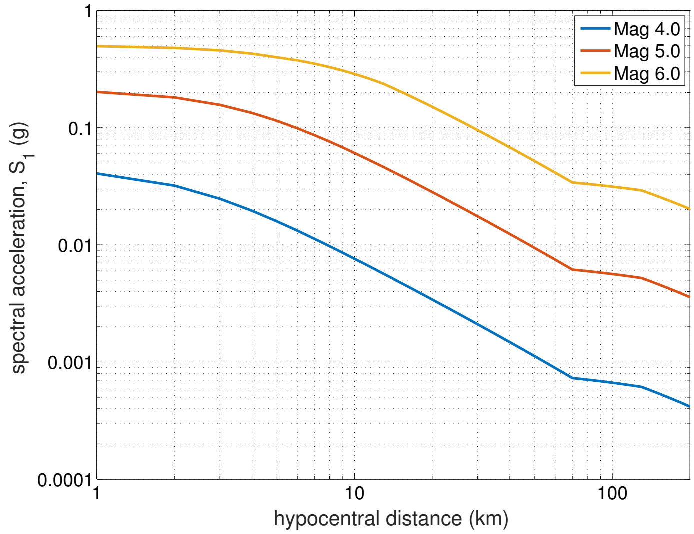

Figure 2.2: Campbell (2003) attenuation model for Magnitude 4.0, 5.0, and 6.0 events.

the epicenter of the earthquake and decreases as the distance increases.

Because Campbell (2003) models the ground motion for hard rock (Site Class B), a site amplification factor was used to correct the model for Oklahoma soil. The average shear-velocity down to 30 m (V_s^{30}) is a standard metric used to classify site conditions. A USGS custom V_s^{30} map of Oklahoma and the surrounding area (Fig. 2.3) showed that only Site Class C and D are present in Oklahoma (USGS, 2010). To ensure the inspection radii were independent of the location of the earthquake, Site Class D (stiff soil) was used to represent all of Oklahoma because it is more conservative than Site Class C. Further, Site Class D is the default site class per the ASCE 7-10 building code where

Table 2.1: Campbell (2003) attenuation model coefficients c_i for 1-sec spectral acceleration (S_1) [Eq. (2.1)].

coefficient	value	coefficient	value
c_1	−0.6104	c_6	0.503
c_2	0.451	c_7	1.067
c_3	−0.2090	c_8	−0.482
c_4	−1.158	c_9	−0.00255
c_5	0.299	c_{10}	0.000141

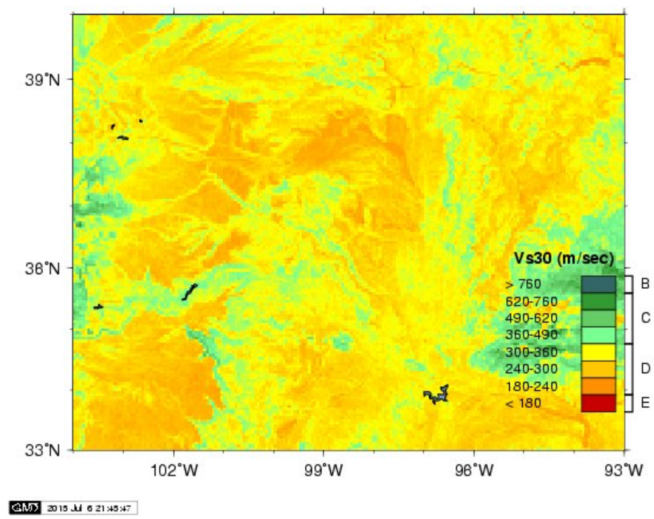

Figure 2.3: Map of V_s^{30} for Oklahoma (USGS, 2010).

"the soil properties are not known in sufficient detail" (ASCE/SEI 7-10, 2010, 11.4.2). The Site Class soil amplification factors can be found in NEHRP Recommended Seismic Provisions (Building Seismic Safety Council, 2009). All of the S_1 values chosen for the radii cutoffs are under $0.10g$, so the following formula is used to calculate the S_1 values for the inspection radii:

$$S_{M1} = 2.4 \times S_1 \tag{2.4}$$

where S_1 is the spectral acceleration at 1.0 s for Site Class B and S_{M1} is the spectral acceleration at 1.0 s adjusted for site class effects (Site Class D).

2.3.1 ShakeMap Bias Factor Calculation

Because Campbell (2003) is calibrated for use with earthquakes of magnitude 5.0 to 8.2, the model needed to be adjusted for the smaller earthquakes experienced in Oklahoma. To accomplish this, ShakeMap uses a bias factor to adjust the magnitude of an earthquake such that the magnitude of the earthquake plus the bias factor yields the best fit to the station data. This best fit is found by minimizing the L_1 norm using station data from the stations within 120 km of the epicenter of the earthquake (Worden et al., 2010):

$$L_1 = \sum_{i=1}^{n} \left| \ln(S_1^{(i)}) - \ln(\hat{S}_1^{(i)}) \right| \tag{2.5}$$

where n is the number of stations, $S_1^{(i)}$ is the spectral acceleration at 1.0 s for Site Class B calculated using the measured acceleration time-history at the ith station and $\hat{S}_1^{(i)}$ is the spectral acceleration at 1.0 s for Site Class B predicted by Eq. (2.1) with the magnitude bias adjustment.

ShakeMap calculates S_1 and a respective bias factor for Oklahoma earthquakes only if the magnitude of the earthquake exceeds 4.8 (C. B. Worden, personal communication, 14 July 2015).* When the smart radii were developed (August 2015), Oklahoma and the surrounding areas had experienced only two earthquakes with magnitude greater than 4.8: the 5.6 magnitude earthquake in 2011 (Oklahoma) and the 4.9 magnitude earthquake in 2014 (Kansas). A bias factor was not calculated for the former because ShakeMap was not using the Campbell (2003) attenuation model in 2011.

2.3.2 Bias Factor Calibration

To predict S_1 for future earthquakes, bias factors calibrated to all earthquakes affecting Oklahoma and the surrounding regions are required. An approach similar to that of ShakeMap (Worden et al., 2010) was adopted to calibrate bias factors correlated to actual seismic station data in and around Oklahoma. Fitting the bias factor requires measured ground-motion acceleration time-histories from previous earthquakes. Ground-motions from seismic stations were acquired for 41 earthquakes that had a magnitude of at least 4.0 occurring between 27 February 2010 and 20 June 2015 (USGS, 2015b). Fig. 2.4 shows a distribution of the earthquakes' magnitudes, depths, and locations.

The acceleration time-histories were retrieved from Standing Order for Data (SOD)

*This threshold was subsequently reduced to M3.5 by USGS on 17 December 2015.

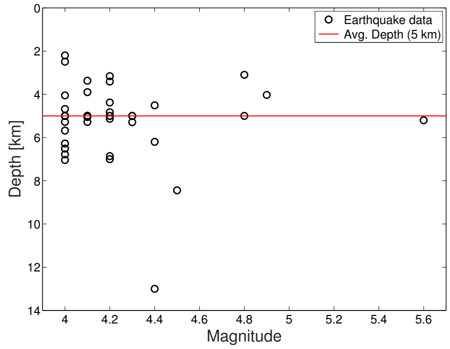

(a)

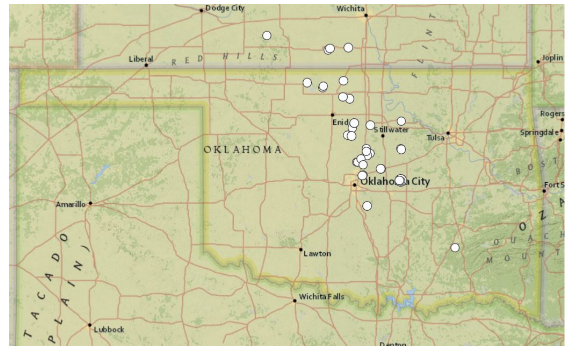

(b)

Figure 2.4: Distribution of earthquakes used to calibrate the bias factor: (a) depth versus magnitude; (b) earthquake location (USGS, 2015b).

for the GS, US, OK, N4, AG, HQ, and TA seismic networks (Owens et al., 2004). For stations with a `?N?` channel code (acceleration), the earthquake data was retrieved and processed according to a modified version of the waveform recipe provided by SOD to generate a SAC file with the acceleration time-histories of each station. For stations with a `?H?` channel code (high gain seismometer measuring velocity), the earthquake data was retrieved and processed similarly to the `?N?` earthquake data and then differentiated to generate a SAC file with the acceleration time-histories of each station. These SAC files were written in Intel processor style little endian byte order.

The SAC files were converted to MAT files to be read in MATLAB (Liel, 2014). Each MAT file included a matrix of times (s) and of accelerations (m/s^2). A few of the peak accelerations (PGA) retrieved from the SOD station data were spot-checked against the PGA values from the respective stations and earthquakes provided by the ShakeMap Archive. For the comparison, the PGA from SOD was converted to $\%g$ to be consistent with ShakeMap. Although none of the data exactly matched the ShakeMap station values, the values were generally very close. Another resource used to compare our PGA values to the USGS PGA values was the Event Page link provided in the USGS Preliminary Earthquake Report email. For the M4.0 event which occurred on 20 June 2015 at 5:10:54 UTC, there was an average percent error of 1.97% between the PGA

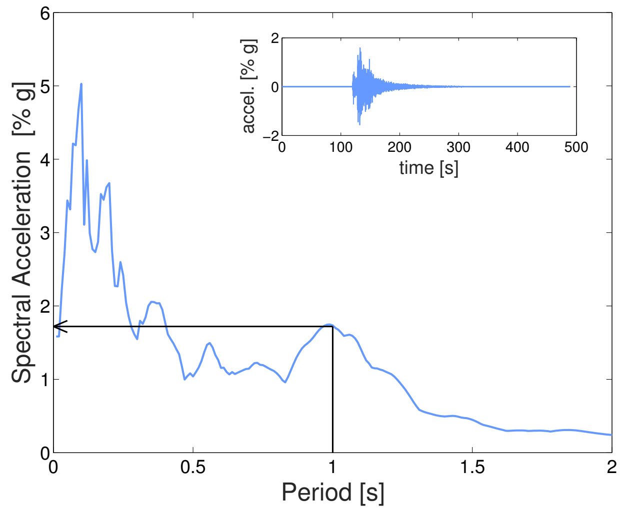

Figure 2.5: Response spectrum (5% damped) for the HHE acceleration time-history (top-right) provided by the OK.OKCFA seismic station for the magnitude 5.6 Oklahoma earthquake that occurred on 6 November 2011. Spectral acceleration at 1.0 s (S_1) is identified.

values from SOD and USGS. The maximum percent error was 5.94% and the minimum was 0.06%. Additionally, while most of the stations and channel codes provided by SOD and USGS were the same, both SOD and USGS had some stations not presented by the other and USGS had more channel codes than provided by SOD.

Response time-histories for a 5%-damped single-degree-of-freedom oscillator were calculated in MATLAB via numerical simulation from which horizontal components (i.e., `??E` and `??N`) of S_1 were identified for each station. Fig. 2.5 shows an example response spectrum and how S_1 is identified. The S_1 values were matched with the longitude and the latitude retrieved from SOD (Owens et al., 2004). For Oklahoma and the surrounding area, ShakeMap generated S_1 values only for the M5.6 earthquake in 2011 and the M4.9 in 2014, so the calculated S_1 values could only be spot-checked against the values from those earthquakes. Similar to the PGA values, the calculated S_1 values matched closely with the ShakeMap Archive data although none of them matched exactly.

While ShakeMap does not give the S_1 values for events of lower magnitudes, the map found through the Event Page link does have S_1 calculated for all of the stations. For example, for the M4.0 event which occurred on 20 June 2015 at 5:10:54 UTC, there was an average error of 5.58% between the S_1 values from SOD and USGS. The maximum error was 15.71% and the minimum was 0.58%. These errors may be do to differences in ground motion processing techniques.

A bias factor was calculated for each of the 41 earthquakes by using the stations' longitude, latitude, and horizontal components of S_1 and the earthquake's magnitude, depth, and epicenter (longitude and latitude). For each station, the epicentral distance r was calculated using the spherical law of cosines (Gellert et al., 1989), from which the hypocentral distance r_{rup} was calculated:

$$r_{\text{rup}} = \sqrt{r^2 + d^2} \tag{2.6}$$

where d is the depth of the earthquake. Only stations within a 120 km radius of the earthquake were used to calibrate the bias factor. Finding the bias factor for each earthquake that minimizes Eq. (2.5) requires a comparison between the measured and predicted values of S_1. Recall that Campbell (2003) [Eq. (2.1)] predicts the *geometric mean* of the horizontal components of S_1 for *hard rock* sites (Site Class B). To be consistent in the comparison between the station data and the values predicted by Campbell (2003), the geometric mean of the two horizontal components of S_1 was calculated from each seismic station's data, and the station S_1 values were converted from the mapped Site Class (C or D, see Fig. 2.3) to Site Class B. The latter was done by dividing the S_1 value for each station by the station's site amplification factor. The site amplification factor is dependent on the magnitude of S_1. The relevant values from the NEHRP Site Coefficient Table can be found in Table 2.2 (Building Seismic Safety Council, 2009). If the station S_1 value falls between the given S_1 values, the site amplification factor was linearly interpolated.

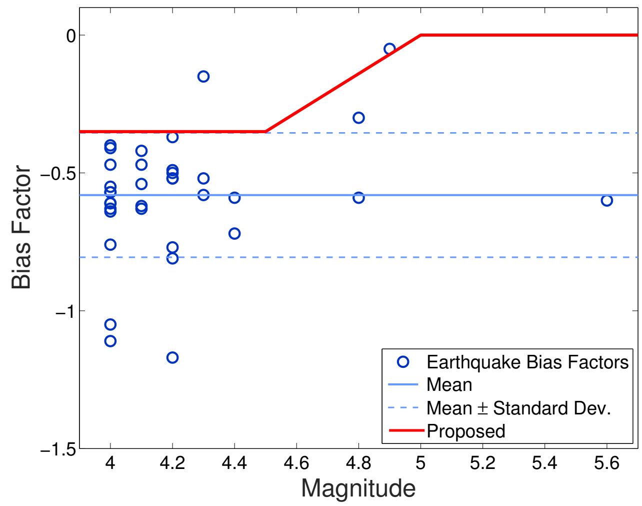

Figure 2.6: Distribution of calculated bias factors with mean and standard deviation indicated. The proposed bias factor curve is also indicated.

Fig. 2.6 shows the calculated bias factors. Bias factors were retained only for events with six or more seismic stations. Analyzing the bias factors for all of the earthquakes with magnitudes between 4.0 and 5.6 gave a maximum of −0.05, a minimum of −1.17, a mean of −0.5803, and a standard deviation of 0.2256. Conservatively, a bias factor of −0.35 (approximately the mean plus one standard deviation) was chosen, instead of the mean, to represent all Oklahoma earthquakes of magnitude 4.5 and below. There is only one event with a magnitude of 5.0 or greater. This is not enough data to determine an average bias factor from, so a bias factor of 0 was chosen for earthquakes with a magnitude of 5.0 or greater. Between magnitudes 4.5 and 5.0 the bias factor is linearly interpolated. A magnitude of 4.5 was chosen because most of the data is for magnitudes below 4.5. The proposed bias factor curve is shown in Fig. 2.6.

Table 2.2: Site amplification factors.

Site Class	**Spectral Response Acceleration Parameter at 1-sec Period**				
	$S_1 \leq 0.1$	$S_1 = 0.2$	$S_1 = 0.3$	$S_1 = 0.4$	$S_1 \geq 0.5$
C	1.7	1.6	1.5	1.4	1.3
D	2.4	2.0	1.8	1.6	1.5

Fig. 2.7 shows all of the station data for magnitude 4.0 and 4.2 Oklahoma earthquakes compared to predictions using Campbell (2003) with no bias, with the mean bias factor, and with the mean bias factor ± the standard deviation of the bias factors. Note that for magnitude 4.0 and 4.2 Oklahoma earthquakes, the mean bias factor plus one standard deviation is the proposed value. Fig. 2.7 also shows that even though we fit the bias factors to individual events, the mean of the bias factor still does a good job of fitting the data from all of the stations for a given magnitude. However, Fig. 2.7 also illustrates the considerable spread in the data. The biased model does not capture this amount of spread, so this model both under- and over-predicts the extreme points. ShakeMap, however, is better able to reflect this spread because it analyzes real-time station data and uses these numbers in its S_1 calculations.

Fig. 2.8 shows station data for four earthquakes compared to predictions using Campbell (2003) with no bias, with the bias factor producing the best fit, and with the proposed bias factor. The unbiased Campbell model typically over-predicts the station data, identifying a need for the model to be adjusted. In every case except Fig. 2.8(b), the best fit bias factor appears to fit the data rather well. However, there are still data points above the curve of the best fit bias factor in each case. When determining the bias factor for inspection radii, we do not want to fit the data, but rather find an upper-bound for the data. The proposed bias factor attempts to quantify this upper-bound. With the exception of Fig. 2.8(b), the proposed bias factor does create the upper-bound for all except one or fewer of the data points for each event.

The reason for the poor fit in Fig. 2.8(b) might be because the fitting of the model is limited: changing the magnitude only moves the Campbell curve up and down. There is no way to change the slope of the sections of the curve to create an even better fit for this data. Creating an Oklahoma specific attenuation model would correct this problem; however, this task is out of the scope of this project.

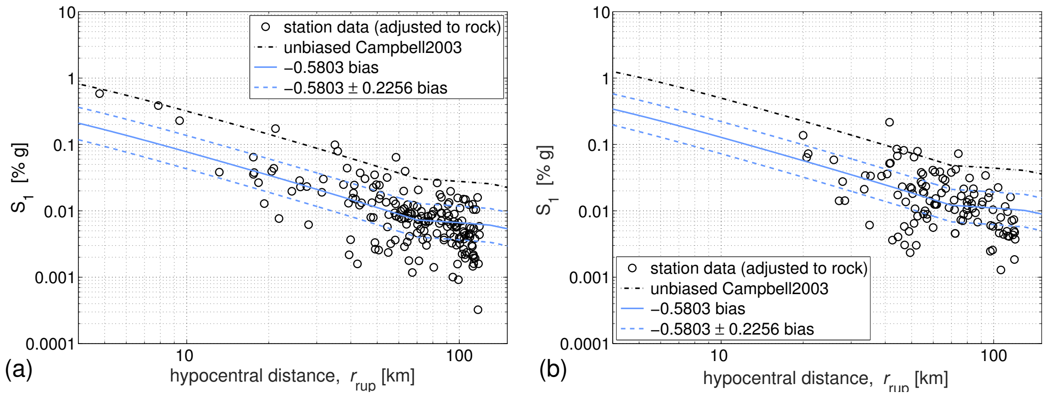

Figure 2.7: All station data for all earthquakes of magnitude (a) 4.0 and (b) 4.2 compared to predictions using Campbell (2003) with and without bias.

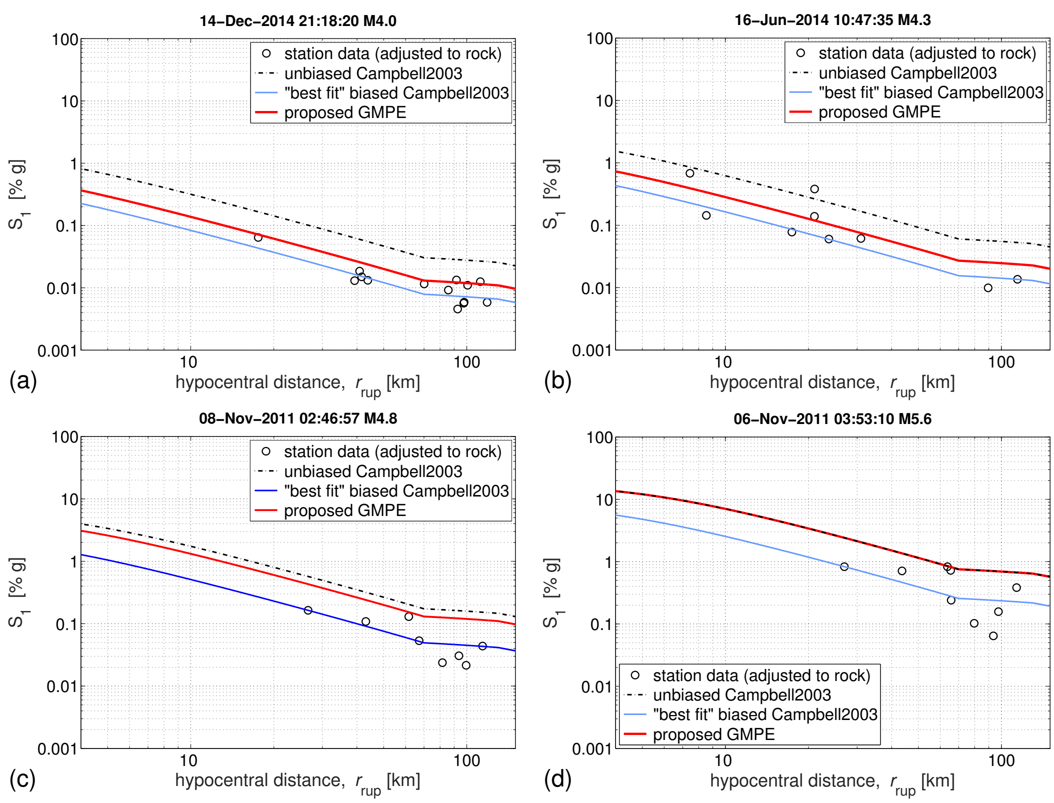

Figure 2.8: Earthquake station data compared to Campbell (2003) with no bias, with the bias factor producing the best fit, and with the proposed bias factor of (a) −0.35, (b) −0.35, (c) −0.14, and (d) 0.

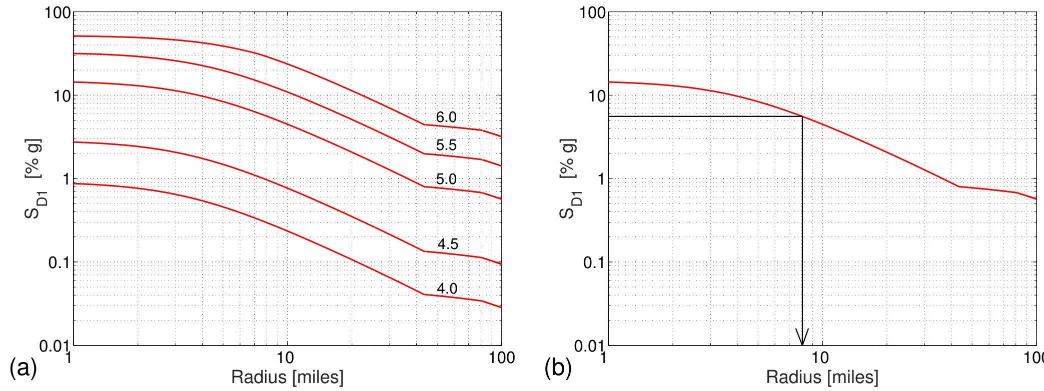

Figure 2.9: (a) Proposed attenuation model for magnitudes 4.0, 4.5, 5.0, 5.5, and 6.0. (b) Selection of inspection radius for magnitude 5.0.

2.4 Smart Inspection Radii

The spectral response accelerations predicted by the attenuation model presented in the preceding section represent the geometric mean of the horizontal components of S_1, not the maximum response in the horizontal plane. The spectral accelerations computed from the biased Campbell (2003) model are scaled by a factor of 1.30 to increase the motions to the maximum response (S_{D1}) for the purpose of determining inspection radii Fig. 2.9(a) shows the proposed attenuation relation for five magnitudes, assuming a depth of 5 km when calculating r_{rup}. This depth was selected because it is the average depth of Oklahoma earthquakes (See Fig. 2.4). These curves were then used to find an inspection radius for each magnitude based on the S_1 values selected from the base fragility curve (Fig. 2.1). For each magnitude between 4.0 and 6.5 and for each critical S_1 value (i.e., 0.0386g, 0.0556g, 0.0643g, and 0.0833g), the largest radius at which the critical S_1 is expected to be exceeded was found. Fig. 2.9(b) gives an example of this process: for an M5.0 earthquake, the proposed attenuation model shows that the inspection radius for a 25% probability of being in the slight damage state (S_{D1} = 5.56%g) is 8.1 miles. To put the data in a format best suited for inspectors to use, the radii were converted from km to miles. The resulting radii are presented in Table 2.3.

Table 2.3: Inspection radii based on Campbell (2003) calibrated with bias factor and adjusted for site amplification.

Magnitude	Inspection Radii Based on *P*% Probability of Being in Slight Damage State (miles)			
	P = 10	*P* = 25	*P* = 33	*P* = 50
4.5	–	–	–	–
4.6	1.2	–	–	–
4.7	3.6	1.0	–	–
4.8	5.8	3.5	2.5	–
4.9	8.4	5.6	4.6	3.0
5.0	11.5	8.1	6.9	5.0
5.1	13.7	9.7	8.4	6.3
5.2	16.1	11.6	10.1	7.7
5.3	18.8	13.6	11.9	9.3
5.4	21.9	16.0	14.0	11.0
5.5	25.3	18.5	16.3	12.9
5.6	29.1	21.4	18.9	15.0
5.7	33.3	24.6	21.8	17.4
5.8	37.9	28.1	24.9	20.0
5.9	42.9	32.0	28.4	22.8
6.0	76.3	36.2	32.1	25.9
6.1	95.0	40.8	36.3	29.3
6.2	112.8	58.4	40.7	33.0
6.3	132.0	86.3	57.2	37.0
6.4	152.7	102.0	85.4	41.2
6.5	174.6	119.0	100.5	59.3

2.5 Prioritizing Bridges

ODOT provided data for 3773 bridges owned and maintained by the state on the ODOT-designated highway system, referred to as "on-system" bridges, for which HAZUS fragility curves were calculated.[†] This data was used to calculate fragility curves for the bridges using HAZUS. The 25% probability of being in a moderate damage state, calculated by HAZUS, was used to sort and prioritize the bridges. Approximately one tenth of the on-system bridge inventory, 353 bridges, were tagged as priority. Of these,

[†]Note that "off-system" bridges (i.e., bridges owned and maintained by a county, city, or other local or regional governmental unit, and not on the ODOT-designated highway system) were not included.

32 were tagged as high priority, 109 were tagged as medium-high priority, and 212 were tagged as medium priority. The lists of these bridges can be found in Tables B.1, B.2, and B.3, respectively, in Appendix B. All remaining bridges were classified as low priority. Within the inspection radius, high priority bridges should be inspected first, medium-high priority bridges inspected second, medium priority bridges third, and low priority bridges last.

HAZUS is unable to calculate the fragility curves for 3 masonry bridges and 83 bridges tagged as "skew = 99 degrees" (variable skew). Therefore, masonry bridges were tagged as high priority bridges, and variable skew bridges were placed in their own category. Table B.4 lists the variable skew bridges. These bridges should be treated as high priority bridges until more information is obtained.

This prioritization system for bridges does not take into consideration the actual shaking a bridge undergoes in an earthquake. Shaking is greatest at the epicenter of an earthquake and decreases with distance. Therefore, it is important to keep in mind that a low priority bridge at the epicenter of the earthquake might be more at risk for damage than a high priority bridge located at the edge of the inspection radius. The prioritization provided here is preliminary and should be used until more sophisticated systems such as ShakeCast can be implemented (Chapter 5).

2.6 Recommendations

By examining fragility curves for bridges, the ground-motion attenuation model, soil amplification factors, and acceleration time-histories from seismic stations, the inspection radii presented in Table 2.3 were developed. These values were presented to ODOT at the monthly seismic meeting on 28 July 2015. By using this table, ODOT is able to choose what probability of being in a slight damage state they are comfortable with and modify their post-earthquake inspection protocol accordingly. It was recommended that, as a starting point, ODOT use the 25% probability column and move to higher probabilities if there is still no damage seen within those radii. Table 2.4 gives the recommended candidate grouping of these inspection radii. Within the inspection radius, high priority bridges should be inspected first, medium-high priority bridges inspected second, medium priority bridges third, and low priority bridges last.

Table 2.4: Smart radii groupings.

Magnitude Range	Inspection Radius (miles)
4.7 to 4.8	5
4.9 to 5.3	15
5.4 to 5.8	30
5.9 to 6.2	60
6.3 +	120

2.6.1 Expanding Inspection Radii

For a given event, the inspection radius should be expanded (1) to account for location uncertainty and/or (2) if damage is found within five miles of the perimeter of the inspection area. There is inherently some uncertainty in the identification of the location of the earthquake epicenter. This location uncertainty is included in the ENS (Earthquake Notification System) reports published by the USGS (Fig. 2.10). To account for this uncertainty, the inspection radius should be expanded by the reported *Horizontal* Location Uncertainty. Note that this value is reported in kilometers which will need to be converted to miles for consistency. Additionally, the inspection radius should be expanded by five miles if damage is found within the outer five miles of the original inspection radius.

2.7 Summary

The *smart inspection radii* presented here incorporate both the demand on and capacity of Oklahoma bridges. Demand is quantified by the ground-motion intensity, in this

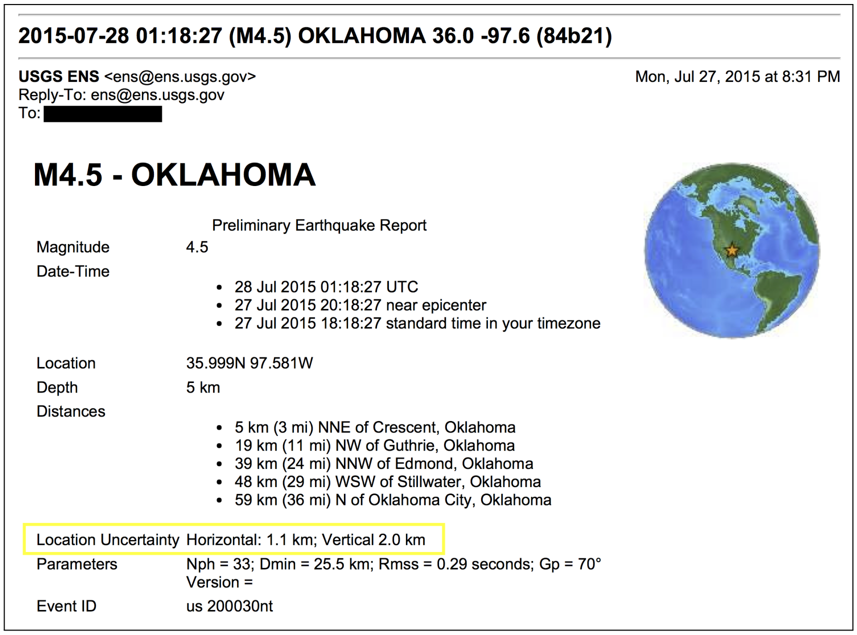

2015-07-28 01:18:27 (M4.5) OKLAHOMA 36.0 -97.6 (84b21)

USGS ENS <ens@ens.usgs.gov> Mon, Jul 27, 2015 at 8:31 PM
Reply-To: ens@ens.usgs.gov
To: [redacted]

M4.5 - OKLAHOMA

Preliminary Earthquake Report

Magnitude	4.5
Date-Time	• 28 Jul 2015 01:18:27 UTC • 27 Jul 2015 20:18:27 near epicenter • 27 Jul 2015 18:18:27 standard time in your timezone
Location	35.999N 97.581W
Depth	5 km
Distances	• 5 km (3 mi) NNE of Crescent, Oklahoma • 19 km (11 mi) NW of Guthrie, Oklahoma • 39 km (24 mi) NNW of Edmond, Oklahoma • 48 km (29 mi) WSW of Stillwater, Oklahoma • 59 km (36 mi) N of Oklahoma City, Oklahoma
Location Uncertainty	Horizontal: 1.1 km; Vertical 2.0 km
Parameters	Nph = 33; Dmin = 25.5 km; Rmss = 0.29 seconds; Gp = 70° Version =
Event ID	us 200030nt

Figure 2.10: Example ENS (Earthquake Notification System) report. Location Uncertainty indicated by the yellow box.

case spectral acceleration at a period of 1.0 s (S_1). Predictions of S_1 are made using the Campbell (2003) ground-motion attenuation model calibrated with a bias factor correlated to actual seismic station data in Oklahoma. These predictions are adjusted by a site amplification factor (Site Class D). Inspection radii are set to be the largest distance from the epicenter at which demand (S_1) exceeds capacity characterized by fragility curves of bridges. A complete table of the calculated inspection radii was presented (Table 2.3). The analysis showed that damage to bridges is unlikely (10% probability of slight damage) for earthquakes with a magnitude less than 4.6.

The recommended post-earthquake bridge inspection radii (Table 2.4) are based on a 25% probability of observing slight damage ($S_1 = 0.0556g$) and should be expanded to account for epicenter location uncertainty. Based on these recommendations, ODOT revised their protocol starting 1 April 2016. The press release (ODOT, 2016) is shown in Figs. 2.11 and 2.12.

Additionally, priority bridges were identified from the Oklahoma on-system bridge odot news

OKLAHOMA DEPARTMENT OF TRANSPORTATION

INFORMATION RELEASE

OKLAHOMA DEPARTMENT OF TRANSPORTATION, MEDIA & PUBLIC RELATIONS DIVISION
200 N.E. 21ST ST. OKLAHOMA CITY, OK 73105-3204 PHONE 405-521-6000

FOR IMMEDIATE RELEASE

Date: Thursday, March 31, 2016
Press Release # 16-012

ODOT firms up earthquake bridge inspection process

The Oklahoma Department of Transportation is relieved by the results of a recent scientific analysis showing it's unlikely that a 4.6 or less magnitude earthquake will damage transportation infrastructure in the state, including bridges. The department plans to incorporate this new information into its bridge inspection protocol starting in April.

"This is great news for Oklahomans concerned with the long-term effects of increased earthquakes in our state," said Mike Patterson, ODOT executive director. "Our department has aggressively inspected bridges and infrastructure for the past few years and learned a great deal through this process about this relatively new phenomenon in our state."

Infrastructure Engineers Inc., a team of consultants that worked closely with researchers from the University of Oklahoma, validated ODOT's inspection process. Additionally, the year-long study of earthquake data revealed there is no structural damage occurring on bridges after tremors below magnitude 4.7, indicating that bridge inspections are unnecessary below this level. The department will continue to inspect bridges after earthquakes, but starting at a threshold of 4.7 magnitude events.

The magnitude of an earthquake will determine how wide an area from the epicenter will be inspected. Starting in April, crews will respond immediately to earthquakes at these new levels:

- 4.7 to 4.8 magnitude — 5-mile inspection radius;
- 4.9 to 5.3 magnitude — 15-mile inspection radius;
- 5.4 to 5.8 magnitude — 30-mile inspection radius;
- 5.9 to 6.2 magnitude — 60-mile inspection radius; and
- 6.3-plus magnitude — 120-mile inspection radius.

Figure 2.11: ODOT Press Release # 16-012: "ODOT firms up earthquake bridge inspection process".

ODOT previously checked bridges after almost every earthquake, then adjusting later to inspect after every 3.0-magnitude event. After consulting national experts, including the California Department of Transportation, the U.S. Geological Survey and Oklahoma Geological Survey, that protocol changed in mid-2014 to inspections after every 4.0-magnitude event within a 5-mile radius of the epicenter.

“We were conservative in our approach to bridge inspections, but now we have the science to know with more certainty that 4.0- to 4.6-magnitude earthquakes present no danger to transportation infrastructure in the state,” said Casey Shell, ODOT chief engineer. “This change in protocol allows the department to better focus its resources.”

Shell said ODOT has never found any structural bridge damage in the state related to earthquakes since inspections began in 2013. Oklahoma’s bridges meet federal design standards, meaning they are meant to safely withstand some degree of vibrations and movement.

Another component of the current $575,000 study was the creation of a post-earthquake bridge inspection manual that describes best practices in detail as well as providing a step-by-step inspection guide. This comprehensive document will be used by all ODOT bridge inspectors statewide, and will be shared with other state agencies and government entities such as the Oklahoma National Guard and with counties and municipalities. Additionally, the study provided training to ODOT personnel that also will be shared with other agencies, as well as detailed structural analysis on three bridges representing those typically used in Oklahoma.

A second phase of the Infrastructure Engineers Inc. study is planned to begin next fiscal year, which will create an analytical program combining ODOT bridge data and earthquake data to help plan a localized inspection route. This will help inspectors respond even more quickly and be more cost effective while ensuring safety for motorists.

—www.odot.org—

(Editors and News Directors: For more information, call the ODOT Media and Public Relations Division at 405-521-6000.)

Figure 2.12: ODOT Press Release # 16-012: “ODOT firms up earthquake bridge inspection process” (cont.).

inventory by comparing the bridges' median S_1 values for moderate damage. A total of 353 bridges were tagged as priority: 32 high priority, 109 medium-high priority, and 212 medium priority (See Appendix B). Within the inspection radius, high priority bridges should be inspected first, medium-high priority bridges second, medium priority bridges third, and non-priority bridges last.

This chapter serves as a starting point for revising ODOT's Post Earthquake Bridge Inspection protocol; however, more in depth analysis is still needed. Chapter 3 will further assess ground motion prediction equations used for Oklahoma. Chapter 4 will validate the fragility curves for a case study bridge. Chapter 5 will develop ShakeCast-OK.

Chapter 3

Oklahoma Ground Motions

3.1 Overview

The effect of earthquakes on bridges is strongly linked to the intensity of the ground motion at the bridge site. The intensity of the ground shaking is a function of the magnitude of the earthquake and the distance from the epicenter to the site. The intensity of the ground shaking as a function of magnitude, distance, and other parameters is modeled with ground motion prediction equations, or *attenuation models*. In Chapter 2, the Campbell attenuation model was compared to Oklahoma ground motions and was shown to generally over predict ground motion intensity. This chapter will examine the eight attenuation models used to represent Oklahoma ground motions for the 2008 USGS seismic hazard map (Peterson et al., 2008). Predictions made with these models will be compared to measured ground motion intensities to assess their accuracy and appropriateness for Oklahoma. Additionally, response spectra will be calculated for seismic station data from the M5.8 earthquake near Pawnee, Oklahoma on 3 September 2016. These response spectra will be compared to the AASHTO design spectra for the station sites. Finally, the trigger value, found to replace the slight fragility curve, from Chapter 2 will be compared to slight fragility curves calculated for past Oklahoma earthquakes.

3.2 Evaluation of Current Attenuation Models

Ground motion attenuation models predict the levels of shaking from an earthquake based on the earthquake's magnitude and the distance from the epicenter of the earthquake. The attenuation models currently used to predict ground motions in Oklahoma are presented below.

3.2.1 2008 USGS Seismic Hazard Map

The 2008 USGS seismic hazard map groups Oklahoma with the New Madrid seismic zone (Peterson et al., 2008). This zone uses a weighted attenuation model that is a combination of seven different attenuation models (Table 3.1). The weights are based on the different types of models. Frankel et al. (1996) and Toro et al. (1997) are single-corner finite fault models (0.3), Silva et al. (2002) is a single-corner point-source model (0.1), Atkinson and Boore (2006) is a dynamic-corner frequency source model (0.2), Campbell (2003) and Tavakoli and Pezeshk (2005) are hybrid models (0.2), and Somerville et al. (2001) is an extended-source model (0.2) (Peterson et al., 2008).

Table 3.1: Central and Eastern United States ground motion models and weights (Peterson et al., 2008).

2008 Ground Motion Prediction Equation	Weight
Frankel et al. (1996)	0.1
Toro et al. (1997)	0.2
Silva et al. (2002)	0.1
Atkinson and Boore (2006)	
140 bar stress drop	0.1
200 bar stress drop	0.1
Campbell (2003)	0.1
Tavakoli and Pezeshk (2005)	0.1
Somerville et al. (2001)	0.2

3.2.2 Oklahoma Station Data

Acceleration time-histories from seismic stations were acquired for 80 earthquakes that had a magnitude of at least 4.0 occurring between 27 February 2010 and 21 March 2017 using Standing Order for Data (SOD) (Owens et al., 2004). A list of these earthquakes is presented in Tables 3.2–3.5. Both velocity and acceleration sensor data was collected, but if a station had both sets of data, only the acceleration senors were used so the station would not be double counted. Stations with only one direction of data recorded were not included. Additionally, each acceleration time-history was screened for obvious problems such as clipping, missing data, noise spikes, etc. which were removed from this study. This resulted in 43 sets out of the 1329 sets of station data collected being discarded. The remaining 1286 bidirectional ground motions records were used to calculate the spectral response accelerations for each ground motion. In particular, the spectral accelerations reported are the geometric mean of the two horizontal components. Of interest to this work are the 1-sec and 0.3-sec spectral accelerations (S_1 and $S_{0.3}$, respectively), which are reported in the following section.

3.2.3 Comparison

The calculated S_1 for each station were compiled and compared to predictions made with the attenuation models. Figs. 3.1–3.3 compare the station data to the eight attenuation models and the weighted model from the 2008 USGS Seismic Hazard Map. For the weighted model, the Frankel et al. (1996) tables do not calculate values for S_1 at epicentral distances less than 9 km or for magnitudes less than 4.4. Therefore, the weighted model was adjusted to not include Frankel for these situations*. This is why the weighted model line in the graphs for M4.4 and greater exhibit a very slight discontinuity at an epicentral distance of 9 km. The figures show that most of the atten-

*The weights listed in Table 3.1 were divided by 0.9 to redistribute the 0.1 originally for Frankel

Table 3.2: All stations selected for ground motion data.

Date	Time	Latitude	Longitude	Depth (km)	Magnitude*	Location
2010/02/27	22:22:27	35.553	-96.752	5	4.1[a]	Oklahoma
2010/10/13	14:06:30	35.192	-97.32	13	4.4[b]	Oklahoma
2011/11/05	07:12:45	35.55	-96.764	3.1	4.8[a]	Oklahoma
2011/11/06	03:53:10	35.532	-96.765	5.2	5.7[c]	Oklahoma
2011/11/06	04:03:42	35.521	-96.771	5	4[d]	Oklahoma
2011/11/08	02:46:57	35.531	-96.788	5	4.8[a]	Oklahoma
2012/04/03	07:34:00	34.635	-95.875	5	4.1[e]	Oklahoma
2013/04/16	06:56:29	35.686	-97.089	6.2	4.4[a]	12km ENE of Luther, Oklahoma
2013/04/16	10:16:53	35.681	-97.098	7	4.2[a]	8km ENE of Luther, Oklahoma
2013/12/07	18:10:24	35.607	-97.386	8.44	4.5[a]	9km ESE of Edmond, Oklahoma
2014/02/09	02:16:02	35.893	-97.292	5	4.1[a]	6km SSW of Langston, Oklahoma
2014/03/30	06:51:56	36.131	-97.629	4.83	4.2[a]	20km N of Crescent, Oklahoma
2014/03/30	14:09:59	36.125	-97.64	3.9	4.1[a]	19km NNW of Crescent, Oklahoma
2014/04/07	16:03:03	35.891	-97.275	5.13	4.2[a]	6km SSW of Langston, Oklahoma
2014/04/10	07:33:57	35.775	-97.483	7.04	4[a]	12km SSW of Guthrie, Oklahoma
2014/06/16	10:47:35	35.593	-97.397	5	4.3[a]	8km NNW of Spencer, Oklahoma
2014/06/18	10:53:02	35.596	-97.392	5	4.1[a]	8km N of Spencer, Oklahoma
2014/07/12	17:11:46	35.864	-97.321	4.05	4[a]	9km E of Guthrie, Oklahoma
2014/07/29	02:46:36	36.756	-98.045	5.29	4.3[a]	27km E of Cherokee, Oklahoma
2014/08/19	12:41:35	35.773	-97.468	4.51	4.4[a]	12km SSW of Guthrie, Oklahoma

*The magnitude used is distinguished by the superscript: [a]moment from a moment tensor inversion of complete waveforms at regional distances (mwr), [b]moment from a centroid moment tensor inversion of intermediate- and long-period body- and surface-waves (mwc), [c]moment from a centroid moment tensor inversion of the W-phase (mww), [d]local (ml), [e]short-period body wave (mb).

Table 3.3: All stations selected for ground motion data (cont.).

Date	Time	Latitude	Longitude	Depth (km)	Magnitude	Location
2014/09/30	03:01:25	36.224	-97.553	2.2	4^a	24km WSW of Perry, Oklahoma
2014/10/02	18:01:24	37.245	-97.955	5	4.3^a	7km SE of Harper, Kansas
2014/10/07	16:51:13	35.947	-96.764	5.28	4^a	4km S of Cushing, Oklahoma
2014/10/10	13:51:21	35.947	-96.759	5	4.2^a	4km S of Cushing, Oklahoma
2014/11/12	21:40:00	37.271	-97.621	4.03	4.9^c	13km S of Conway Springs, Kansas
2014/11/30	10:24:44	36.603	-97.607	5.68	4^a	25km SSE of Medford, Oklahoma
2014/12/14	21:18:20	36.319	-96.755	4.68	4^a	4km ESE of Pawnee, Oklahoma
2015/01/26	19:30:44	36.848	-97.702	6.86	4.2^d	5km NNE of Medford, Oklahoma
2015/01/27	11:31:09	36.262	-97.264	3.41	4.2^a	3km SE of Perry, Oklahoma
2015/01/27	15:58:40	36.629	-97.712	5	4^a	19km S of Medford, Oklahoma
2015/02/05	15:08:40	36.815	-98.291	4.38	4.2^a	8km NE of Cherokee, Oklahoma
2015/03/24	19:48:28	36.778	-98.03	6.51	4^d	26km W of Medford, Oklahoma
2015/04/04	13:21:17	36.118	-97.572	5.05	4.1^a	18km N of Crescent, Oklahoma
2015/04/08	20:52:00	35.819	-97.419	2.49	4^a	6km S of Guthrie, Oklahoma
2015/04/19	05:27:14	35.953	-97.332	3.16	4.2^a	6km W of Langston, Oklahoma
2015/04/27	22:22:17	35.918	-97.326	5.28	4.1^a	7km WSW of Langston, Oklahoma
2015/05/23	18:44:28	37.429	-98.953	5	4^a	30km SW of Pratt, Kansas
2015/06/05	23:12:47	37.265	-97.921	2.35	4.1^a	9km ESE of Harper, Kansas
2015/06/14	18:17:09	36.286	-97.522	6.28	4^a	20km W of Perry, Oklahoma
2015/06/17	19:17:08	36.285	-97.523	6.01	4.3^a	21km W of Perry, Oklahoma

*The magnitude used is distinguished by the superscript: ^{a}moment from a moment tensor inversion of complete waveforms at regional distances (mwr), ^{b}moment from a centroid moment tensor inversion of intermediate- and long-period body- and surface-waves (mwc), ^{c}moment from a centroid moment tensor inversion of the W-phase (mww), ^{d}local (ml), ^{e}short-period body wave (mb).

Table 3.4: All stations selected for ground motion data (cont.).

Date	Time	Latitude	Longitude	Depth (km)	Magnitude	Location
2015/06/20	05:10:54	35.739	-97.386	3	4^a	12km NE of Edmond, Oklahoma
2015/07/20	20:19:03	36.842	-98.259	4.08	4.4^a	13km NE of Cherokee, Oklahoma
2015/07/27	18:12:15	35.989	-97.572	5	4.5^a	4km NNE of Crescent, Oklahoma
2015/07/28	01:18:27	35.991	-97.581	5.25	4.1^a	4km NNE of Crescent, Oklahoma
2015/08/05	07:48:02	36.598	-97.692	6.02	4^d	23km S of Medford, Oklahoma
2015/08/14	21:25:40	36.831	-97.801	0.09	4.1^a	6km WNW of Medford, Oklahoma
2015/09/18	12:35:16	35.993	-96.8	0.21	4.1^a	3km WNW of Cushing, Oklahoma
2015/09/25	01:16:37	35.987	-96.787	2.89	4^a	1km W of Cushing, Oklahoma
2015/10/10	09:20:43	36.719	-97.931	5.63	4.4^a	20km WSW of Medford, Oklahoma
2015/10/10	22:03:05	35.986	-96.803	3.27	4.3^a	3km W of Cushing, Oklahoma
2015/11/07	11:11:53	36.953	-97.855	5	4.1^a	19km NNW of Medford, Oklahoma
2015/11/15	09:45:31	36.47	-98.755	5.11	4.3^a	33km NW of Fairview, Oklahoma
2015/11/19	07:42:12	36.66	-98.459	5.91	4.7^a	13km SW of Cherokee, Oklahoma
2015/11/20	22:40:40	36.948	-97.828	5	4.1^a	17km NNW of Medford, Oklahoma
2015/11/23	21:17:46	36.838	-98.276	5.03	4.4^a	11km NE of Cherokee, Oklahoma
2015/11/25	00:43:50	36.839	-98.269	4.86	4.1^e	12km NE of Cherokee, Oklahoma
2015/11/30	09:49:12	36.751	-98.056	5.63	4.7^a	26km E of Cherokee, Oklahoma
2015/12/06	01:01:41	36.47	-98.761	6.13	4^a	33km NW of Fairview, Oklahoma
2015/12/29	11:39:19	35.665	-97.405	6.53	4.3^a	6km ENE of Edmond, Oklahoma
2016/01/01	11:39:39	35.669	-97.407	5.83	4.2^a	6km ENE of Edmond, Oklahoma

*The magnitude used is distinguished by the superscript: ^{a}moment from a moment tensor inversion of complete waveforms at regional distances (mwr), ^{b}moment from a centroid moment tensor inversion of intermediate- and long-period body- and surface-waves (mwc), ^{c}moment from a centroid moment tensor inversion of the W-phase (mww), ^{d}local (ml), ^{e}short-period body wave (mb).

Table 3.5: All stations selected for ground motion data (cont.).

Date	Time	Latitude	Longitude	Depth (km)	Magnitude	Location
2016/01/06	06:19:25	36.488	-98.732	9.41	4^{d}	33km NW of Fairview, Oklahoma
2016/01/07	04:27:27	36.486	-98.741	7.09	4.4^{a}	33km NW of Fairview, Oklahoma
2016/01/07	04:27:57	36.495	-98.725	4.06	4.7^{c}	33km NW of Fairview, Oklahoma
2016/01/07	08:37:11	36.475	-98.734	6.65	4.4^{a}	32km NW of Fairview, Oklahoma
2016/01/18	12:55:56	36.276	-98.41	8.31	4.1^{d}	6km E of Fairview, Oklahoma
2016/02/13	17:07:06	36.49	-98.709	8.31	5.1^{c}	31km NW of Fairview, Oklahoma
2016/02/13	17:17:39	36.481	-98.739	5	4^{d}	33km NW of Fairview, Oklahoma
2016/03/29	04:53:01	35.99	-97.577	5.18	4.2^{a}	4km NNE of Crescent, Oklahoma
2016/04/07	22:27:30	35.662	-97.174	6.11	4.2^{d}	1km E of Luther, Oklahoma
2016/07/08	21:31:57	36.477	-98.739	7.32	4.2^{a}	32km NW of Fairview, Oklahoma
2016/07/08	22:29:38	36.475	-98.746	6.36	4.2^{a}	33km NW of Fairview, Oklahoma
2016/07/09	02:04:27	36.464	-98.758	7.24	4.4^{a}	33km NW of Fairview, Oklahoma
2016/07/17	04:17:58	36.284	-97.514	4.79	4.2^{a}	20km W of Perry, Oklahoma
2016/08/17	13:34:28	35.678	-97.079	6.06	4^{a}	10km E of Luther, Oklahoma
2016/09/03	12:02:44	36.425	-96.929	5.56	5.8^{c}	14km NW of Pawnee, Oklahoma
2016/10/21	20:26:00	36.449	-98.776	7.08	4^{a}	33km NW of Fairview, Oklahoma
2016/11/02	04:26:54	36.305	-96.666	4.35	4.4^{a}	12km ESE of Pawnee, Oklahoma
2016/11/07	01:44:24	35.991	-96.803	4.43	5^{c}	3km W of Cushing, Oklahoma
2016/11/07	07:33:59	36.456	-98.762	7.94	4.1^{e}	32km NW of Fairview, Oklahoma
2016/11/25	15:19:35	36.843	-97.752	7.89	4^{e}	4km NNW of Medford, Oklahoma

[*]The magnitude used is distinguished by the superscript: ^{a}moment from a moment tensor inversion of complete waveforms at regional distances (mwr), ^{b}moment from a centroid moment tensor inversion of intermediate- and long-period body- and surface-waves (mwc), ^{c}moment from a centroid moment tensor inversion of the W-phase (mww), ^{d}local (ml), ^{e}short-period body wave (mb).

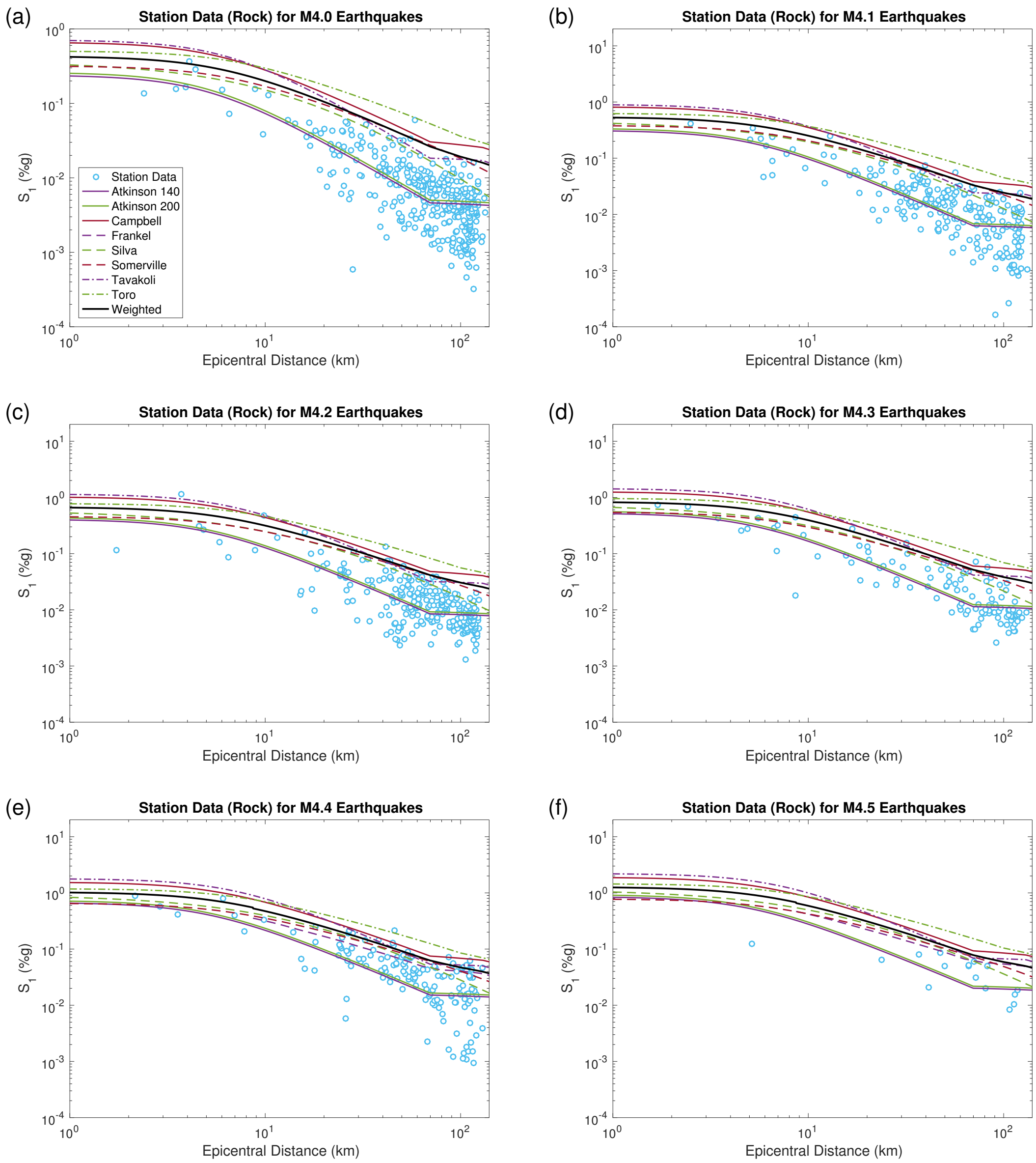

Figure 3.1: Station data compared to the eight attenuation models and the weighted model from the 2008 USGS Seismic Hazard Map.

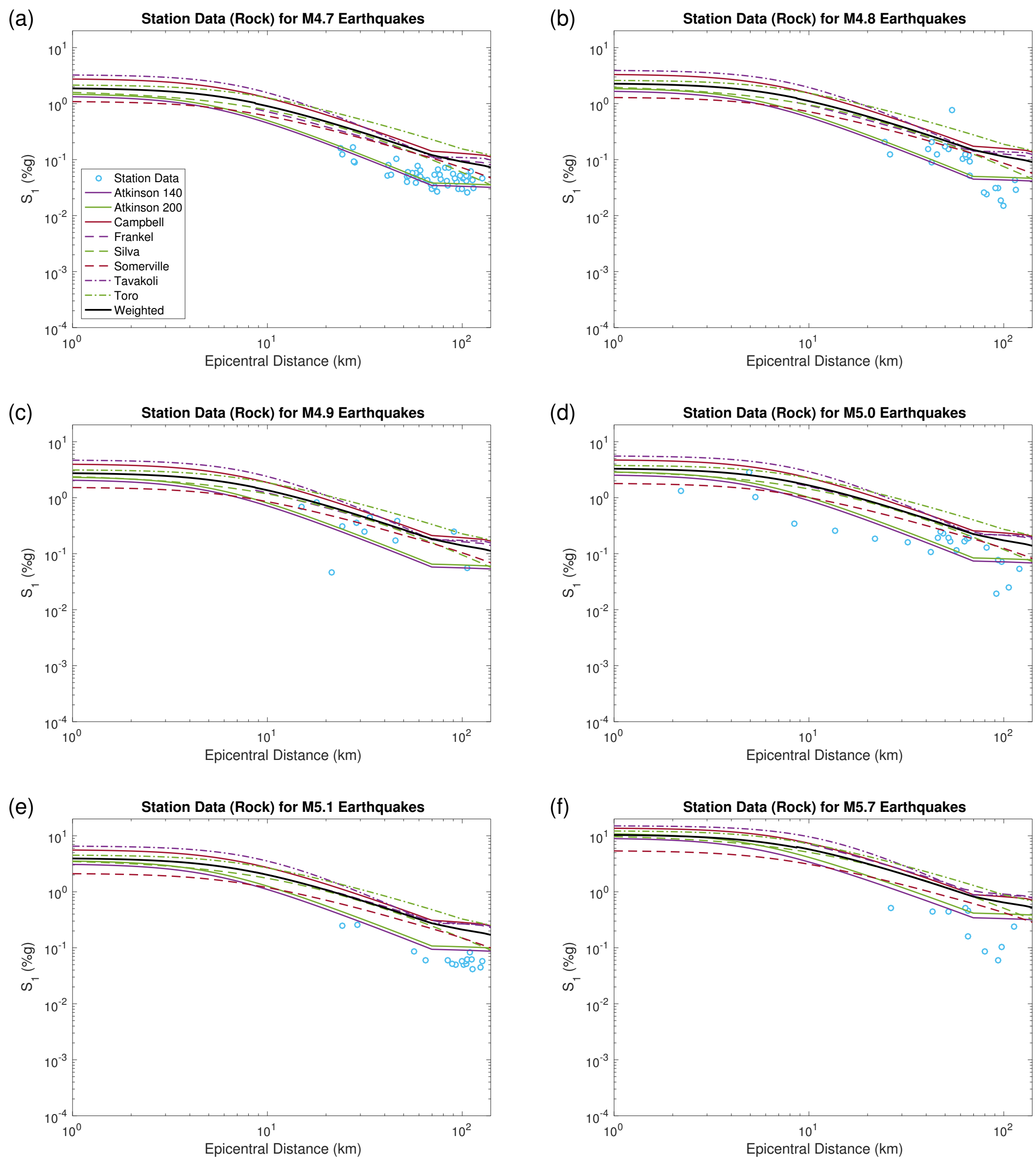

Figure 3.2: Station data compared to the eight attenuation models and the weighted model from the 2008 USGS Seismic Hazard Map (cont.).

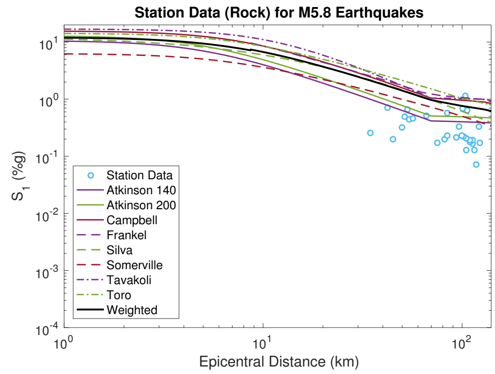

Figure 3.3: Station data compared to the eight attenuation models and the weighted model from the 2008 USGS Seismic Hazard Map (cont.).

uation models tend to over predict Oklahoma ground motions. Epicentral distance was used instead of hypocentral distance because epicentral distance is extracted from SOD and almost half of the models use epicentral rather than hypocentral distances. For the models that use hypocentral distances, a depth of 5 km was assumed.

Table 3.6 shows the root-mean-square error (RMSE) in comparing the station data to each to the models. RMSE is calculated as follows (Zwillinger, 1995):

$$\text{RMSE} = \sqrt{\frac{1}{n}\sum_{i=1}^{n}\left(\ln \hat{S}_1^{(i)} - \ln S_1^{(i)}\right)^2} \tag{3.1}$$

where n is the number of stations considered, and $\hat{S}_1^i$ and $S_1^{(i)}$ are the ith predicted and measured 1-sec spectral accelerations, respectively.

Because of Frankel's previously mentioned limitations, Frankel cannot be compared to all of the station data, so the incomparable points were omitted when computing RMSE. The RMSE values as well as the graphs show that Atkinson 140 and Atkinson 200 best predict ground motions for Oklahoma earthquakes, while Toro and Campbell do the worst.

Table 3.6: The root-mean-square error (RMSE) in comparing the station data to each model and the weighted model for M4.0-M5.8 earthquakes and the RMSE in the model compared to all earthquakes (total).

Mag.	Atkinson 140	Atkinson 200	Campbell	Frankel	Silva	Somerville	Tavakoli	Toro	Weighted	n^*
4.0	*0.793*	0.806	2.036	NaN	1.303	1.730	1.672	**2.357**	1.770	360(360)
4.1	*0.898*	0.899	1.874	NaN	1.253	1.557	1.598	**2.166**	1.626	227(227)
4.2	0.751	*0.750*	1.746	NaN	1.140	1.409	1.479	**2.052**	1.497	258(258)
4.3	0.698	*0.695*	1.616	NaN	1.012	1.231	1.414	**1.874**	1.354	110(110)
4.4	1.005	*0.993*	1.636	1.266	1.166	1.302	1.473	**1.880**	1.424	151(145)
4.5	0.738	*0.730*	1.474	0.981	0.924	1.022	1.346	**1.718**	1.124	16(15)
4.7	0.336	*0.299*	1.219	0.905	0.785	0.802	1.079	**1.541**	0.983	50(50)
4.8	0.804	*0.778*	1.302	1.108	0.899	0.922	1.211	**1.551**	1.096	23(23)
4.9	0.952	0.902	1.091	0.915	0.903	*0.807*	1.152	**1.238**	0.940	11(11)
5.0	*0.664*	0.680	1.292	1.150	0.912	0.796	1.323	**1.466**	1.074	23(19)
5.1	*0.490*	0.621	1.603	1.533	1.034	0.981	1.567	**1.775**	1.330	17(17)
5.7	*0.893*	1.036	1.672	1.757	1.438	1.189	1.730	**1.882**	1.521	10(10)
5.8	*0.767*	0.906	1.481	1.575	1.173	0.951	1.555	**1.612**	1.304	30(30)
Total	*0.808*	0.814	1.787	1.245	1.180	1.452	1.532	**2.073**	1.542	1286(1275)

*The number of stations included in calculating RMSE for all models (for Frankel and weighted models)

italics indicate the lowest RMSE for a given magnitude and **bold** indicates the highest RMSE for a given magnitude

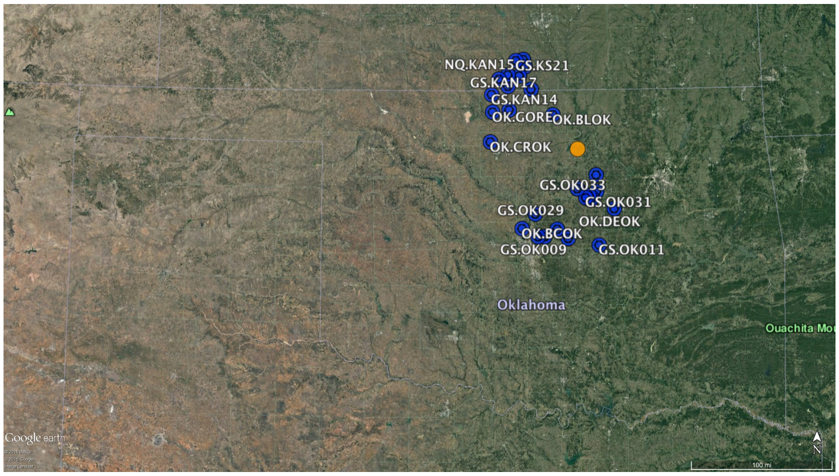

Figure 3.4: Seismic stations and their proximity to the M5.8 Pawnee earthquake epicenter.

3.3 Response Spectrum Comparisons

The largest earthquake Oklahoma has experienced to date (24 April 2017) was the M5.8 Pawnee earthquake on 3 September 2016. This earthquake had a depth of 5.6 km and occurred at a latitude and longitude of 36.4251° and −96.9291°. Response spectra were calculated from station data for this earthquake and compared to the AASHTO design spectra at the station locations.

3.3.1 Seismic Stations

Ground motion records were were retrieved from SOD (Owens et al., 2004) for all stations in the GS, NQ, and OK seismic networks within 120 km of the M5.8 Pawnee earthquake epicenter. A total of 28 stations were identified. Fig. 3.4 shows the identified stations and their location relative to the earthquake epicenter. Table 3.7 presents a list of these stations, their locations and soil conditions (V_s^{30}), as well as which channels are used. Bidirectional ground motions are considered, so both the East and North components were retained, but the vertical components were not included. For stations with a `?N?` channel code (acceleration), the earthquake data was retrieved and processed according to a modified version of the waveform recipe provided by SOD to generate a SAC file with the acceleration time-histories of each station. For stations with a `?H?` channel code (high gain seismometer measuring velocity), the earthquake data was retrieved and processed similarly to the `?N?` earthquake data and then differentiated to generate a SAC file with the acceleration time-histories of each station. These SAC files were written in Intel processor style little endian byte order, which were subsequently converted to MAT files to be read in MATLAB (Liel, 2014). Note that one

Table 3.7: Seismic stations composing the ground-motion suite.

Station	Epicentral Distance (km)	Latitude	Longitude	V_s^{30} (m/s)	Channel East	Channel North
GS.KAN01	109.6	37.1534	−97.7590	245.1	HNE	HNN
GS.KAN05	113.3	37.1087	−97.8723	254.0	HNE	HNN
GS.KAN09	100.1	37.1361	−97.6183	263.4	HNE	HNN
GS.KAN13	81.6	37.0129	−97.4778	216.0	HNE	HNN
GS.KAN14	109.6	36.9568	−97.9630	234.1	HNE	HNN
GS.KAN17	101.4	37.0441	−97.7647	236.5	HNE	HNN
GS.KS20	105.3	37.2297	−97.5543	247.9	HN2	HN1
GS.KS21	115.9	37.2865	−97.6630	258.0	HN2	HN1
GS.OK005	88.7	35.6549	−97.1911	330.2	HNE	HNN
GS.OK009	103.7	35.5813	−97.4229	319.0	HNE	HNN
GS.OK011	106.6	35.4852	−96.6858	268.0	HNE	HNN
GS.OK025	100.6	35.5811	−97.3379	278.5	HH2	HH1
GS.OK029	84.3	35.7966	−97.4549	342.2	HN2	HN1
GS.OK030	56.7	35.9278	−96.7838	317.4	HN2	HN1
GS.OK031	53.0	35.9531	−96.8391	287.2	HN2	HN1
GS.OK033	42.3	36.0444	−96.9382	311.9	HN2	HN1
GS.OK034	50.0	36.0102	−96.7132	273.7	HN2	HN1
NQ.KAN15	112.8	37.2998	−97.5727	240.4	HNE	HNN
NQ.OK914	51.6	35.9708	−96.8048	273.6	HNE	HNN
NQ.OK915	54.2	35.9535	−96.7726	329.7	HNE	HNN
NQ.OK916	84.6	36.8073	−97.7477	204.3	HNE	HNN
OK.BCOK	105.0	35.6567	−97.6093	264.8	HHE	HHN
OK.BLOK	45.2	36.7606	−97.2150	243.4	HHE	HHN
OK.CHOK	96.6	35.5611	−97.0613	285.6	HHE	HHN
OK.CROK	94.9	36.5047	−97.9834	296.9	HHE	HHN
OK.DEOK	75.4	35.8427	−96.4983	281.4	HHE	HHN
OK.QUOK	34.5	36.1714	−96.7080	335.4	HHE	HHN

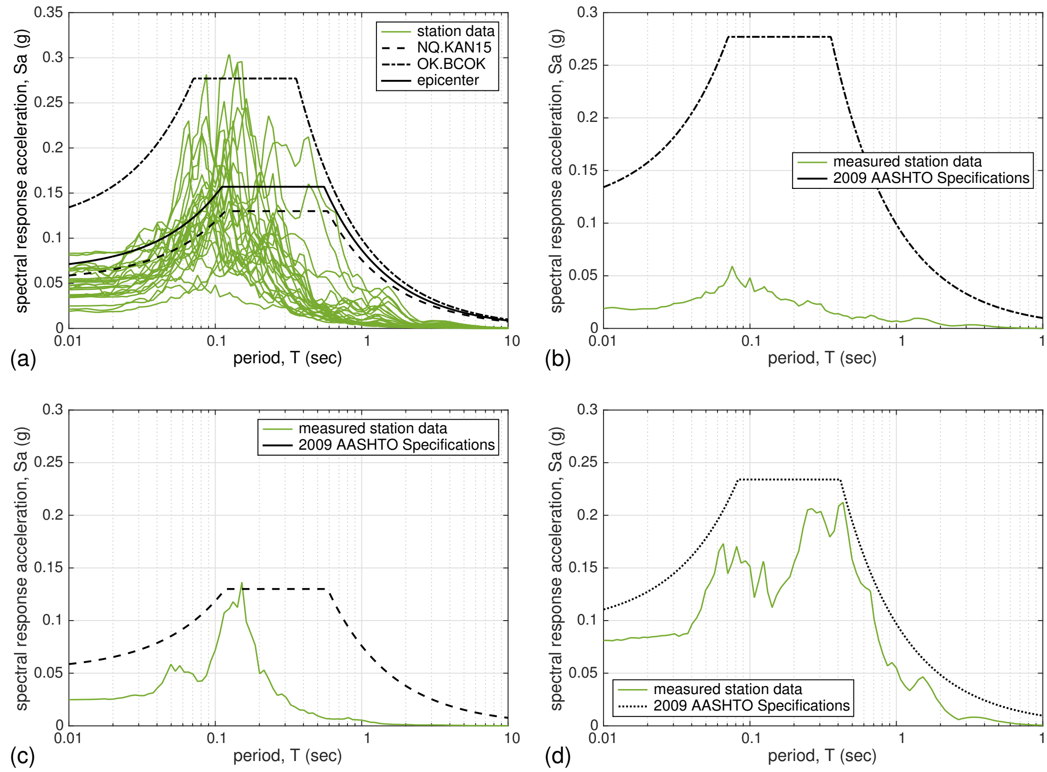

Figure 3.5: Spectral response acceleration S_a measured at seismic stations compared to the 2009 AASHTO Specifications Design Response Spectra: (a) all 27 stations including design spectra at three sites — lowest design S_a (NQ.KAN15), highest design S_a (OK.BCOK), and at the M5.8 Pawnee earthquake epicenter; (b) station OK.BCOK; (c) station NQ.KAN15; and (d) station GS.OK005.

station that was identified, OK.GORE, was omitted from this study because its data was inconsistent and potentially corrupted.

3.3.2 Ground Motion Characteristics

Fig. 3.5(a) show the response spectra for the 27 seismic stations that registered the M5.8 Pawnee earthquake. The spectral acceleration reported is the largest radial acceleration:

$$S_a(T) = \max_t \sqrt{[a_1(t;T)]^2 + [a_2(t;T)]^2} \tag{3.2}$$

where $a_1(t;T)$ and $a_2(t;T)$ are the 5%-damped acceleration responses in two orthogonal horizontal directions, in this case East and North, for a structure with period T. This is an orientation-independent measure of the spectral acceleration, as opposed to the geometric mean of the response spectra in the two directions (Boore et al., 2006). The largest spectral accelerations are observed at periods between 0.05 and 0.3 seconds. There is variation in the spectra at different sites because the stations were located at varying distances from the epicenter (Table 3.7).

3.3.3 Comparison to AASHTO Design Standards

Fig. 3.5(a) shows the spectral acceleration from each station compared to the 2009 AASHTO Specifications Design Response Spectra (AASHTO, 2009). For the sake of clarity, design spectra are shown for only three locations: the lowest design values (NQ.KAN15), the highest design values (OK.BCOK), and at the epicenter of the M5.8 Pawnee event. Because the design curves are based on the hazard from the Meers fault in Southwest Oklahoma, the design spectral accelerations are higher closer to the fault (OK.BCOK) and lower farther from the fault (NQ.KAN15). However, as can be seen from Fig. 3.5(a), this does not necessarily correspond to the intensity of the ground motions from the M5.8 Pawnee earthquake.

Fig. 3.5(b) shows that the station OK.BCOK displays a spectral acceleration curve far below its design curve, while in Fig. 3.5(c) the design curve and measured spectrum more closely match, with the measured S_a exceeding the design value at a period of about 0.15 sec. Note that there are stations between NQ.KAN15 and OK.BCOK that are closer to the epicenter but farther from the Meers fault than OK.BCOK; these stations would have design curves between OK.BCOK and NQ.KAN15 with higher measured spectra. One station of notes is GS.OK005 [Fig. 3.5(d)] whose spectrum displays longer period content than the other stations. The peak S_a is at a period of 0.43 sec, whereas the other GMs had more energy in the 0.05 – 0.3 sec range. it is also noted that this GM better matches the design spectrum than other GMs.

The mismatch between shaking levels and the design spectra at each location means that a bridge might experience shaking levels higher than it was designed for because design spectra are based on the maximum creditable earthquake and do not take into account induced seismicity. Also, the earthquakes Oklahoma is experiencing are not near the Meers fault, where the design spectra are higher.

3.4 Computing Slight Fragility Curve

The slight fragility curve cannot be calculated prior to an earthquake because K_{shape} requires actual ground motion data to calculate:

$$K_{\text{shape}} = 2.5 S_1 / S_{0.3} \tag{3.3}$$

However, using SOD and ShakeMap, S_1 and $S_{0.3}$ values from previous earthquakes can be extracted to determine whether or not the proposed trigger value (Section 2.2) is conservative. According to the HAZUS manual, the lowest unmodified median S_1 for slight damage for bridges that include K_{shape} is 60%g (FEMA, 2003).

3.4.1 Using Station Data

Using the same set of data as in Section 3.2, the $S_1/S_{0.3}$ ratio was computed for each station from each earthquake. These values were then plotted against the station distance from the epicenter (Fig. 3.6(a)) and earthquake magnitude (Fig. 3.6(b)). Examining the graphs shows that there is no correlation between magnitude or distance and $S_1/S_{0.3}$ ratio. Therefore, a single value rather than a function of magnitude or distance can be selected to represent ratios for Oklahoma. Fig. 3.6(c) shows a histogram of all the recorded ratios.

The 2.5 in Eq. (3.3) is the ratio between $S_{0.3}$ and S_1 for the standard code-based spectral shape for which the HAZUS fragility curves were derived (Mander, 1999). The fact that most of the $S_1/S_{0.3}$ ratios are less than 0.4 (1/2.5) shows that Oklahoma earthquakes tend to have higher frequency content, which causes the bridges to be have

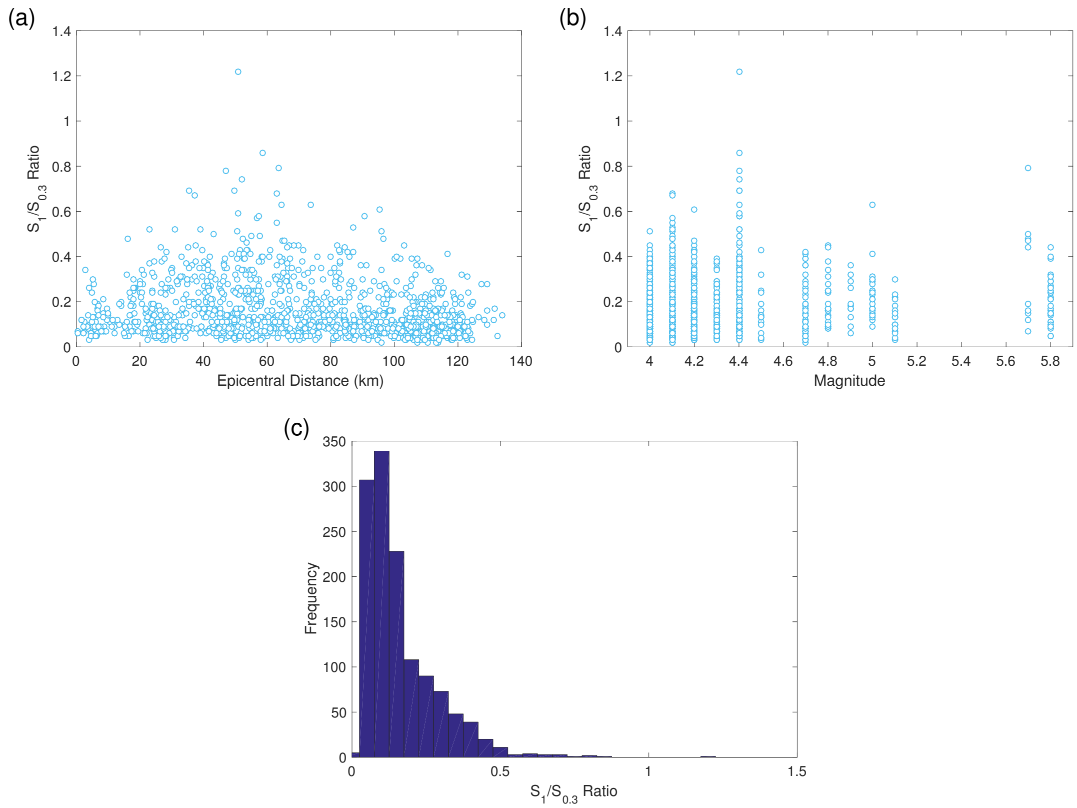

Figure 3.6: $S_1/S_{0.3}$ ratios computed at each station plotted against (a) epicentral distance, (b) earthquake magnitude, and (c) frequency of occurrence.

lower slight fragility curve medians (i.e. more vulnerable).

Knowing this distribution of $S_1/S_{0.3}$ (Fig. 3.6(c)), the probability of observing the slight damage state given ground motion intensity S_1 can be calculated as follows:

$$P(\text{slight} \mid S_1) = \int_0^{\infty} P(\text{slight} \mid S_1, \rho)\, f(\rho)\, \mathrm{d}\rho \tag{3.4}$$

where $P(\text{slight} \mid S_1, \rho)$ is the slight fragility curve and $f(\rho)$ is the distribution of the ratio $\rho = S_1/S_{0.3}$. This integral can be calculated using Monte Carlo integration (Robert and Casella, 2004). Eq. (3.4) can be approximated by the empirical average,

$$P(\text{slight} \mid S_1) \approx \frac{1}{N} \sum_{j=1}^{N} P(\text{slight} \mid S_1, \rho_j) \tag{3.5}$$

where ρ_j ($j = 1, ..., N$) are i.i.d. samples generated from the density f, taken to be

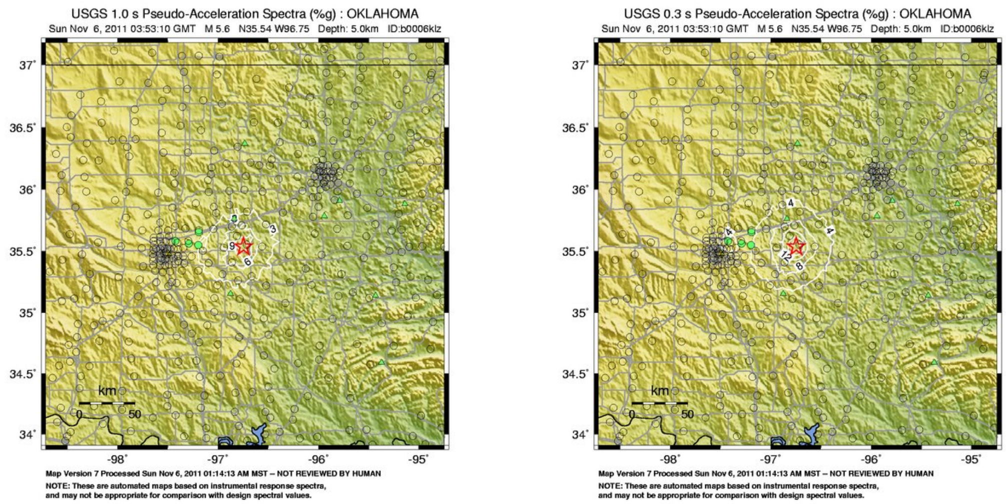

(a) (b)

Figure 3.7: ShakeMaps for the M5.7 earthquake: (a) S_1 and (b) $S_{0.3}$ (USGS, 2015b).

the measured values (Fig. 3.6(c)). Evaluating Eq. (3.5) for the trigger S_1, 5.56%g, the probability is determined to be 9%, which is below the 25% used in establishing the trigger value (Chapter 2). For bridges that do not take into account K_{shape}, the lowest base fragility curve for slight damage is 25%g (FEMA, 2003). This corresponds to a 0.6% probability of slight damage, which shows that bridges with K_{shape} are generally more at risk than those without.

3.4.2 Using ShakeMap Grid

Because station data is usually so far from the epicenter of the earthquake that the shaking levels would produce extremely low probabilities of damage, ShakeMap grid S_1 and $S_{0.3}$ values (Fig. 3.7) were used to calculate probabilities of damage. The highest probability of damage for the M5.7 and M5.8 earthquakes are 12% (Fig. 3.8(a)) and 4.8% (Fig. 3.8(b)), respectively. The probability of 12% seems unrealistically high, seeing as the next highest probability of damage is 5.4% (Fig. 3.8(c)). Because these percentages are lower than the 25% probability of damage that the trigger value is based on, the trigger value is slightly conservative.

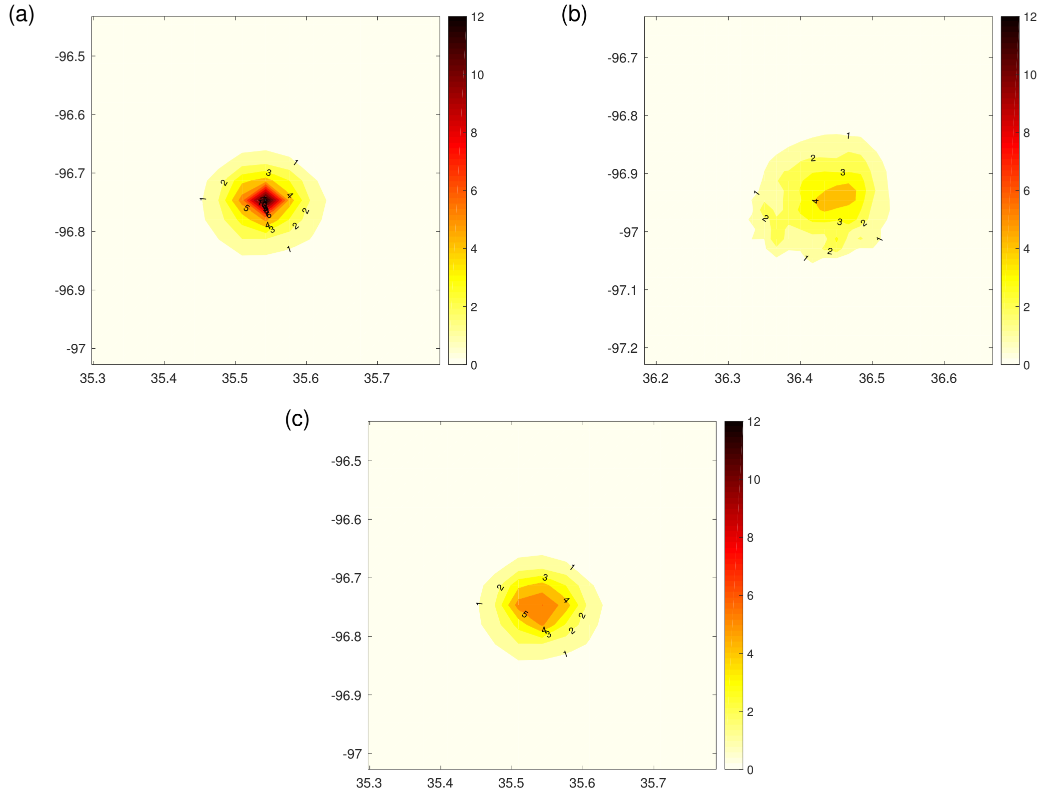

Figure 3.8: Contours of probability of slight damage based on $S_1/S_{0.3}$ ratios from ShakeMap for the (a) M5.7 earthquake, (b) M5.8 earthquake, and (c) M5.7 earthquake with outlier point removed.

3.5 Summary

This chapter compared Oklahoma station data to the attenuation models found in the 2008 USGS seismic hazard map. Most of the attenuation models overpredicted Oklahoma ground motions; however, the Atkinson and Boore (2006) model had the best fit. Then, response spectra calculated from seismic stations from the M5.8 earthquake were compared to the AASHTO spectra from those sites. Because the AASHTO spectra are based off of the Meers fault, the measured levels of shaking sometimes exceeded the design curves at locations farther from the fault. Finally, slight fragility curve values were calculated for previous Oklahoma earthquakes. The computed values showed that the trigger value that this research determined is conservative.

Chapter 4

Seismic Analysis of the I-35/Cimarron River Bridge

4.1 Overview

In Chapter 2, it was established that there are two components to determine inspection radii: demand on a bridge and capacity of a bridge. Chapter 3 further examined demand on a bridge. This chapter will further examine capacity of a bridge, using a seismic response analysis for the Interstate 35 (I-35) bridge over the Cimarron River as a case study.

The I-35 bridge over the Cimarron River (NBI 145170000000000 and 14518-0000000000) is located approximately 40 miles north of Oklahoma City in Logan County, Oklahoma (35.9860° N, −97.3530° W). The bridge's median S_1 values for moderate, extensive, and complete damage as determined by HAZUS are $0.48g$, $0.67g$, and $0.87g$, respectively. Fig. 4.1 shows a photo of the I-35 bridge over the Cimarron River.

The Oklahoma Department of Transportation selected the I-35 bridge over the Cimarron River for this study because (a) it is a *route critical* bridge along the I-35 corridor and (b) it is a *skew* bridge. This chapter describes our seismic study and provides conclusions to understand the seismic performance of this bridge and to help determine the level of effort involved in performing similar studies for other bridges. The results from this study can also be used to verify and adjust the parameters used in the HAZUS fragility curves that are critical in developing the Interim Response Protocol (Chapter 2), as well as ShakeCast-OK (Chapter 5). The goals of this study are as follows:

- Estimate the seismic fragility of the bridge per HAZUS fragility values (FEMA, 2003).

- Review available design plans of the bridge layout and develop analytical models of bridge components from the plans.

- Construct a detailed non-linear finite element model of the bridge in *OpenSees* (McKenna and Feneves, 2000), including superstructure components, substructure components, and bearings.

- Perform an eigenvalue analysis using *OpenSees* to extract the first 100 natural periods and accompanying mode shapes.

Figure 4.1: Photo of the I-35 bridge over the Cimarron River.

- Establish capacities of the concrete columns (flexural) and bearings (deformation) incorporating survey data from bridge inspectors.

- Perform time-history simulations with the finite element model for five ground motions matched to a 7% probability of exceedance in 75 years response spectrum applied longitudinally and then transversely.

- Perform time-history simulations with the finite element model for five ground motions matched to a 2% probability of exceedance in 50 years response spectrum applied longitudinally and then transversely.

- Compare the results of the time-history simulations to the established capacities to assess for damage and identify potential weak points in the structure.

4.2 Bridge Layout

Figs. 4.2 and 4.3 show the general elevation and plan of the I-35 bridge over the Cimarron River. The I-35 bridge over the Cimarron River comprises a northbound bridge and a southbound bridge, each comprised of eight spans consisting of two 101-ft spans, two 100-ft 9-in. spans, and four 100-ft spans for a total length of 803 ft 6 in. The eight spans are divided into two continuous four-span segments. The width of each span is 42 ft $4^1/_2$ in. Each span is constructed of eight built up steel girders for end and center spans; see Appendix C.1.

The girders for the north end spans bear on an abutment supported on piles at one end and bents at the other end, and the girders for the south end spans bear on an abutment supported on shallow spread footing foundation at one end and bents at the other end. The girders in the center spans are supported at each end by reinforced concrete bents. Note that the bridge underwent a widening in 1978, and the substructure consists of a multi-column bent and a single-column bent, as shown in Fig. 4.4. Each bent for

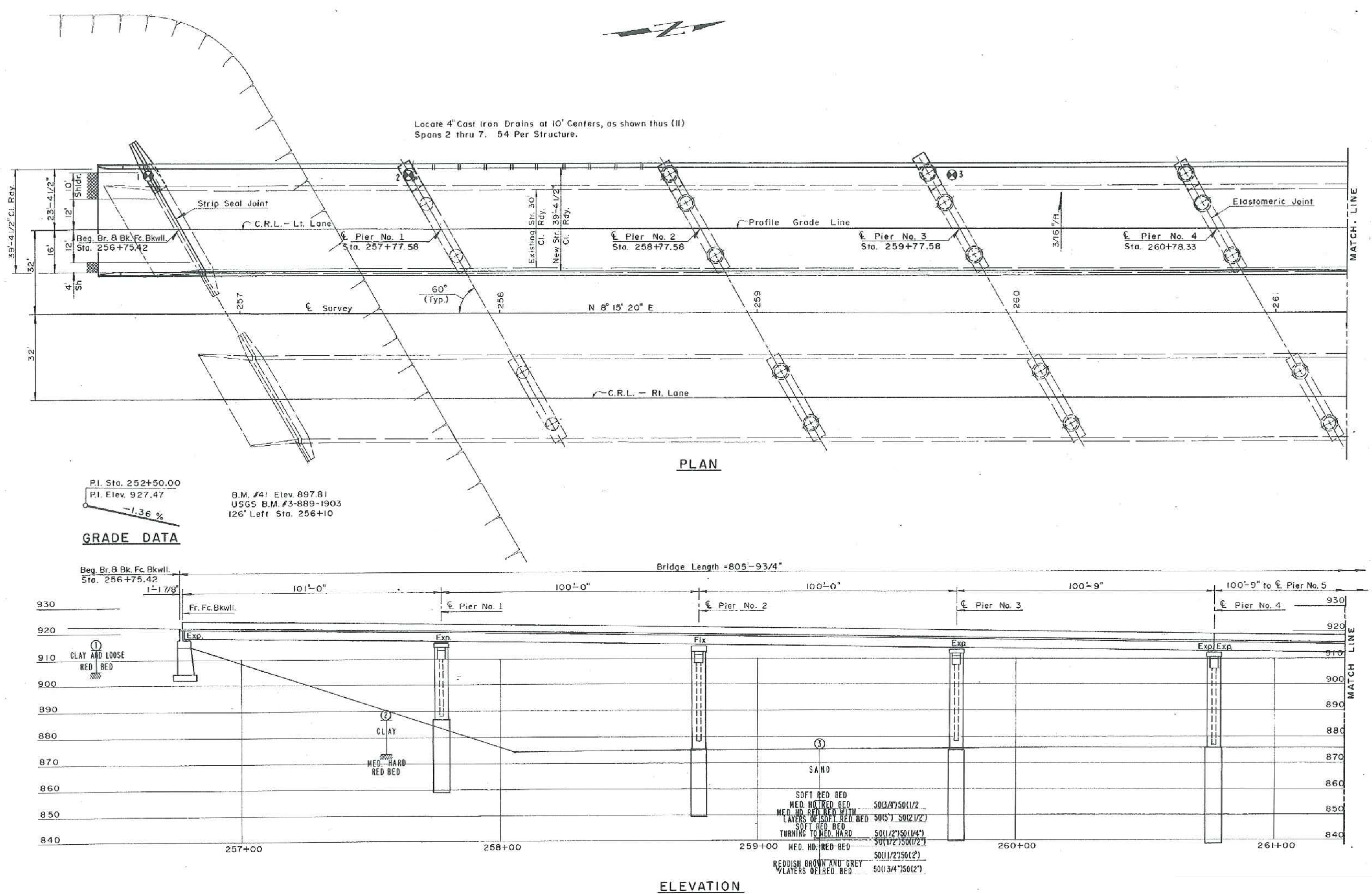

Figure 4.2: General elevation and plan of the I-35 bridge over the Cimarron River — South abutment and Piers 1–4. Taken from Proj. No. I–FI–35–4(97)166 plans.

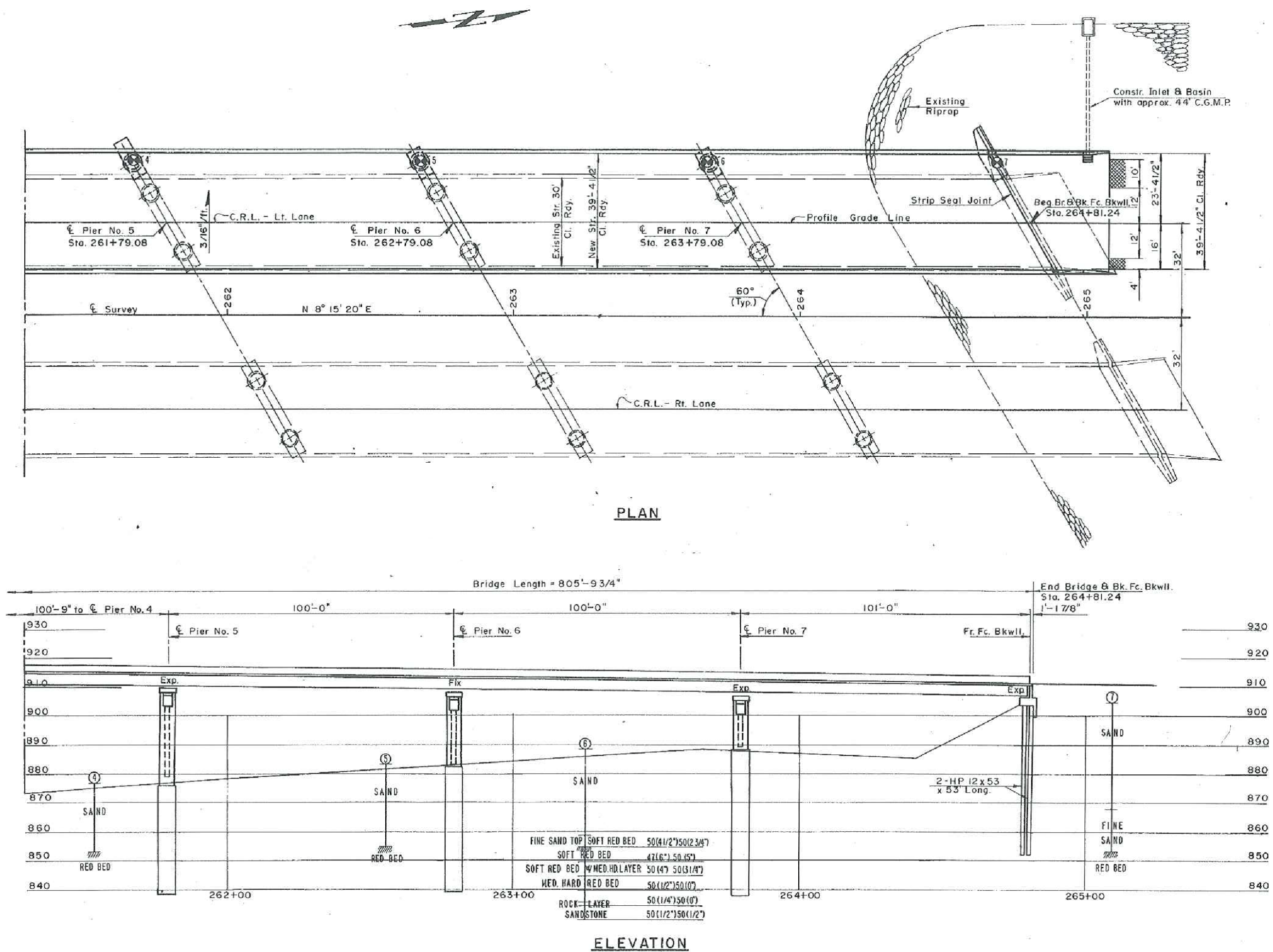

Figure 4.3: General elevation and plan of the I-35 bridge over the Cimarron River — Piers 5–7 and North abutment. Taken from Proj. No. I–FI–35–4(97)166 plans.

this bridge consists of a T-shaped 5-ft 3-in. or 5-ft wide by 6-ft deep reinforced concrete bent beam supported by three 60-in. diameter circular reinforced concrete columns; see Appendix C.2. The columns range in above ground height of between 24 and 32 ft. The end and intermediate supports are at a 30° angle with the longitudinal axis of the bridge; the effects of *skew* on the response of bridges have been shown to be more significant for skew angles greater than 20°. The layout and configuration of the northbound bridge and southbound bridge are the same.

Fixed high-type steel, expansion roller, and expansion-type elastomeric bearings are used on this bridge. The high-type steel bearings, shown in Fig. 4.5(a), are used at the second and sixth piers.* This bearing includes a sole plate and keeper plate to which the girder is attached. The combination of a rocker plate, a web plate, and web stiffeners form the bearing. Two anchor bolts attach the bearing to the bent.

The roller bearings, shown in Fig. 4.5(b), are used at both abutments and the first, third, fifth, and seventh piers. This bearing is made of an extra strong pipe with a square bar attached across the opening of each end of the pipe and connected to the opposite

*Refer to Figs. 4.2 and 4.3 for pier numbering.

Figure 4.4: Photo of bridge substructure.

bar by a stiffener plate. The bar rests in a notch at each end of the bottom plate to keep the pipe from rolling too far. A sole plate connects the girder to the bearing and two anchor bolts connect the bottom plate to the pier.

Two elastomeric bearings, as shown in Fig. 4.5(c), are used at the fourth pier. The end of each of the two girders rests on an elastomeric bearing pad. Two anchor bolts set into the bent cap are inserted through a slot in the anchor plate. Appendix C.3 shows the bearing details.

4.3 Analytical Models of Bridge Components

The analytical bridge model developed in this study has a reasonable degree of fidelity and therefore requires a significant amount of detail in modeling the various bridge components. These components are classified into one of three main categories: (i) superstructure which consists of girders, deck slab, and parapets; (ii) substructure which consists of abutments, bents (beams and columns), shear walls, footings, and foundations (piles); and (iii) bearings whose primary responsibility is to tie the superstructure to the substructure. The models of these bridge components were created in the analysis software *OpenSees*, which was initiated and is maintained by the Pacific Earthquake Engineering Research (PEER) Center (McKenna and Feneves, 2000). Fig. 4.6 depicts the node layout for the entire I-35 bridge over the Cimarron River. Nearly 5000 nodes

Figure 4.5: Photos of bearings used in the I-35 bridge over the Cimarron River: (a) fixed high-type steel bearing; (b) roller bearing; (c) expansion elastomeric bearing.

were used in the model to represent the bridge components.

4.3.1 Bridge Superstructure

The superstructure of the bridge refers to the portion of the bridge located above the bearings. In general, this consists of a set of girders with a thin concrete deck cast on top. The deck elements were modeled in *OpenSees* by using elastic shell elements and the girder elements were modeled using 5-ft elastic beam elements. The superstructure is expected to remain linearly elastic under seismic loading (cracking was not modeled nor was the deck joint at pier 4).

The superstructure details for the I-35 bridge over the Cimarron River are shown in Fig. C.1 (Appendix C.1). Note that this bridge underwent a widening in 1978, and the "Finished Bridge" in its present configuration is the one modeled here. The concrete deck is 6.5 in. thick and has an assumed density of 150 pcf. The steel girders are constructed of built-up plate sections. The properties are: cross sectional area ranging

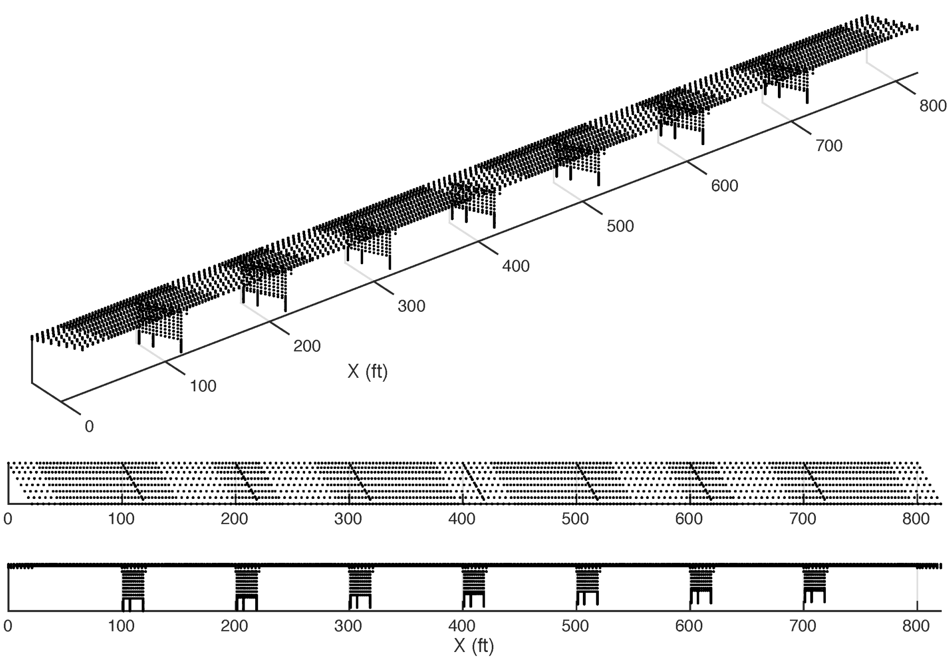

Figure 4.6: Nodes in the finite element model of the I-35 bridge over the Cimarron River.

between 43.75 and 69.75 in.^{2}, moment of inertia of between 8,754 and 20,696 in.^{4}, density of 490 pcf and a distance from the bottom to neutral axis of girder between 15 and 19 in.

4.3.2 Bridge Substructure

The substructure of the bridge refers to the portion of the bridge located below the bearings. In general, this consists of abutments, foundations, and bents (beams and columns). The bents were modeled in detail for the finite element analysis of the bridge structure, but soil-structure interactions were not modeled; i.e., fixed conditions were assumed at the top of the drilled shafts and abutments. Additional modeling, including rotational and translation springs to represent the soil (substructure method) or fully coupling the structural model with a detailed finite element model of the soil (direct method), could increase the fidelity of the model, but the inclusion of soil-structure interaction is outside the scope of this work.

Multi-column Concrete Bents

Bridge piers (or bents) are substructure components which act as intermediate vertical and horizontal supports for bridge decks. In this case, the bridge bent configuration consists of multiple concrete columns which are supported on drilled shafts. The tops of the columns are joined by a reinforced concrete bent beam (pier cap), used to provide support for the bridge girders, and the columns are connected through their height with shear walls. Fixed conditions were assumed at the bottom of the columns (i.e., at the top of the drilled shaft / soil surface).

Fig. 4.7 depicts the node layout for the multi-column concrete bents. The finite element model included nodes for the bent beam, columns, and shear wall, which were connected by a combination of fiber elements and elastic shell elements, as described below.

Analytical Modeling of Concrete Bents The concrete bents were modeled in *OpenSees* using a combination of displacement-based beam column elements (*dispBeamColumn*) and rigid links (*rigidLink*). The section properties for the columns and the bent beams were created using fiber elements with appropriate constitutive models for both the concrete and the steel reinforcement. Fiber elements allow the creation of a composite section which consists of different materials located at various spacial locations. Rigid links were used to connect the neutral axis of the bent to the top of the bent, the columns, and the shear walls.

Material Models Reinforced concrete sections were constructed from three materials, namely unconfined concrete, confined concrete and reinforcing steel. The unconfined concrete behavior was modeled using the *Concrete01* material as provided in *OpenSees*. This material uses the Kent-Scott-Park model (Scott et al., 1982) which utilizes a degraded linear uploading/reloading stiffness and a residual stress. A concrete peak compressive stress of 4.0 ksi occurs at an associated strain ϵ_o = 0.002.

The model for the confined concrete, which is inside the transverse shear reinforcing steel cage, is slightly different from that of the unconfined (cover) concrete. This

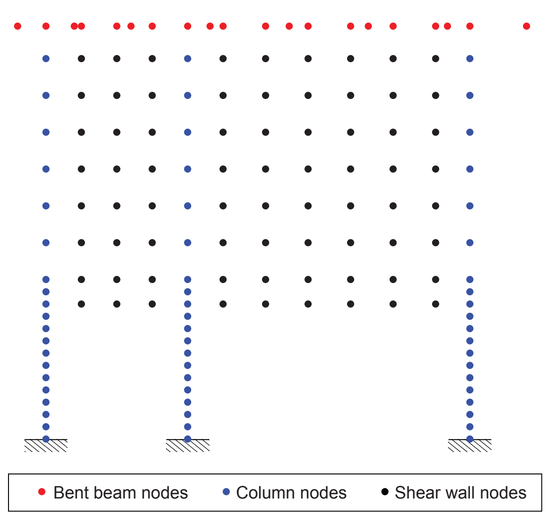

Figure 4.7: Multi-column concrete bent nodes.

is because the confinement of concrete by transverse shear reinforcement results in a significant increase in both the strength and ductility of compressed concrete (Mander et al., 1988). The maximum stress and associated strain for the confined concrete is given as Kf_c' and $\epsilon_o = 0.002K$ respectively, for which

$$K = 1 + \frac{\rho_s f_{yh}}{f_c'} \tag{4.1}$$

where f_c' is the unconfined compressive cylinder strength, ρ_s is the ratio of volume of steel hoops to volume of concrete core measured to the outside of the peripheral hoop, and f_{yh} is the yield strength of the steel hoops (Park et al., 1982).

For the columns, the transverse shear reinforcement is provided by #4, grade 60 stirrups spaced 12 in. on center. For a 60-in. diameter circular column with 4-in. cover, $\rho_s = 4.02 \times 10^{-3}$, which results in a K value of 1.060. Therefore, the confined compressive strength and associated strain are equal to 4.24 ksi and 2.12×10^{-3}, respectively.

The reinforcing steel is assumed to have a yield strength $f_{ys} = 60$ ksi and an elastic modulus $E_s = 29{,}000$ ksi, and is modeled as an uniaxial bilinear steel material object with kinematic hardening (*Steel01*). A strain hardening ratio of 0.018 was used for this material.

Analytical Model of Concrete Columns The elements for the columns were generated using displacement beam-column elements (*dispBeamColumn*) that have an associated fiber section being representative of the true column section. The bridge bents use 60-in. diameter circular columns with vertical reinforcing bars. The vertical reinforcement consists of 16-#9 bars.

A moment-curvature analysis of the reinforced concrete section at the bottom of the column was performed. Given the geometry of a column section and reinforcement, the moment-curvature interaction diagram of a column section was determined. The nonlinear characteristics of a column section are affected by the axial force acting on

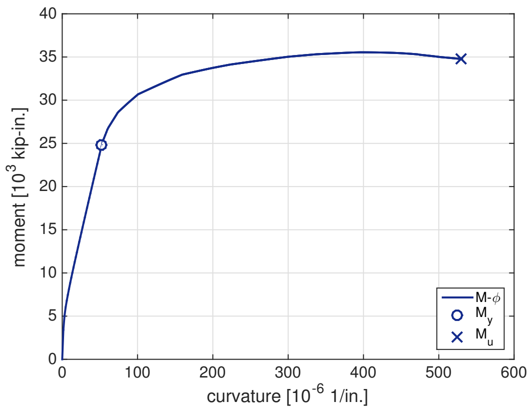

Figure 4.8: Moment-curvature relationship for reinforced concrete columns.

the column; the axial force from dead load (202 kips) was used. The moment-curvature relation of a column section is shown in Fig. 4.8. The moment M_y and curvature ϕ_y at the first yielding — that is, when the vertical reinforcing bars reach the steel yield strength for the first time — are indicated in the figure, as well as the ultimate capacity M_u of a column section and corresponding curvature ϕ_u. Yield and ultimate moments and curvatures for the columns are given in Table 4.1.

Analytical Model of Concrete Bent Beam The section for the concrete bent beam is created in the same way as for the circular columns; i.e., displacement beam-column elements with fiber sections. The bent beam has a T-shape (Fig. C.2): a combination of two rectangular sections that are 36-in. wide by 54-in. tall and 63-in. wide by 18-in. tall and employ 7-#11 (bottom steel), 7-#10 (top steel), and 6-#4 (side steel), grade 60 reinforcing bars with 2-in. cover. Non-symmetric behavior of the beam is present due to the non-symmetric distribution of the reinforcing steel. It should be noted that this beam section was assumed for the entire length of the bent beam.

Table 4.1: Moment-curvature values for reinforced concrete columns.

P (kip)	M_y (kip-in.)	ϕ_y (10^{-6} 1/in.)	M_u (kip-in.)	ϕ_u (10^{-6} 1/in.)
202	24800	52.5	34800	530

Analytical Model of Concrete Shear Walls Between columns, there is a concrete shear wall. The shear wall is 18 in. thick and is modeled using an elastic shell element, similar to the bridge deck. For piers one and seven, the shear wall extends from the bottom of the bent to 10 ft above the column bottom. For the other piers, the shear wall extends from the bottom of the bent to 11 ft above the column bottom. The shear wall is connected to the bent and columns using rigid links elements (*rigidLink*) found in *OpenSees*.

4.3.3 Bridge Bearings

A bridge bearing is a mechanical system that permits movement or transfers loads from the superstructure of the bridge to the substructure or support system of the bridge. They are typically responsible for transmitting both vertical and horizontal loads to the substructure. The forces applied to a bridge bearing mainly include superstructure self-weight, traffic loads, wind loads and earthquake loads. They become a significant factor in the overall response and functionality of a bridge before and after loading.

High-Type Steel Bearings

The high-type steel bearing is a fixed bearing. In both the longitudinal and transverse directions, high-type steel bearings were modeled using a combination of the *Steel01* and *Hysteretic* materials found in *OpenSees*. The bearings were modeled according to Nielson (2005). The normal force on the bearings was found to be 59.7 kips. In the longitudinal direction, the coefficient of friction (μ), initial stiffness, and hardening ratio were taken to be 0.21, 491.7 kip/in., and 0.06, respectively (Nielson, 2005). In the transverse direction the coefficient of friction, the initial stiffness, and hardening ratio were taken to be 0.375, 1235.7 kip/in., and 0, respectively. Fig. 4.9 shows the analytical force-deflection relationship for the high-type fixed bearings in both the longitudinal and transverse directions.

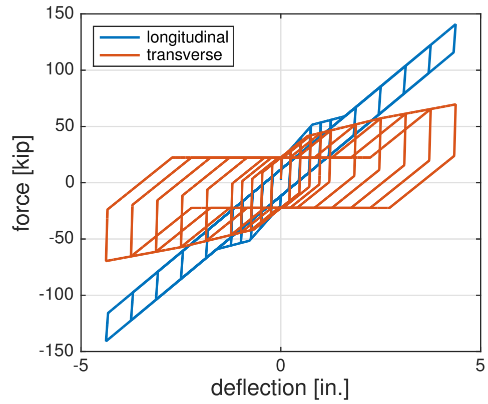

Figure 4.9: Longitudinal and transverse force-deflection responses for high-type fixed bearings.

Roller Bearings

The roller bearing is an expansion bearing. In both the longitudinal and transverse directions, it was modeled using the *Steel01* material found in *OpenSees*. The roller bearing was modeled in the longitudinal direction according to Mazroi et al. (1982). For the abutments, the normal force on the bearings due to the weight of the deck and girders was found to be 29.8 kips which results in a μ of 0.006. For piers one, three, five, and seven, the normal force on the bearings due to the weight of the deck and girders was found to be 59.7 kips which results in a μ of 0.007. Zero was assumed for the hardening ratio and 0.05 in. was assumed for the deflection used to find the initial stiffness. Mazroi et al. (1982) did not model roller bearings in the transverse direction, so the bearing was assumed to have the same transverse properties as the high-type steel bearing, i.e., μ was taken as 0.375. The normal forces and deflection were taken to be the same as in the longitudinal direction. Fig. 4.10 shows the analytical force-deflection relationship for the roller bearings in both the longitudinal and transverse directions located at (a) the North and South abutments and (b) piers 1, 3, 5 and 7.

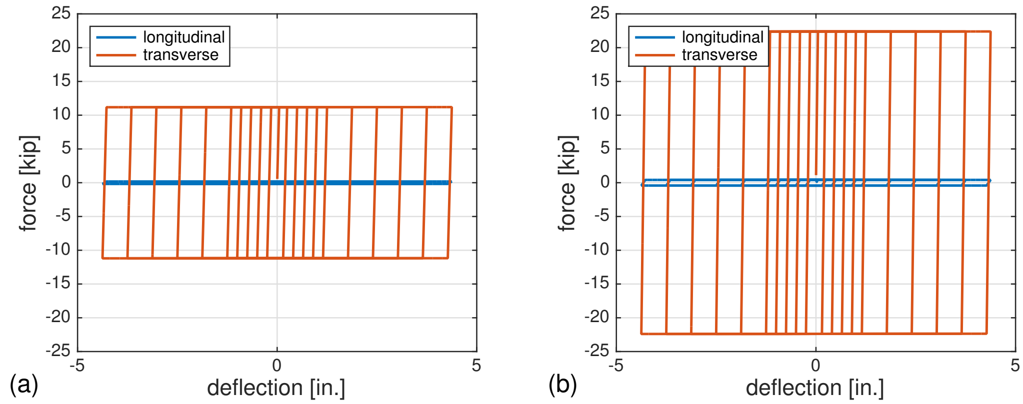

Figure 4.10: Longitudinal and transverse force-deflection responses for roller bearings located at (a) North and South abutments, (b) piers 1, 3, 5 and 7.

Elastomeric Bearings

Elastomeric bridge bearings are a common bearing used on concrete girder and slab type bridges. These types of bearings consist of an elastomeric rubber pad and anchor bolts for restraint that are embedded into the pier cap and project through steel plates attached to the underside of the girder. Each component of the bearing system provides a distinct contribution in the transfer of forces. The elastomeric pad transfers horizontal load by developing a frictional force while the anchor bolts provide resistance through a beam type action. Models of the pad and the anchor bolts are developed separately and then combined in parallel to get the appropriate composite action.

The bearing dimensions are presented in Fig. C.3. Each consists of a 60-durometer elastomeric pad that is $7^1/_2$-in. wide by 15-in. long and 4-in. thick. It has two $1^1/_4$-in. diameter anchor bolts (#11 bars) that are inserted into a slot that is $1^5/_8$ in. by 5 in.

Elastomeric Pad The behavior of the elastomeric pad is characterized initially by shearing, while sliding controls at large deformations; the modeling of the elastomeric pad was accomplished by using a *Steel01* material in *OpenSees*. The *Steel01* material was used to construct a uniaxial bilinear steel material object with kinematic hardening described by a non-linear evolution equation. The initial shear stiffness of the bearing and also the calculation of an appropriate coefficient of friction are fundamental values that should be determined for modeling of the elastomeric pad. The initial stiffness, k_o, can be calculated as follows (Schrage, 1981):

$$k_o = \frac{GA}{h_r} \tag{4.2}$$

where A is the area of the elastomeric bearing, G is the shear modulus of the elastomeric pad and h_r is the thickness of the elastomeric pad. The elastomeric pads are 60 durometer, for which the shear modulus G is in the range 130–200 psi, with an average value of 165 psi.

The frictional coefficient for concrete bridges takes into account the interface between the elastomeric rubber and a concrete surface. Schrage (1981) showed that the coefficient of friction for an elastomeric bearing is a function of the normal stress on the bearing, σ_m, and is given by

$$\mu = 0.05 + \frac{0.4}{\sigma_m} \tag{4.3}$$

where μ is the coefficient of friction and σ_m is the normal stress on the bearing given in MPa. The normal force on each bearings was found to be 29.8 kips. The coefficients of friction μ for the bearings are given in Table 4.2.

Anchor Bolts The anchor bolts are used to prevent excessive movement between the girders and the piers, on which they bear. Each girder requires two anchor bolts at each end. The anchor bolts are embedded into the top of the concrete pier cap and project out and through anchor plates attached to the underside of the girder. Under working loads the response of these anchor bolts is expected to remain linear. However, for moderate

Table 4.2: Elastomeric bearing pad properties.

Location	**A (in.^{2})**	**h_r (in.)**	**k_o (kip/in.)**	**σ_m (psi)**	**μ**	**F_y (kip)**
Pier 4	112.5	4	4.64	267	0.268	8.03

earthquakes, a non-linear behavior is expected.

In work performed by Vintzeleou and Tassios (1987), it was shown that there is extreme pinching in the hysteresis when a dowel is loaded as a cantilever, as is the case for elastomeric-type bearings. There was also an obvious drop off in strength as the dowels fractured. In order to construct in *OpenSees* a uniaxial bilinear hysteretic material object with pinching of force and deformation, as well as, damage due to ductility and energy dissipation, we estimated the yield and ultimate strength of a #11 anchor bolt acting in cantilever action with 1-in. length. For a single bolt, the estimated yield and ultimate strengths are approximately 34.2 and 34.5 kips, respectively. The yield deformation is taken to be 0.05 in. and the deformation at failure is 0.10 in.

Analytical Model of Elastomeric Bearing The composite behavior of an elastomeric bridge bearing is achieved by combining the behavior of the elastomeric pad and two anchor bolts in parallel. The elastomeric pad is represented and modeled in *OpenSees* by using a *Steel01* material with an initial stiffness k_o and yield force F_y given in Table 4.2.

The anchor bolt behavior is modeled in *OpenSees* by using a hysteretic material with yield strength of 34.2 kips. The 1¼-in. bolts are inserted into 1⅝-in. by 5-in. slots. The slot allows a total of ⅜ in. of transverse movement and 3¾ in. of longitudinal movement without initiating the effects of the anchor bolts. This condition is simulated by placing a 3⁄16-in. transverse gap and 1⅞-in. longitudinal gap on each side of the hysterisis; this gap is represented in *OpenSees* by using an elastic-perfectly plastic gap material (*ElasticPPGap*). Fig. 4.11 shows the analytical force-deflection relationship for the elastomeric bearings in both the longitudinal and transverse directions.

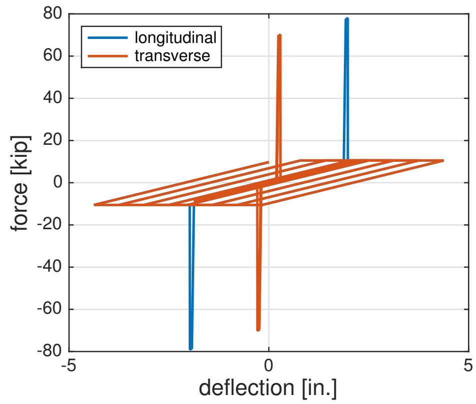

Figure 4.11: Longitudinal and transverse force-deflection responses for elastomeric bearings.

4.4 Modal Properties

The modal properties of bridges are a useful way to classify their general characteristics. An eigenvalue analysis of the I-35 bridge over the Cimarron River using *OpenSees* extracted the first 100 natural periods and accompanying mode shapes. Fig. 4.12 shows these periods.

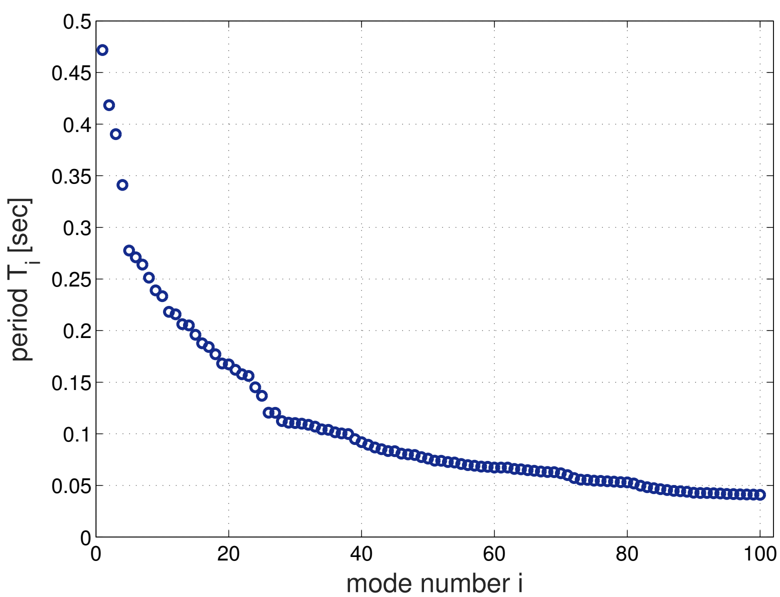

Figure 4.12: First 100 natural periods of the I-35 bridge over the Cimarron River.

The analysis reveals that the bridge's fundamental (1st) period is approximately 0.47 seconds with the predominant motion being in the longitudinal direction. This mode shape is presented in Fig. 4.13 and confirms the longitudinal nature of this mode. Longitudinal motion occurs in spans 1–4, which correspond to the tallest columns. Motion in all four spans is simultaneously activated because these spans represent a 4-span continuous deck segment. In addition to the deck moving in a rigid body mode, bending in the columns is activated as well.

The 2nd mode is the first flexural mode (Fig. 4.14). Most of the modes of the bridge demonstrate predominately flexural behavior. The 3rd mode is the first mode to show rotation; however, this mode also demonstrates flexural behavior. The best examples of rigid-body modes with rotation as the predominant motion are modes 23 and 25; Fig. 4.15 shows the 23rd mode shape. The 19th mode is one of the more interesting modes of the bridge. It demonstrates bending in the columns of pier 4 (Fig. 4.16).

4.5 Seismic Response Analysis

As part of the seismic response analysis, transient time-history bridge responses were calculated for ground-motion records that are representative of the seismic characteristics of the site. A suite of five ground motions (GMs) at two hazard levels were considered (i.e., a total of 10 GMs). The response of the columns and bearings were recorded, and the results are presented. Maximum responses (column curvatures and bearing deflections) are presented, from which conclusions on the state of the bridge are drawn.

4.5.1 Ground Motions

Earthquake acceleration time histories previously determined by Liao et al. (2016) for this site are used. Liao et al. (2016) performed a deaggregation analysis using the computer program *EZ-FRISK v7.62* in order to estimate the controlling earthquake magni-

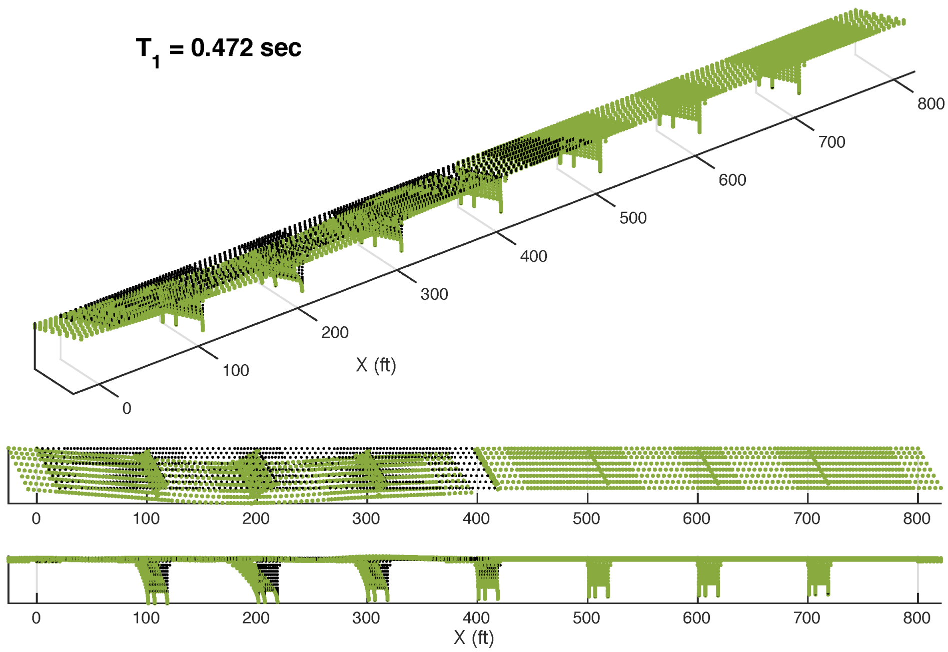

Figure 4.13: 1st mode of the I-35 bridge over the Cimarron River.

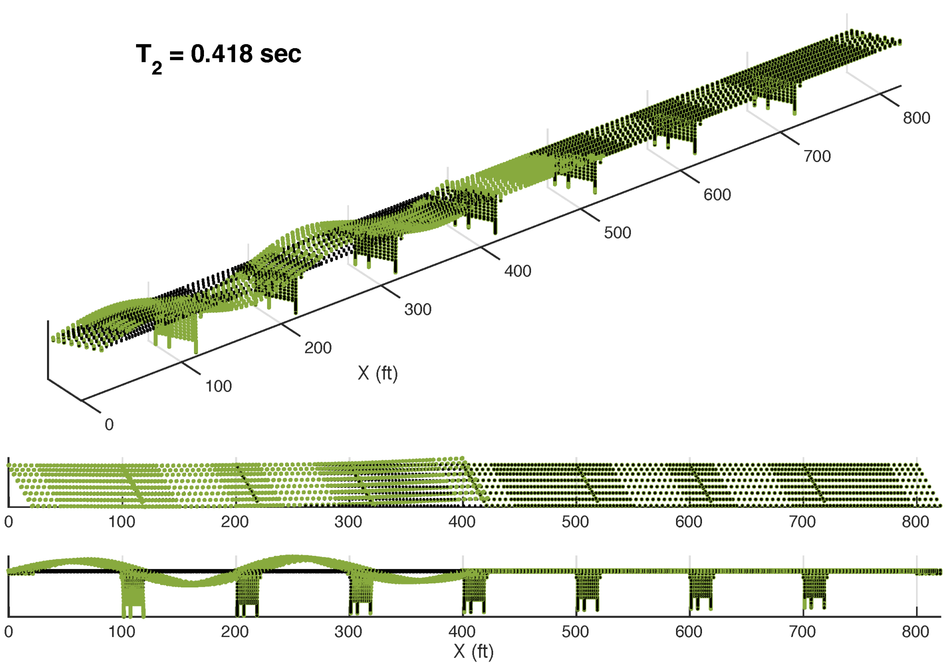

Figure 4.14: 2nd mode of the I-35 bridge over the Cimarron River.

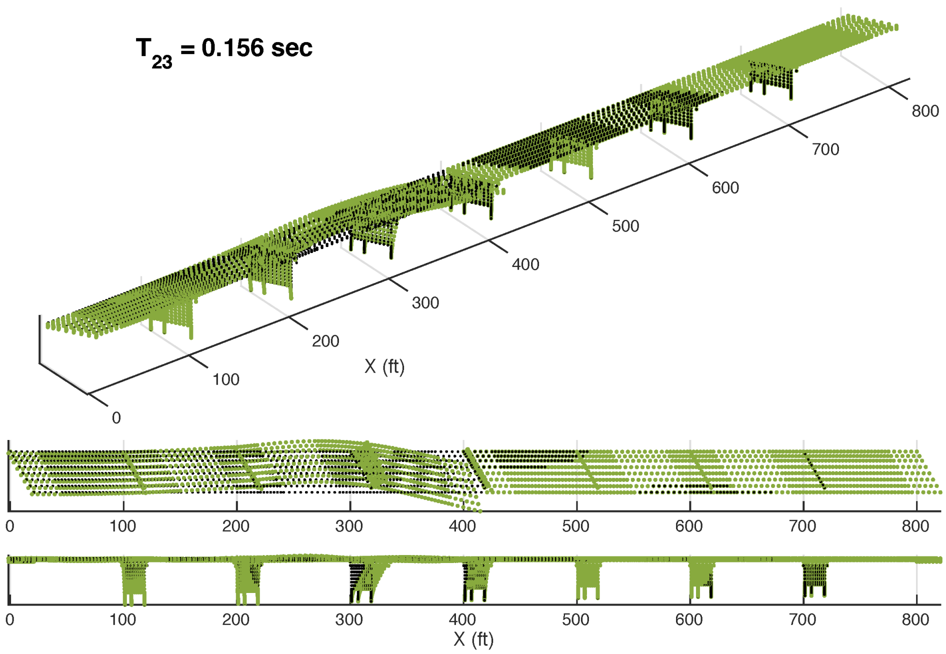

Figure 4.15: 23rd mode of the I-35 bridge over the Cimarron River.

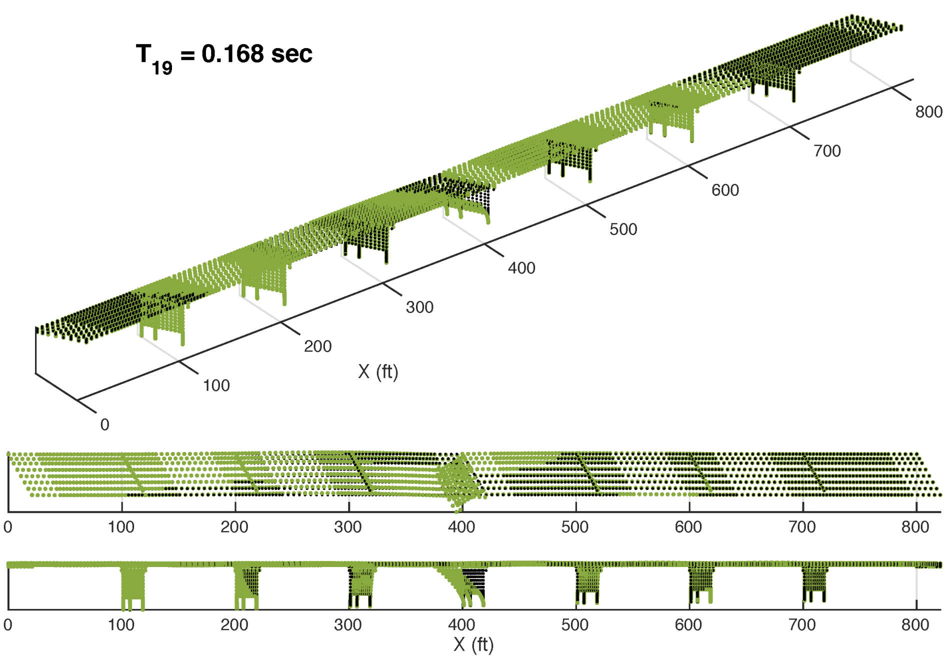

Figure 4.16: 19th mode of the I-35 bridge over the Cimarron River.

tudes and distances for the I-35 bridge over the Cimarron River as part of their Probabilistic Seismic Hazard Analysis (PSHA). The results indicated that the controlling magnitude-distance pairs for this site range from M5.8 to M6.8 with associated distances ranging from 76 to 277 km.

Five earthquake acceleration time histories were selected based on spectral shape, site conditions, moment magnitude, site distance, fault rupture mechanism, and duration of strong shaking (Liao et al., 2016). The strong motion records were chosen from the Pacific Earthquake Engineering Research (PEER) Center database and are listed in Table 4.3.

These GM time histories were spectra matched to target spectra for the site. These target spectra were developed for 7% probability of exceedance (PE) in 75 years and for 2% PE in 50 years. Liao et al. (2016) used these spectrally matched time histories as the outcrop motions in the geotechnical site response analysis. The free field, site-specific horizontal acceleration response spectra and corresponding time-histories for the soil conditions at the site were developed using *SHAKE2000*. The site-specific ground surface (free field) spectra resulting from the site response studies for 7% PE in 75 years and 2% PE in 50 years are shown in Figs. 4.17 and 4.18, respectively. The corresponding ground surface motions are shown in Appendix C.4. Notably, the 1.0-sec spectral acceleration (S_1) for the two hazard levels are approximately 0.047g (7% PE in 75 years) and 0.076g (2% PE in 50 years). These values bound the trigger S_1 value used in the development of the smart bridge inspection radii (0.0556g), permitting an assessment of that trigger value as a predictor for damage for the I-35 bridge over the Cimarron River.

4.5.2 Damage States for Seismic Response Analysis

Past experiences have shown that the vulnerabilities of bridges during earthquakes are mainly due to damage to critical components, such as columns and bearings. For exam-

Table 4.3: Earthquake time histories for seismic analysis.

Earthquake	**Station**	**Component**	**M_w**	**Dist. (km)**	**PGA (g)**
1980 Italy Irpinia Earthquake	Tricarico	TRC000	6.9	53	0.05
1997 Italy Umbria Marche Earthquake	Norcia-Zona Industriale	NZ1090	5.7	29	0.04
1997 Italy Umbria Marche Earthquake	Gubbio-Piana	GBP000	6.0	36	0.09
2009 Italy L'Aquila Earthquake	Celano	TK003XTE	6.3	21	0.08
2009 Italy L'Aquila Earthquake	Sulmona	CR003YLN	6.3	39	0.03

Note: Dist. refers to closest distance to fault rupture.

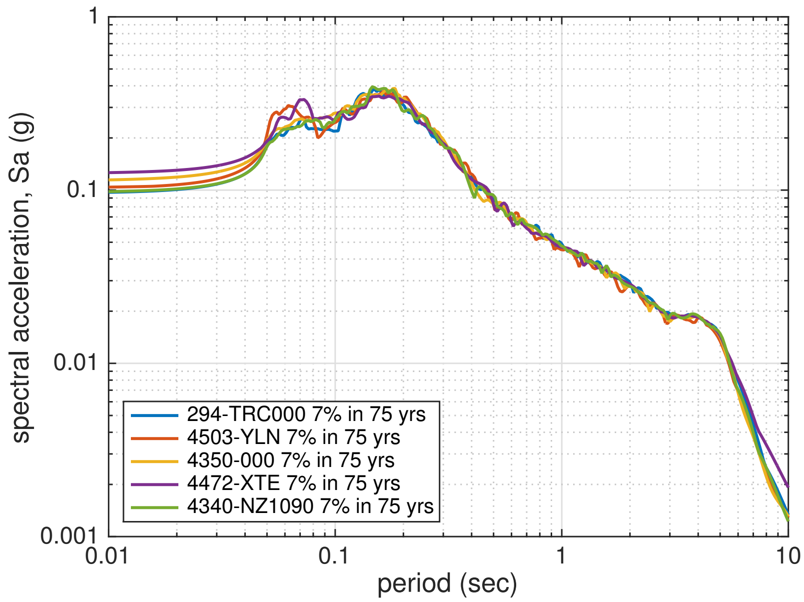

Figure 4.17: Response spectra (5% damped) for the five ground surface motions used in seismic analysis — 7% PE in 75 years.

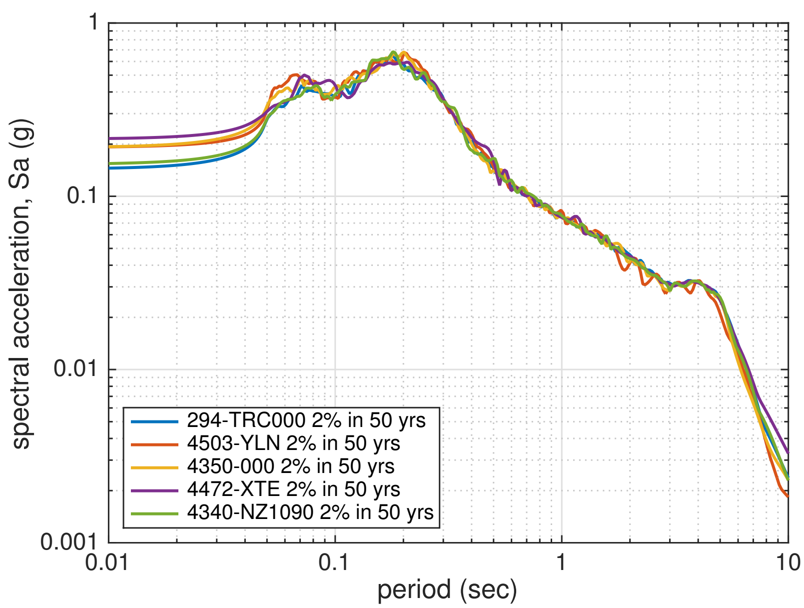

Figure 4.18: Response spectra (5% damped) for the five ground surface motions used in seismic analysis — 2% PE in 50 years.

ple, large relative movements at the expansion joints may result in the loss of support and excessive ductility demands on bridge piers may result in column failure in flexure. Hence, estimating the capacity of bridge components is essential for determining the risk of damage to structural components and the entire structure. With the definition of qualitative damage (limit) states (Table 1.1), the next task is to assign a quantitative measure to each of the limit states for each of the bridge components. Capacity limit states for as-built components from Nielson (2005) are described in this section and will be used when appropriate and modified otherwise.

Flexural Capacity of Concrete Columns

There are different metrics which are available for defining the limit states of the RC columns, including drift, displacement ductility μ_Δ, and curvature ductility μ_ϕ. The metric chosen for this study is curvature ductility which is defined as

$$\mu_\phi = \frac{\phi_{\max}}{\phi_y} \tag{4.4}$$

i.e., the maximum realized curvature divided by the yield curvature or curvature at yield of the outer most steel reinforcing bar.

Nielson (2005) developed limit states using a Bayesian approach, whereby physics-based (“prescriptive”) and survey-based (“descriptive”) information was combined. The prescription approach used values adapted from Hwang et al. (2000). Hwang et al. (2000) proposed limit states, in terms of displacement ductility, of 1.0, 1.2, 1.76, and 4.76 which correspond to yield, cracking, spalling, and reinforcement buckling[†], respectively. These limit states are defined in terms of displacement ductility, so Nielson (2005) translated them into equivalent curvature ductilities for typical RC columns in the Central and Southeastern United States, which are given in Table C.1 (Appendix

[†]The *Seismic Retrofitting Manual for Highway Bridges* (FHWA, 1995b) notes that, for poorly confined columns, longitudinal steel will buckle at a displacement ductility of 3.0, which is thus the value chosen by Nielson (2005).

C.5). The descriptive approach used survey data from Padgett and DesRoches (2007) where bridge inspectors and officials were asked to describe the functionality of a bridge for different levels of component damage. Following a Bayesian updating procedure, the limit states for the columns were modified, resulting in the limit states listed in Table C.2. In this study, the prescriptive values for the column limit states are used, which are, in general, slightly conservative and are given in Table 4.4.

Deformation Capacity of Bridge Bearings

Nielson (2005) used the same Bayesian approach to define the limit states for bearings. The following presents the prescriptive limit states (Table C.1) and the Bayesian updated limit states (Table C.2), as well as the limit states used in this study (Table 4.4).

High-Type Steel Bearings For the prescriptive limit state of high-type steel (fixed) bearings, Nielson (2005) assumed a deformation of 0.24 in. for slight damage, 0.79 in. for moderate damage, 1.57 in. for extensive damage, and 10.0 in. for complete damage in both the longitudinal and transverse directions. These values correspond to appearance of cracks in the concrete pier, prying of bearings and severe deformation in the anchor bolts, complete fracture of bolts resulting in toppling or sliding of the bearings,

Table 4.4: Limit states for bridge components used in this study. Adapted from Nielson (2005).

Component		Slight	Moderate	Extensive	Complete
RC column (μ_ϕ)		1.00	1.58	3.22	6.84
High-Type Steel Bearing					
	longitudinal (in.)	0.24	0.79	1.57	7.35
	transverse (in.)	0.24	0.79	1.57	7.35
Roller Bearing					
	longitudinal (in.)	1.47	4.10	5.36	7.35
	transverse (in.)	0.24	0.79	1.57	7.35
Expansion-type Elastomeric Bearing					
	longitudinal (in.)	1.92	4.10	5.36	7.35
	transverse (in.)	0.24	3.58	5.60	7.68

and unseating of the girder resulting in the complete collapse of the span, respectively.

Following the Bayesian update procedure, the limit states for the high-type steel bearings were modified. The median values for the updated limited states are presented in Table C.2, which were used in this study (Table 4.4).

Roller Bearings Nielson (2005) did not consider roller bearings. However, the transverse deformations for all damage states were assumed to be the values Nielson (2005) used for the high-type steel bearings, to be consistent with the assumptions in Section 4.3.2. The longitudinal values for high-type steel rocker bearings and the values for low-type steel sliding bearings were the same. These bearings are both types of steel expansion bearings, so we assumed that roller bearings would have similar limit states in the longitudinal direction.

Examining the plans for the roller bearing shows that the slot for the keeper bar and the keeper bar may have a 2:12 slope. This would mean that if the bearing rolled approximately 18.4 degrees, the keeper bar would engage the side of the slot. Because the roller is 6⅜ in. in diameter, the deflection from this rotation would be about 2.02 in. This is greater than the value presented in Table 4.4 for slight damage, so the assumptions for deflections in the longitudinal direction for the roller seem valid.

Elastomeric Bearings The behavior of the elastomeric bearings is one which is controlled by shearing, but at large deformations, sliding is initiated. Unrestricted sliding can only occur once a fracture of the steel retention dowels (anchor bolts) occurs. For the prescriptive information, Nielson (2005) assumed a deformation of 1.18 in. for slight damage, 3.94 in. for moderate damage, 5.91 in. for extensive damage, and 10.0 in. for complete damage. These values correspond to noticeable deformation without significant closure, need for realignment with possible dowel fracture, need for some degree of repair (girder retention) with assured dowel fracture and additional deck realignment, and unseating of girder, respectively. These values were then updated using survey data

(Table C.2).

The slot dimensions for the expansion elastomeric bearings detailed by Nielson (2005) differ from those on the I-35 bridge over the Cimarron River. On the I-35 bridge over the Cimarron River, the slot allows for ±1.875 in. of deflection longitudinally and ±0.1875 in. of deflection transversely. According to the anchor bolt model, yielding and failure of the bolt will occur, respectively, at 0.05 in. and 0.10 in. beyond engagement of the slot. Therefore, the values for slight damage determined by Nielson (2005) have been modified to be better representative of the I-35 bridge over the Cimarron River. These limit state values are given in Table 4.4.

Note that Nielson (2005) considered dowels encased in the elastomeric pads, for which "it is difficult, if not impossible, for a bridge inspector to recognize this fracture or to differentiate between the fixed and expansion bearings." Therefore, Nielson (2005) assumed that the limit states for the fixed and expansion elastomeric bearings, in both the longitudinal and transverse directions, are the same. This is not the case for the bearings used on the I-35 bridge over the Cimarron River, as reflected in Table 4.4.

4.5.3 Seismic Evaluation of Bridge Components

Seismic Evaluation of Concrete Columns

Fig. 4.19 shows the maximum column curvatures due to longitudinal GMs. The variables ϕ_X and ϕ_Z are the transverse and the longitudinal curvatures of the pier columns, respectively. The maximum curvatures occurs at the columns with fixed bearings (piers 2 and 6) and the lower curvatures occur at columns with expansion bearings (all other piers). This is because, if the bearing does not readily deform (i.e., fixed-type), the lateral inertial loads will be transmitted to the columns producing larger bending moments. The columns with elastomeric bearings show more curvature than the columns with roller bearings as the elastomeric bearings are stiffer. The longitudinal loading

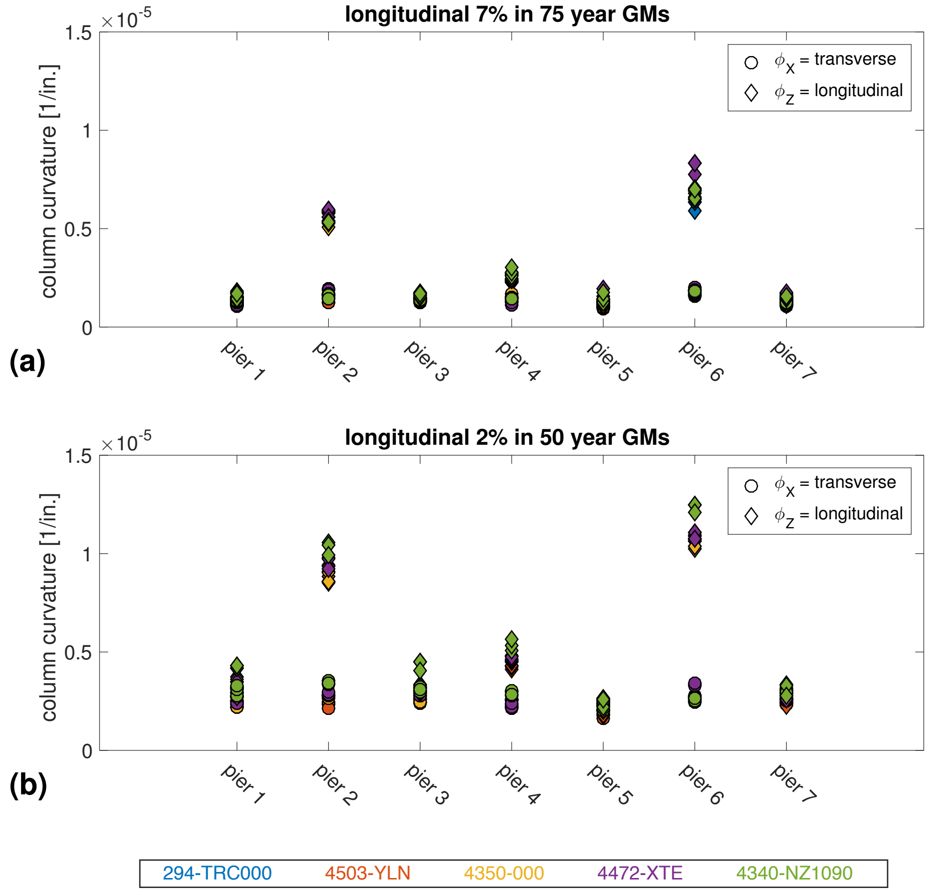

Figure 4.19: Maximum column curvatures for longitudinal GMs: (a) 7% PE in 75 years and (b) 2% PE in 50 years. Marker shape indicates deflection direction; fill color indicates the GM considered.

causes higher longitudinal curvatures in all piers. Similar trends are seen for the 7% PE in 75 year GMs (Fig. 4.19(a)) and the 2% PE in 50 year GMs (Fig. 4.19(b)), but the 2% PE in 50 year GMs produce larger curvatures.

Fig. 4.20 shows the maximum column curvatures due to transverse GMs. Piers 1 and 7 exhibit the largest curvatures.The other five piers (2 through 6) exhibit comparable maximum curvatures. The figure shows that transverse loading causes more curvature in the longitudinal than in the transverse direction in every pier except two and six. This is because the bents are stiffer transversely than they are longitudinally. Note that the weakest direction is perpendicular to the bent beam due to the skew angle. Similar

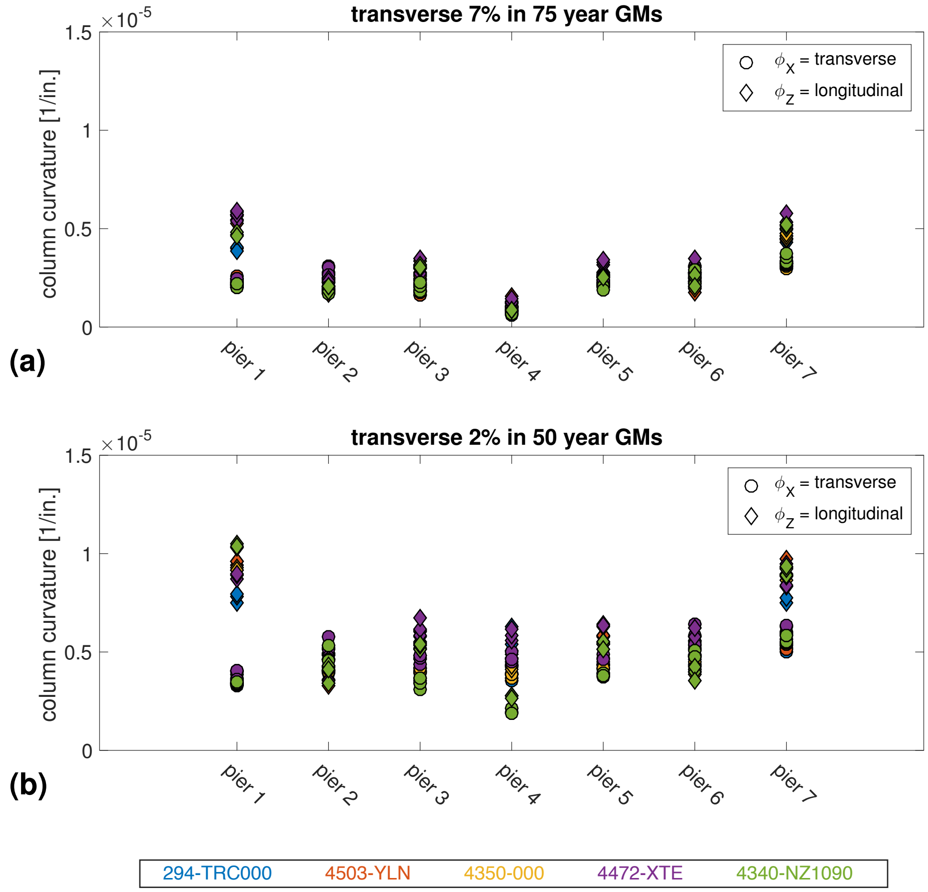

Figure 4.20: Maximum column curvatures for transverse GMs (a) 7% PE in 75 years and (b) 2% PE in 50 years. Marker shape indicates deflection direction; fill color indicates the GM considered.

trends are seen for the 7% PE in 75 year GMs (Fig. 4.20(a)) and the 2% PE in 50 year GMs (Fig. 4.20(b)), but the 2% PE in 50 year GMs produce larger curvatures.

Figs. 4.19 and 4.20 show that the maximum column curvatures in the longitudinal and transverse directions are 6.425×10^{-6} and 1.247×10^{-5} 1/in., respectively. In both cases, the curvatures are well below the yield values (5.25×10^{-5} 1/in.). The maximum longitudinal curvature occurred due to longitudinal loading and the maximum transverse curvature occurred due to longitudinal loading, as well.

Fig. 4.21 compares the moment-curvature plots for the column with the maximum curvature in the transverse and longitudinal directions, pier 6 column 2, to the moment-

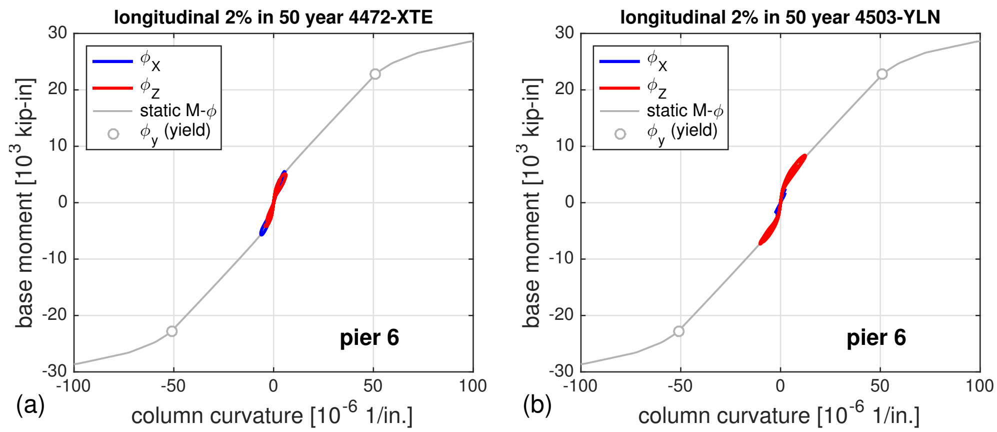

Figure 4.21: Moment-curvature responses for columns. (a) Pier 6, middle column for 4472-XTE at 2% PE in 50 years in the transverse direction; (b) Pier 6, middle column for 4503-YLN at 2% PE in 50 years in the longitudinal direction.

curvature relationship for the column's capacity. The dynamic moment-curvature plots for the columns follow the static moment-curvature relationship of the column very closely. The curvature ϕ_y at the first yielding is also shown on the figure, and it can be seen that the column curvature is well below its maximum curvature — a curvature ductility (μ_ϕ) value of about 25%.

Seismic Evaluation of Bridge Bearings

Fig. 4.22 shows the maximum bearing deflections at each pier due to longitudinal GMs. Each figure has points for five different earthquakes, eight bearings per pier, and two directions of motion (longitudinal and transverse), or 80 points, with the exception of the fourth pier which has sixteen bearings and 160 points. Maximum deflections are lowest at the fixed-type bearings (piers 2 and 6), as expected. This figure is almost the opposite of the curvature plots where the maximum curvatures occurred at the columns with fixed bearings and the lower curvatures occurred at columns with expansion bearings. Both of the abutments and piers one, three, five, and seven employ roller bearings. The maximum deflections for roller bearings occur at the abutments because they are furthest from the fixed bearings. The deflections in the elastomeric bearings are similar

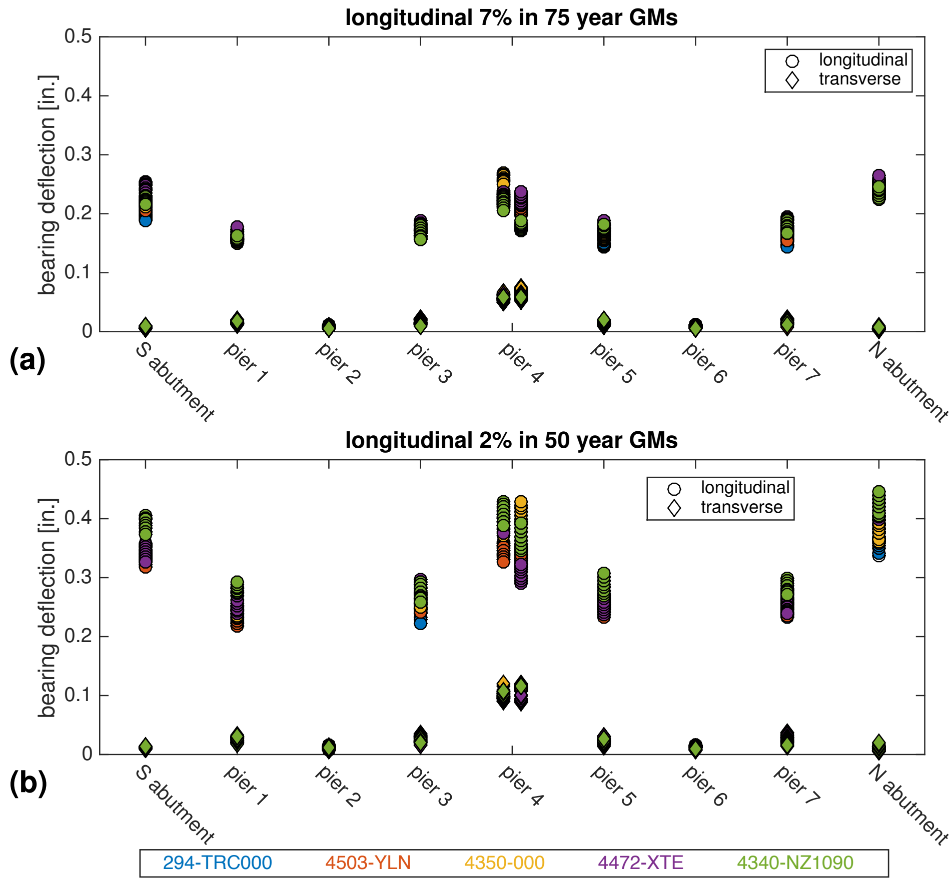

Figure 4.22: Maximum bearing deflections for longitudinal GMs: (a) 7% PE in 75 years and (b) 2% PE in 50 years. Marker shape indicates deflection direction; fill color indicates the GM considered.

to but slightly less than deflections in the abutments. Similar trends are seen for the 7% PE in 75 year GMs (Fig. 4.22(a)) and the 2% PE in 50 year GMs (Fig. 4.22(b)), but the 2% PE in 50 year GMs produce larger deflections. Also, it can be seen that the longitudinal displacements tend to be greater than the transverse displacements for longitudinal loadings.

Fig. 4.23 shows the maximum bearing deflections at each pier due to transverse GMs. The points are for the same locations and motions as stated for Fig. 4.22. Like Fig. 4.22, maximum deflections are lowest at the fixed-type bearings (piers 2 and 6). However, the maximum deflection for rollers occurred at piers one and seven instead of the abutments. The deflections at pier four for the elastomeric bearings were the second

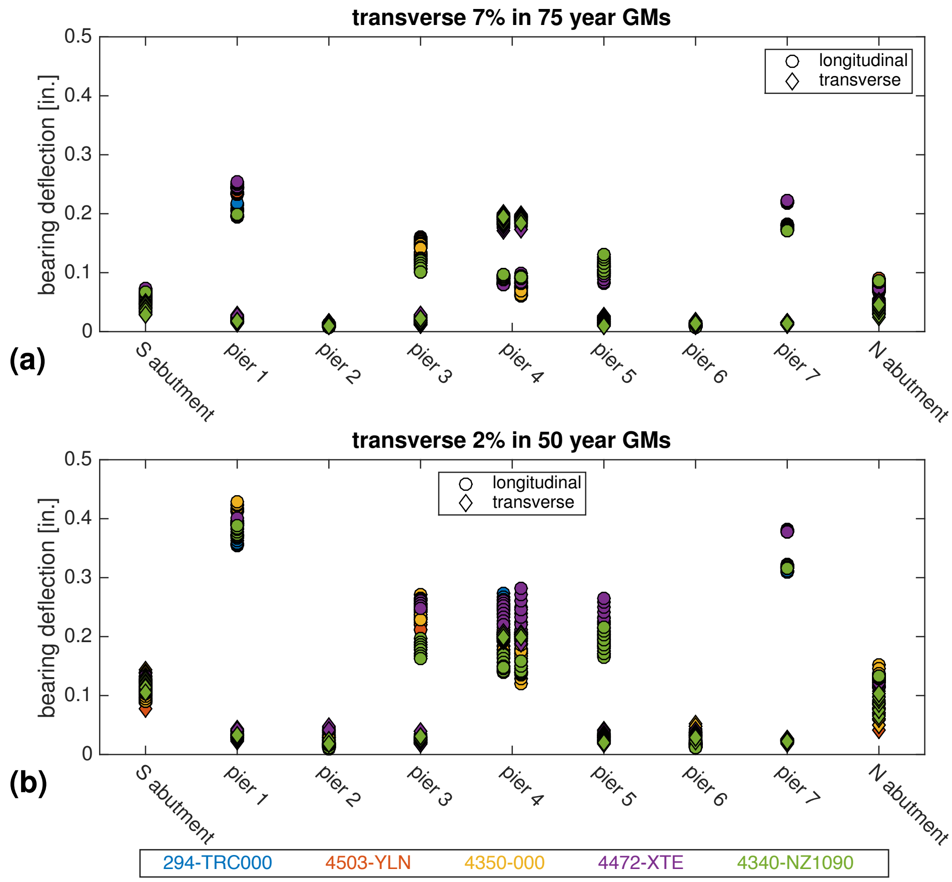

Figure 4.23: Maximum bearing deflections for transverse GMs (a) 7% PE in 75 years and (b) 2% PE in 50 years. Marker shape indicates deflection direction; fill color indicates the GM considered.

greatest deflections. Similar trends are seen for the 7% PE in 75 year GMs (Fig. 4.23(a)) and the 2% PE in 50 year GMs (Fig. 4.23(b)), but the 2% PE in 50 year GMs produce larger deflections. The shape, however, is different from that of Fig. 4.22. This may be because of the skew angle.

Figs. 4.24–4.26 show force-deflection responses for the maximum deflections in the transverse and longitudinal directions for the three bearing types: high-type steel, roller, and elastomeric.

Fig. 4.24 shows that the maximum displacement in the longitudinal direction for a high-type steel bearing is 0.02 in. and the maximum displacement in the transverse direction is 0.05 in. Both of these values are significantly lower than the deflection for

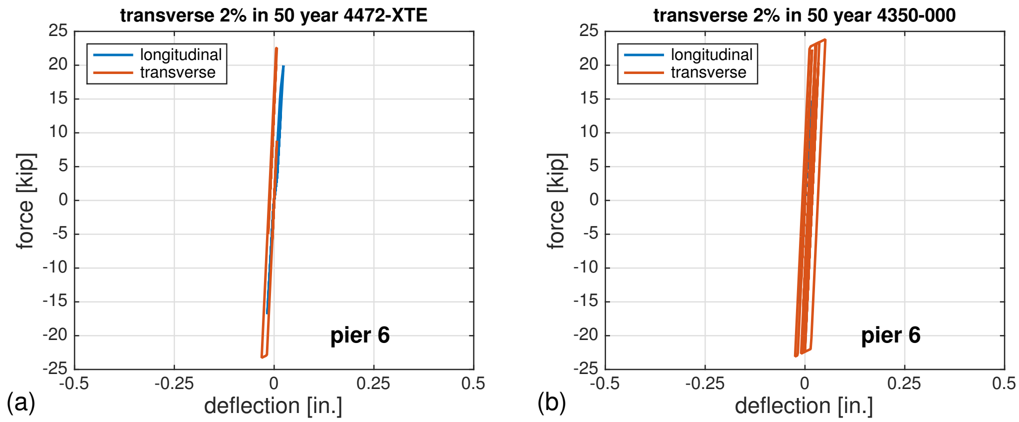

Figure 4.24: Force-deflection responses for high-type fixed bearing. (a) Pier 6, bearing #1 for 4472-XTE at 2% PE in 50 years applied in the transverse direction; (b) Pier 6, bearing #7 for 4350-000 at 2% PE in 50 years applied in the transverse direction.

slight damage presented in Table 4.4. These values are similar in magnitude because the bearing is not designed to allow deflection in either the longitudinal or transverse directions. Unlike the roller and elastomeric bearings, both of the maximum displacements were caused by transverse loadings. These bearings experience larger deflections because they carry larger loads. When we load the bridge transversely, the piers are much stiffer and cannot accommodate the same levels of drift. Therefore, the inertial loads transmitted to the bearings are greater.

The maximum displacement in the longitudinal direction for a roller bearing is 0.47 in. while the maximum displacement in the transverse direction is 0.14 in. (Fig. 4.25). Both of these values are lower than the deflection for slight damage presented in Table 4.4. This makes sense because the roller is designed to deflect in the longitudinal direction and is much more resistant to deflection in the transverse direction. Additionally, the maximum longitudinal displacement is due to a longitudinal loading and the maximum transverse displacement is due to a transverse loading.

Fig. 4.26 shows that the maximum displacement in the longitudinal direction for an elastomeric bearing is 0.43 in. and the maximum displacement in the transverse direction is 0.21 in. Both of these values are significantly lower than the deflection for

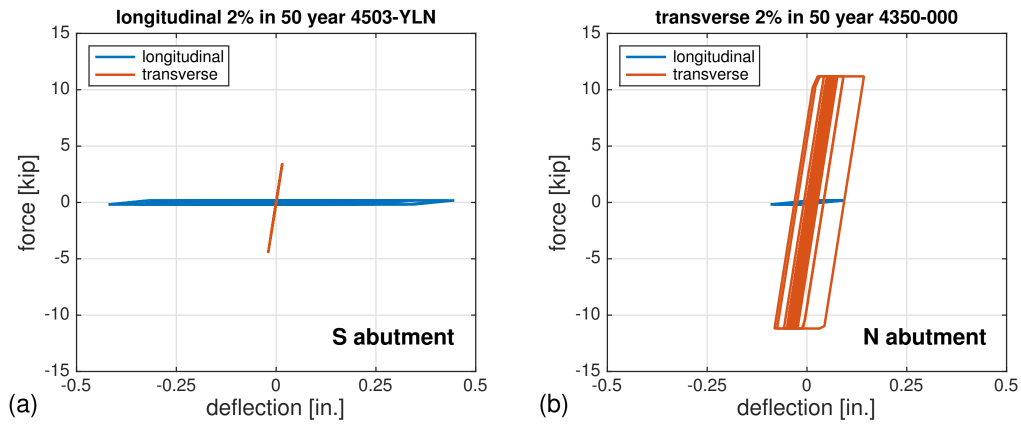

Figure 4.25: Force-deflection responses for roller bearing. (a) South abutment, bearing #8 for 4503-YLN at 2% PE in 50 years applied in the longitudinal direction; (b) North abutment, bearing #2 for 4350-000 at 2% PE in 50 years applied in the transverse direction.

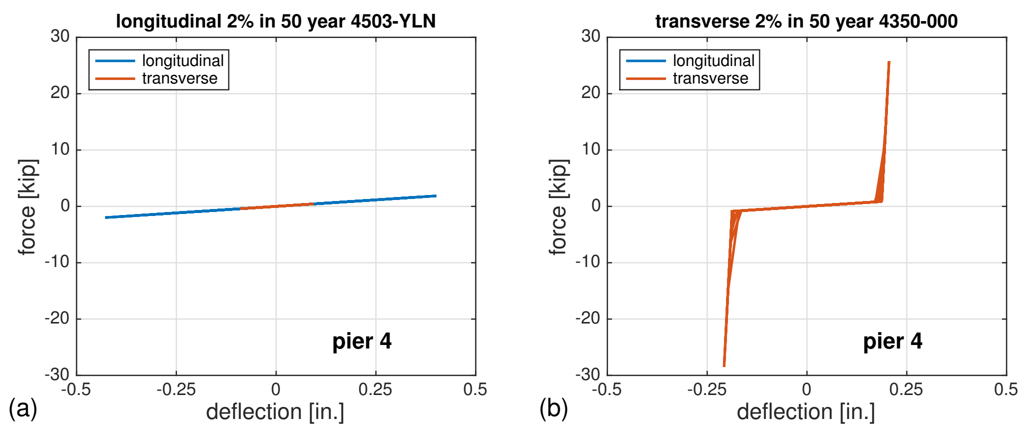

Figure 4.26: Force-deflection responses for elastomeric bearing. (a) Pier 6, bearing #1 for 4503-YLN at 2% PE in 50 years applied in the longitudinal direction; (b) Pier 4, bearing #7 for 4350-000 at 2% PE in 50 years applied in the transverse direction.

slight damage presented in Table 4.4. These values are more similar to one another than the roller displacement values because the elastomeric pad allows displacement in both the transverse and longitudinal directions. In the longitudinal direction, the force-displacement response (Fig. 4.26(a)) is linear which indicates that the bolts were not activated due to the displacement: all motion was in the bolt slot of the bearing. In the transverse direction (Fig. 4.26(b)), the center portion of the figure shows motion within the bolt slot; however, the gap is smaller transversely than in the longitudinal direction, so the bolt is activated and the stiffness increases which cause a stiffening effect beyond about 0.20 in. of transverse deflection. Similar to the roller bearings, the maximum longitudinal displacement is caused by a longitudinal loading and the maximum transverse displacement is caused by a transverse loading.

4.6 Summary

In this chapter, an *OpenSees* finite element model of the I-35 bridge over the Cimarron River, located approximately 40 miles north of Oklahoma City in Logan County, Oklahoma, was developed and used to conduct a seismic response analysis. The seismic response analysis has shown that the potential for structural damage is low under both the 7% PE in 75 years and 2% PE in 50 years level events considered. The analysis indicates that the maximum curvature in the columns was about 25% of the yield curvature and the maximum deflections in the bearings were less than 0.5 in. The maximum column curvatures and the bearing deflections were below the values prescribed for the slight damage state in the bridge fragility curves. This helps verify the HAZUS fragility curves used for the development of ShakeCast–OK (Chapter 5). The maximum 1.0-sec spectral acceleration (S_1) used in these seismic analyses, 0.076g, is higher than the trigger value of 0.0556g used in the development of the smart bridge inspection radii (Chapter 2). Therefore, the value of 0.0556g can be considered a conservative value for this bridge for inspection purposes.

Chapter 5

ShakeCast-OK

5.1 Overview

Chapter 2 described the creation of smart radii for ODOT. This chapter takes the trigger value established for the development of the smart radii and uses it as a starting point for ShakeCast-OK, a further refinement of the inspection protocol. ShakeCast (short for ShakeMap Broadcast) is a situational awareness application that automatically retrieves a ShakeMap from USGS, compares shaking intensities against users' facilities' fragility curves, and sends email notifications of potential damage levels to responsible parties (Wald et al., 2008). ShakeCast has the benefit of using real time data to offer better ground motion estimates than using an attenuation model alone. This will help overcome the limitations of current attenuation models demonstrated in Chapter 3.

This chapter details the development and implementation of ShakeCast for ODOT, termed ShakeCast-OK. To create a ShakeCast instance, the recommended practices found in the *Cloud Installation Guide* were followed (USGS, 2015a). Then, modifications of the standard fragility curves were made to better match Oklahoma's inventory, and these modified fragilities were used to populate the instance. Finally, the savings afforded by ShakeCast in terms of department of transportation resources are quantified through a few scenarios, in which ShakeCast is compared with the previous ODOT inspection radii and the smart radii.

5.2 Fragility Curve Modifications

When calculating the fragility curves for ODOT's bridges, the standard HAZUS fragility curves were not appropriate in all cases. As previously mentioned in Chapter 2, the slight fragility curve cannot be calculated prior to an earthquake. Because ShakeCast bridge inventories are uploaded prior to an earthquake, a trigger value is used instead. The same trigger value as previously described in Chapter 2 (i.e., a spectral acceleration at 1.0 second of 0.0556g) was used for every bridge in the inventory.

Another concern with the standard HAZUS fragility curves was that they do not take into account a bridge's actual condition at the present time. To account for this and be more conservative, two additional bridge properties were examined: (i) whether or not a bridge was fracture critical and (ii) whether or not a bridge's super- and substructure were structurally deficient. The former is indicative of a bridge having at least one tension member whose failure will most likely cause a part of or the entire bridge to collapse and is identified by NBI item number 92A (FHWA, 1995a). The latter are identified by NBI item numbers 59 and 60, and for this study an NBI rating of four or less in either category was deemed structurally deficient. For fracture critical and structurally deficient bridges, the moderate, extensive, and complete fragility curves' medians were reduced to the S_1 value corresponding to a 25% probability of damage from the HAZUS fragility curve. The purpose of this was to reduce the threshold values for these damage states so the threshold would be exceeded for lower levels of shaking.

There are certain bridge classes that are not represented in HAZUS, e.g. masonry bridges and bridges with a variable skew angle. Therefore, to be conservative, the moderate, extensive, and complete fragility curves for these bridges were assigned to be the lowest fragility curves found in the ODOT database: median S_1 values of 15, 20, and 25%g, respectively.

5.3 Populating the ShakeCast Database

In order to use a ShakeCast instance, files must be uploaded with information about bridges and who should receive notifications about these bridges. Additionally, the order which the files are uploaded to ShakeCast is critical since notifications will not be sent if they are uploaded in the incorrect order.

5.3.1 Facility Inventory

Bridge information is uploaded to ShakeCast by using a CSV file. This file contains several different fields of information including identifiers, descriptions, and fragility values. The following facility fields were populated.

external_facility_id This field identifies the facility, which was determined to include each bridge's structure number (ODOT's name to identify a bridge) and the first five digits of its NBI number, e.g., '4230 1874EX / 14517'. The bridge's structure number was included because it is ODOT's preferred way of identifying its bridges because it provides information about the location of the bridge. The NBI number was provided as an additional way to identify the bridge.

facility_type This field identifies the type of facility. ShakeCast's default facility type for bridges is $BRIDGE\_ST$. However, using this for all of ODOT's bridges did not achieve the desired result. ODOT desired the notifications to be packaged by division so that the division engineers would not have to sort through a list of bridges to determine if their division was affected. Instead, new facility types, $DIV1$, $DIV2$, etc., were created for each of ODOT's divisions. By creating a facility type for each division, this will allow the engineers to easily determine the number of bridges affected per division.

facility_name This field was used to give additional identification information concerning each bridge. This field was populated with both the facility carried (NBI item number 7) and the feature intersected (NBI item number 6), e.g., ‘I-35 / CIMARRON RIVER’.

description This field is used to give a short description of the bridge. It is not included in the email notification or the ShakeCast Summary Report. The additional information included here was the bridge’s division, “Fracture Critical” for fracture critical bridges, “Structurally Deficient” for structurally deficient bridges, and the bridge’s skew angle. This information was included so that inspectors would know factors for each bridge that might cause it to need to be prioritized.

lat, lon These fields specify the bridge’s latitude and longitude.

METRIC:PSA10:*damage-level* Each field beginning with `METRIC:` is the facility fragility specifier. The ShakeMap metric used is `PSA10` (1.0-sec spectral acceleration), and the *damage-level* is taken to be `GREEN`, `YELLOW`, `ORANGE`, and `RED` for the low, medium, medium-high, and high potential impact fragility values, respectively.

short_name This field is supposed to be a shorter version of the facility name used in the output, but the default templates used this field as the ‘Location’ in the email notification. Therefore, this field was populated with the latitude and longitude of the bridge (e.g., ‘35.9847, 97.353’).

The first file that must be uploaded to ShakeCast is an XML file generated by the ShakeCast Workbook (Q.-W. Lin, personal communication, October 2016) that defines the facility types. This is required because new facility types (e.g., DIV1, DIV2, etc.) needed to be created in the system. Additionally, icons for each division and for their five possible damage states (none, slight, moderate, extensive, and complete) must be uploaded so that bridge icons will show on the ShakeCast reports and online. After uploading the facility types, the bridge CSV file can be uploaded.

Once the bridges have been uploaded, they can be viewed under the Facilities tab, as shown in Fig. 5.1. Clicking on one of the bridges shown on this page displays infor-

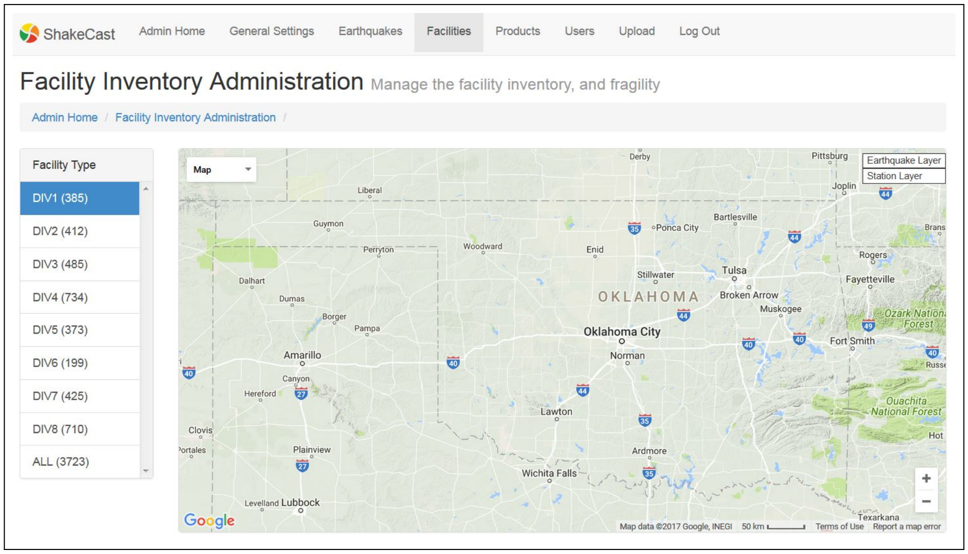

Figure 5.1: A screenshot from ShakeCast showing uploaded facilities.

mation about the bridge as well as its location (Fig. 5.2).

5.3.2 User Groups

After uploading the bridges, an XML file defining the groups is uploaded. The XML file is generated by the ShakeCast Workbook (Q.-W. Lin, personal communication, October 2016). For this project, eight groups were created, DIV1, DIV2, DIV3, etc. A group defines which facility types a person assigned to the group will receive notifications for. In this case, each ODOT division has its own group. The group file also includes a predetermined area inside of which earthquakes will be processed. The area for all divisions was defined as a polygon fully encompassing Oklahoma as well as portions of the surrounding states. The administrator can set the minimum magnitude that notifications will be sent out for. A magnitude of 4.0 was chosen. This file also lets the administrator choose which notifications will be sent out. For this instance, notifications were selected for each of the damage states. This means that a notification will be sent out when there is a new event if any bridges have shaking above the trigger value.

Once the groups have been uploaded, they can be viewed under the Users tab.

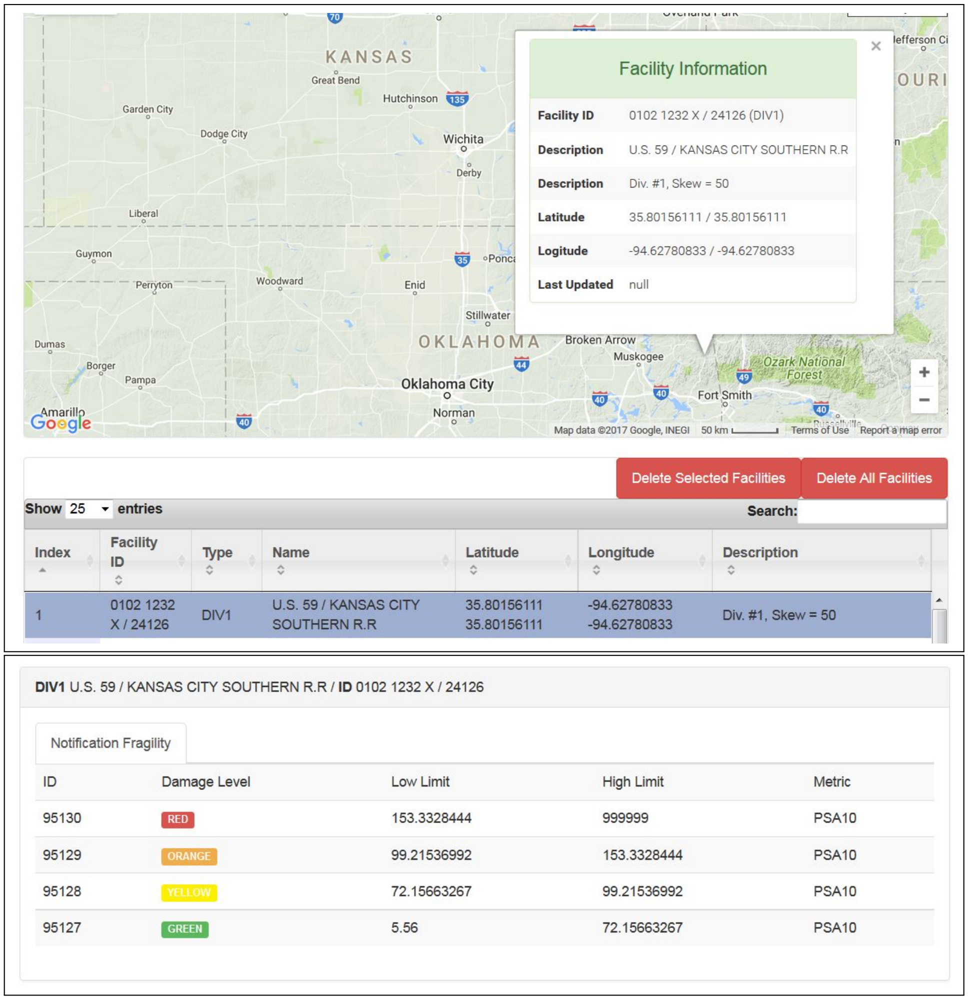

Figure 5.2: A screenshot from ShakeCast showing bridge information.

Fig. 5.3 is a screenshot showing the groups as well as the polygon used for all divisions. Tabs not shown in the screenshot display more information about each group.

5.3.3 User Inventory

The final file to be uploaded is a CSV file that defines the ShakeCast users, or those who will receive ShakeCast emails. There were two iterations of this file for this project: one which included all relevant ODOT personnel and one which sends an email to an ODOT email group which ODOT maintains to send to its relevant personnel.

The CSV file contains nine columns: `USER_TYPE`, `USERNAME`, `PASSWORD`,

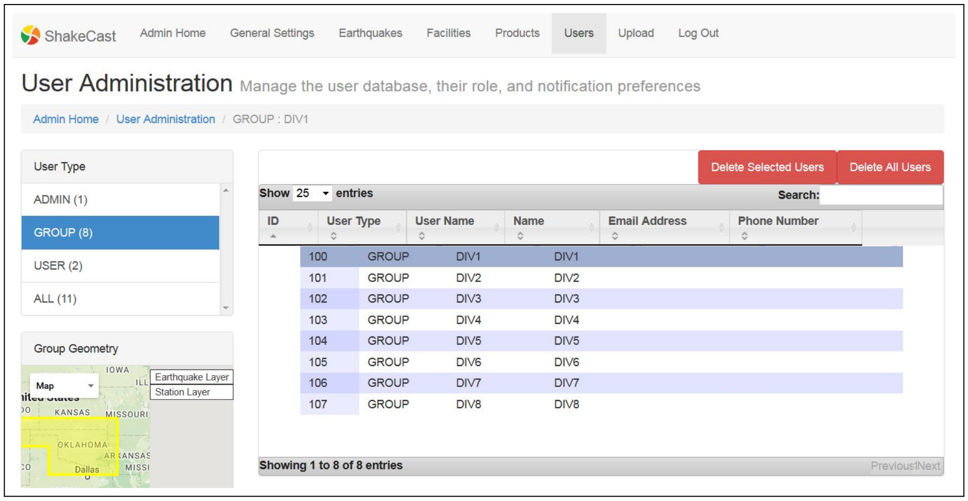

Figure 5.3: A screenshot from ShakeCast showing uploaded groups.

`FULL_NAME`, `EMAIL_ADDRESS`, `PHONE_NUMBER`, `GROUP`, `DELIVERY:PAGER`, and `DELIVERY:EMAIL_HTML`. The user type for all users is defined as $USER$. A user profile cannot upload and change files like an administration profile can. Each username must be unique, so each user's username was taken to be their ODOT email address without '@odot.org'. The email and two delivery columns all used the same email address. For the group column, each user was assigned to all of the divisions. This means that after an earthquake, every person will receive one email per division with affected bridges.

5.4 Running ShakeCast Scenarios

To test ShakeCast and ensure that it is working properly, earthquake scenarios were run. The scenarios used were from previous Oklahoma earthquakes. Only two of the earthquakes Oklahoma has experienced to date (24 April 2017) had shaking levels high enough to trigger email notifications: the M5.7 earthquake on 6 November 2011, and the M5.8 earthquake on 3 September 2016.

To load an earthquake, one goes to the Administration tab and then the Earthquakes tab. Under the Earthquakes tab, there are two ways to fetch earthquakes: fetching from scenarios or fetching from archives (Fig. 5.4). If one chooses to fetch a scenario, the let-

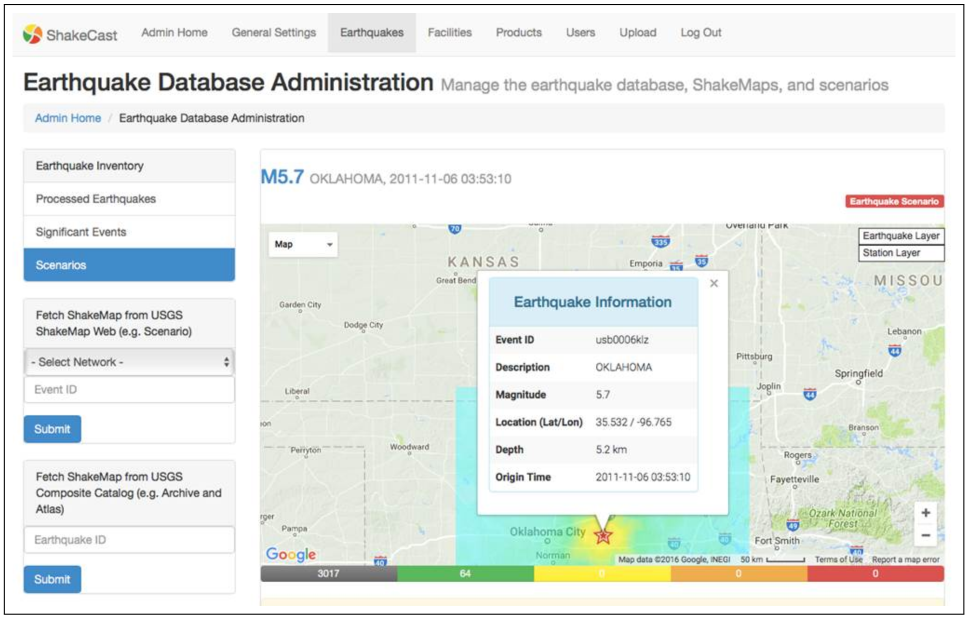

Figure 5.4: A screenshot from ShakeCast showing an earthquake.

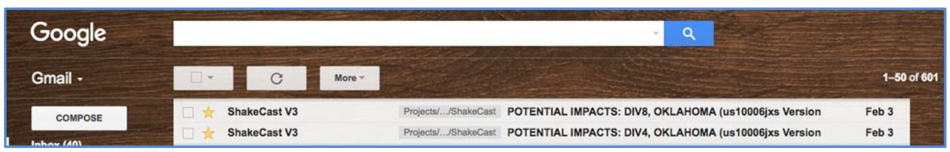

Figure 5.5: A screenshot of ShakeCast emails for the M5.8 earthquake.

ters "us" prior to the earthquake ShakeMap number are not included (e.g. b0006klz and 10006jxs). If one fetches an event from archives, the "us" is included (e.g. usb0006klz and us10006jxs). Once a scenario has been loaded, it must be deleted before it can be loaded and run again. If "trigger" is selected on an event that has already been loaded, it will delete the event from the ShakeCast Instance and it cannot be retrieved again. Additionally, after an earthquake has been deleted once, it can only be re-retrieved from the scenarios bar.

After a scenario has been triggered, one email is received per division affected (Fig. 5.5). Each email has two parts: the body and an attached PDF. The body of the email includes a ShakeMap of the earthquake and a list of all affected bridges in the division (Figs. 5.6 and 5.7). The PDF includes a map with the affected bridge locations

POTENTIAL IMPACTS: DIV4, OKLAHOMA (us10006jxs Version 9)

ShakeCast V3 <shakecast@usgs.gov> Mon, Feb 13, 2017 at 10:00 AM
To: ShakeCast V3 <shakecast@usgs.gov>

USGS science for a changing world — **ShakeCast Report** — National Earthquake Information Center (NEIC)

Potential Impacts: DIV4

This report supersedes any earlier reports about this event. This is a computer-generated message and has not yet been reviewed by an Engineer or Seismologist. Epicenter and magnitude are published by the USGS. Reported magnitude may be revised and will not be reported through ShakeCast. The USGS website should be referenced for the most up-to-date information. Inspection prioritization emails will be sent shortly if ShakeCast determines significant shaking occurred at user's infrastructure. An interactive version of this report is accessible on the ShakeCast internet/intranet website.

Earthquake Details

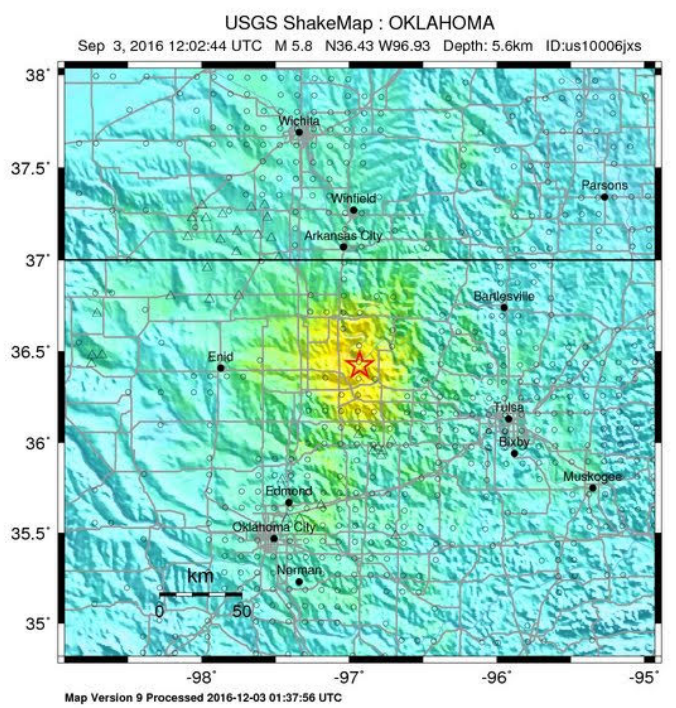

PERCEIVED SHAKING	Not felt	Weak	Light	Moderate	Strong	Very strong	Severe	Violent	Extreme
POTENTIAL DAMAGE	none	none	none	Very light	Light	Moderate	Mod./Heavy	Heavy	Very Heavy
PEAK ACC.(%g)	<0.007	0.08	1.0	5.0	8.8	15	27	47	>83
PEAK VEL.(cm/s)	<0.003	0.04	0.5	3.0	6.5	14	30	63	>136
INSTRUMENTAL INTENSITY	I	II-III	IV	V	VI	VII	VIII	IX	X+

Scale based upon Atkinson & Kaka, 2007

Name: **(not assigned at this time)** Magnitude: **5.8** ShakeMap ID: **us10006jxs-9** Location: **OKLAHOMA** Latitude-Longitude: **36.4251, -96.9291** Local Time: **2016-09-03 12:02:44**

Figure 5.6: Example ShakeCast email body.

Summary of Potential Impacts: DIV4

Total number of facilities analyzed: **32**
Summary by impact rank:

High	**0**	High impact potential
Medium-High	**0**	Medium-High impact potential
Medium	**0**	Medium impact potential
Low	**32**	Low impact potential
Below Threshold	**0**	No impact potential

List of Potentially Impacted Facilities: DIV4

DIV4 presented in the table below are sorted in order of impact potential. The list includes the top 200 facilities in the area of shaking. The complete list is available on the web server.

DIV4	Facility ID	Location	Impact Potential	PSA10
U.S. 177 / CIMARRON TP GATE UNDER	5238 1470 X / 19078	36.3833, 97.0678	Low	13.04
U.S. 177 / BNSF R.R. UNDER	5224 1150 X / 19350	36.4572, 97.0678	Low	12.27
U.S. 64 / LONG BRANCH CREEK	5204 1619 X / 21610	36.2965, 96.9952	Low	12.75
S.H. 108 / CIMARRON TP UNDER	6034 0210 X / 19063	36.2374, 96.9258	Low	11.19
U.S. 64 / OAK CREEK	5204 1904 X / 21540	36.3065, 96.9457	Low	9.74
U.S. 177 / LONG BRANCH CREEK	6031 0920 X / 22013	36.2349, 97.0699	Low	9.09
U.S. 177 / BLACK BEAR CREEK	5224 0223 X / 28201	36.3227, 97.0676	Low	13.26
U.S. 177 / BLACK BEAR CREEK N O'FLO	5224 0241 X / 28202	36.3252, 97.0676	Low	13.26
U.S. 177 / BLACK BEAR CREEK S O'FLO	5224 0201 X / 28200	36.3192, 97.0676	Low	13.26

Figure 5.7: Example ShakeCast email body (cont.).

from all divisions and a list of these bridges (Fig. 5.8). This list included more detailed information about the bridges than in the email body. The information from these emails can be copied and pasted into Excel to be sorted such that division engineers can best organize a route to inspect bridges.

5.5 ShakeCast and Radii Comparison

By implementing ShakeCast, ODOT will be able to save money by reducing the number of bridges inspected. Fig. 5.9 shows the number of bridges inspected using the old radii, the interim protocol (smart radii), and ShakeCast for the M5.7 and M5.8 earthquakes. The average cost to inspect a bridge is $55 (W. L. Peters, personal communication,

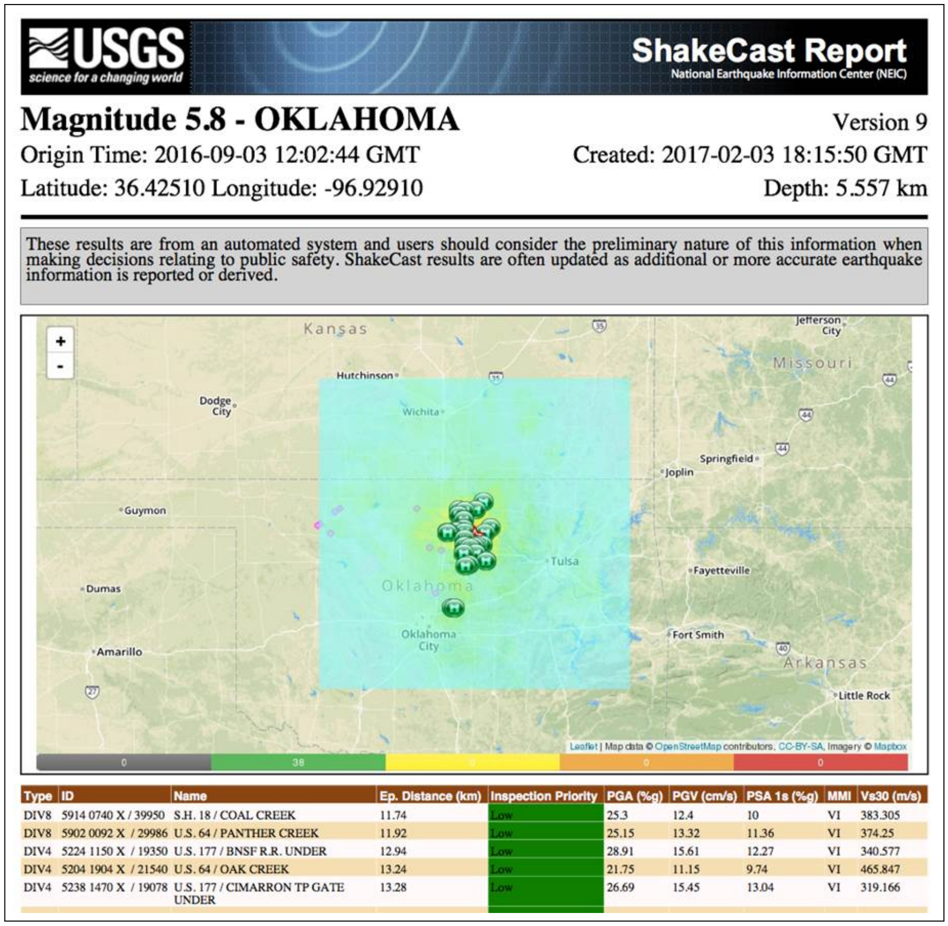
USGS science for a changing world

ShakeCast Report
National Earthquake Information Center (NEIC)

Magnitude 5.8 - OKLAHOMA Version 9

Origin Time: 2016-09-03 12:02:44 GMT Created: 2017-02-03 18:15:50 GMT

Latitude: 36.42510 Longitude: -96.92910 Depth: 5.557 km

These results are from an automated system and users should consider the preliminary nature of this information when making decisions relating to public safety. ShakeCast results are often updated as additional or more accurate earthquake information is reported or derived.

Type	ID	Name	Ep. Distance (km)	Inspection Priority	PGA (%g)	PGV (cm/s)	PSA 1s (%g)	MMI	Vs30 (m/s)
DIV8	5914 0740 X / 39950	S.H. 18 / COAL CREEK	11.74	Low	25.3	12.4	10	VI	383.305
DIV8	5902 0092 X / 29986	U.S. 64 / PANTHER CREEK	11.92	Low	25.15	13.32	11.36	VI	374.25
DIV4	5224 1150 X / 19350	U.S. 177 / BNSF R.R. UNDER	12.94	Low	28.91	15.61	12.27	VI	340.577
DIV4	5204 1904 X / 21540	U.S. 64 / OAK CREEK	13.24	Low	21.75	11.15	9.74	VI	465.847
DIV4	5238 1470 X / 19078	U.S. 177 / CIMARRON TP GATE UNDER	13.28	Low	26.69	15.45	13.04	VI	319.166

Figure 5.8: A screenshot from the emailed ShakeCast PDF.

2016). This means that using the interim protocol, about \$32,000 would have been saved on the M5.7 and about \$11,000 was saved for the M5.8. Using Shakecast would have saved ODOT an additional \$8,600 and \$7,100 for each of the earthquakes, respectively. Additionally, ODOT will save money by inspecting for fewer earthquakes. For instance in the year after the interim protocol was implemented (1 April 2016 – 31 March 2017), there were 13 earthquakes that would have required bridge inspections using the old protocol, 4* using the smart radii, and only 1 using ShakeCast. This resulted in ODOT saving \$15,700. Implementing ShakeCast over the same period would have saved an additional \$8,800.

*ODOT currently (24 April 2017) uses a modified version of the proposed smart inspection radii which lowers the inspection threshold from M4.7 to M4.4.

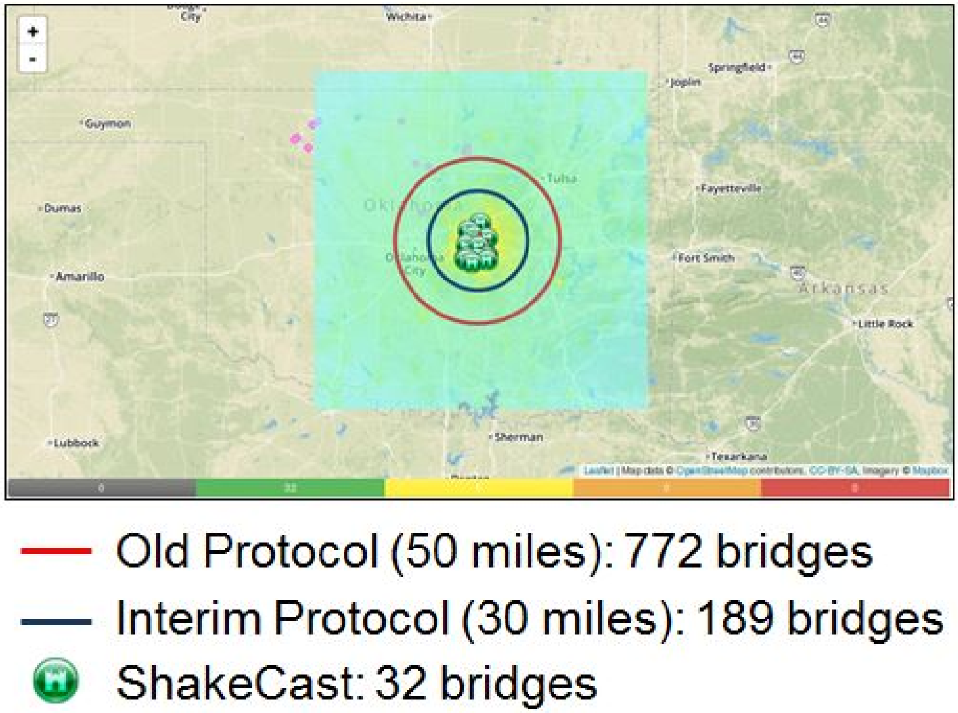

(a)

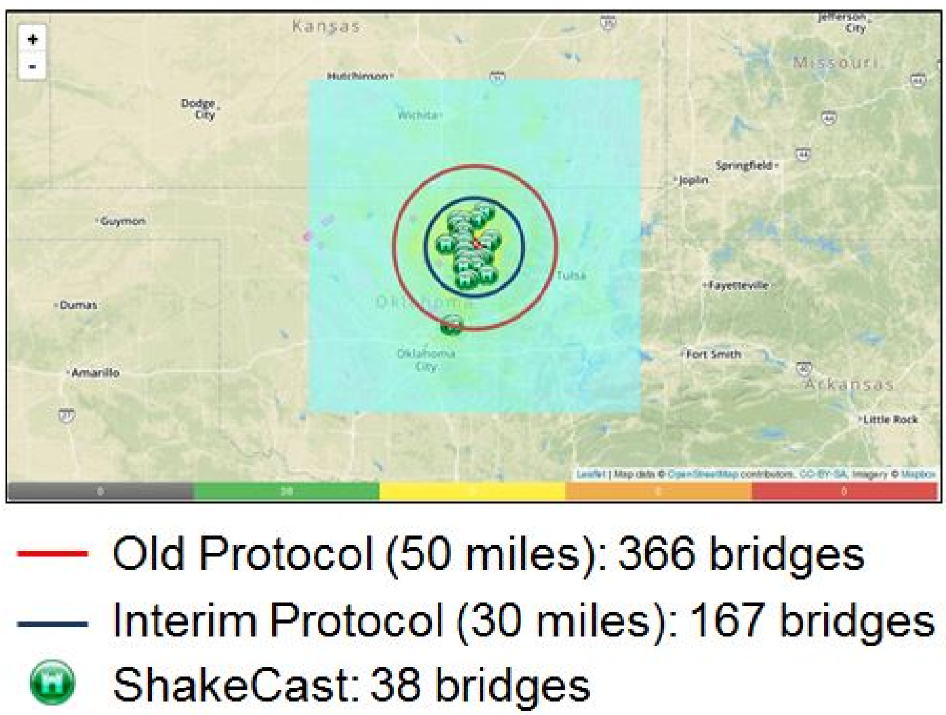

(b)

Figure 5.9: Comparison of the number of bridges to be inspected using the old radii, interim protocol and ShakeCast for the M5.7 (a) and M5.8 (b) earthquakes.

5.6 Summary

To develop ShakeCast-OK, HAZUS fragility curves were used with additional reductions for fracture critical, structurally deficient, and variable skew bridges. This chapter detailed the steps taken to populate the instance, as well as some of the customizations made to meet ODOT's requirements. After populating the instance, it was shown that by implementing ShakeCast significantly fewer inspections would be required as compared to the inspection radii because ShakeCast utilizes better data on the ground shaking levels, improving the potential for damage prediction capabilities.

Chapter 6

Summary, Conclusions, and Future Work

6.1 Summary and Conclusions

Since 2009, there has been a dramatic increase in the number of earthquakes in Oklahoma. Therefore, concern has arisen about how Oklahoma's infrastructure will handle the increased seismic demand. In particular, ODOT is concerned about their bridges' response to earthquakes and the potential for damage. This research sought to investigate these concerns. A summary of the areas of study and results is presented below.

The *smart inspection radii* presented in Chapter 2 incorporate both the demand on and capacity of Oklahoma bridges. Demand was quantified by the ground-motion intensity, in this case spectral acceleration at a period of 1.0 s (S_1). Predictions of S_1 were made using the Campbell (2003) ground-motion attenuation model calibrated with a bias factor correlated to actual seismic station data in Oklahoma. These predictions were adjusted by a site amplification factor (Site Class D). Inspection radii were set to be the largest distance from the epicenter at which demand (S_1) exceeds capacity characterized by fragility curves of bridges. A trigger value of $S_1 = 5.56\%g$ was selected as this capacity. The analysis showed that damage to bridges is unlikely (10% probability of slight damage) for earthquakes with a magnitude less than 4.6.

Chapter 3 compared measured Oklahoma seismic station data to the attenuation models found in the 2008 USGS seismic hazard map. Most of the attenuation models overpredicted Oklahoma ground motions; however, the Atkinson and Boore (2006) model had the best fit. Note that since the completion of this work, the USGS has switched from Campbell (2003) to Atkinson and Boore (2006) for ShakeMap ground-motion predictions in Oklahoma (USGS, 2016e). The response spectra calculated from seismic stations from the 3 September 2016 M5.8 Pawnee, Oklahoma earthquake were compared to the AASHTO spectra from those sites. Because the AASHTO design spectra are heavily based off of the Meers fault, the levels of shaking sometimes exceeded the design curves at locations farther from the Meers fault. Using slight fragility curve values calculated for previous Oklahoma earthquakes, it was found that the trigger value is slightly conservative.

Chapter 4 presents the results of a seismic response analysis for the Interstate 35 bridge over the Cimarron River located approximately 40 miles north of Oklahoma City in Logan County, Oklahoma. The purpose of this study was to improve the understanding of the seismic performance of this bridge and to determine the level of effort involved in performing a finite element analysis for a bridge structure. The results from this study can also be used to verify and adjust the fragility curve parameters needed for the development of ShakeCast–OK.

Seismic response analysis has shown that the potential for structural damage is low under both the 7% probability of exceedance in 75 years and 2% probability of exceedance in 50 years level events considered. The analysis indicates that the maximum curvature in the columns was about 25% of the yield curvature, and the maximum deflections in the bearings (< 0.5 in.) were all below the deflections prescribed for the slight damage state.

The final step in preparing ODOT for the emerging seismic threat was the development of Shakecast-OK (Chapter 5). To develop ShakeCast-OK, HAZUS fragility curves were used with additional reductions for fracture critical, structurally deficient, and variable skew bridges. After populating the instance, we found that ShakeCast-OK recommends significantly fewer inspections than the inspection radii because it has better data on the ground shaking levels.

6.2 Future Work

This research is a first step toward assessing the vulnerability of Oklahoma bridges to the emerging seismic threat. As a continuation of this research, the following are several areas which have the potential for further investigation:

- It has been demonstrated that current attenuation models do not accurately model Oklahoma ground motions. A new attenuation model should be developed to model the smaller magnitude earthquakes with high-frequency content.

- This research followed the current practice of only examining the effect of horizontal ground motions on bridges. However, more research is needed to examine how vertical ground motions attenuate and affect bridges.

- It was demonstrated that AASHTO design spectra can be exceeded by seismic events because these events are not occurring within close proximity to the Meers fault. Therefore, research needs to be conducted to determine how to incorporate induced seismicity into the AASHTO design spectra (Petersen et al., 2017).

- This research reduced fragility curves for structurally deficient and fracture critical bridges. Future research could perform a more rigorous analysis of the fragility curves for these bridges.

- This research looked at each earthquake that affected a bridge separately. However, the cumulative effect of repeated small earthquakes on a bridge should be examined to see if there is a potential for damage.

Chapter 7

Limitations

The conclusions and recommendations presented in this thesis were developed for the Oklahoma Department of Transportation (ODOT) by the researchers from the University of Oklahoma, in accordance with generally accepted civil and earthquake engineering principles and practices. This report was not prepared to be used by parties other than ODOT.

Earthquake ground motions are inherently uncertain, and observations of strong ground motions are limited in Oklahoma. Predictions for strong ground motions are based on available data and generally accepted attenuation models.

The fragility functions presented in this report are based on standard bridge models, adjusted for certain bridge characteristics. As a result, actual bridge fragilities may be different than those represented by the models and other interpretations are possible. Input parameters for the fragility functions were provided by ODOT, and we have assumed this information is true and accurate.

The conclusions and recommendations of Chapter 4 are for the seismic evaluation of structural aspects for the Interstate 35 Bridge over the Cimarron River located in Logan County, Oklahoma. The bridge was modeled assuming that its condition matched that described in the plans, which may differ from the actual condition of the bridge. Our evaluation was performed based on the plans and inspection reports provided by ODOT, and we have assumed this information is true and accurate.

Bibliography

AASHTO (2009). *Guide Specifications for LRFD Seismic Bridge Design*. Association of State Highway and Transportation Officials, Washington D.C.

ASCE/SEI 7-10 (2010). *Minimum design loads for buildings and other structures*. Structural Engineering Institute of ASCE, Reston, VA.

ATC (1985). "Earthquake damage evaluation data for California." *Report No. ATC-13*, Applied Technology Council.

ATC (1991). "Seismic vulnerability and impact of disruption of lifelines in the conterminous United States." *Report No. ATC-25*, Applied Technology Council.

Atkinson, G. M. and Boore, D. M. (2006). "Earthquake ground-motion predition equations for eastern North America." *Bulletin of the Seismological Society of America*, 96(6), 2181–2205.

Basoz, N. and Kiremidjian, A. S. (1997). "Evaluation of bridge damage data from the Loma Prieta and Northridge, CA earthquakes." *Report No. MCEER-98-0004*, MCEER.

Boore, D., Watson-Lamprey, J., and Abrahamson, N. (2006). "Orientation-independent measures of ground motion." *Bulletin of the Seismological Society of America*, 96(4A), 1502–1511.

Bosöz, N. and Mander, J. B. (1999). "Enchancement of the highway transportation lifeline module in HAZUS." *Report No. Final Pre-Publication Draft (#7)*, National Institute of Building Sciences (March).

Building Seismic Safety Council (2009). *NEHRP Recommended Provisions for Seismic Regulations for New Buildings and Other Structures*. FEMA, Washington, D.C.

Campbell, K. W. (2003). "Prediction of strong ground motion using the hybrid empirical method and its use in the development of ground-motion (attenuation) relations in eastern North America." *Bulletin of the Seimological Society of America*, 93(3), 1012–1033.

FEMA (2003). *Multi-hazard loss estimation methodology: Earthquake model: HAZUS MR4 technical manual*. Federal Emergency Management Agency, Washington, D.C.

FHWA (1995a). *Recording and Coding Guide for the Structure Inventory and Appraisal of the Nation's Bridges*. Office of Engineering Bridge Division, Federal Highway Administration, Washington, D.C., FHWA-PD-96-001 edition.

FHWA (1995b). *Seismic Retrofitting Manual for Highway Bridges*. Office of Engineering and Highway Operations R&D, Federal Highway Administration, McLean, VA, FHWA-RD-94-052 edition.

Frankel, A., Mueller, C., Barnhard, T., Perkins, D., Leyendecker, E., Dickman, N., Hanson, S., and Hooper, M. (1996). "National seismic-hazard maps: Documentation." *Report No. 96-532*, U.S. Department of the Interior U.S. Geological Survey.

Gellert, W., Gottwald, S., Hellwich, M., Kästner, H., and Kstner, H. (1989). *The VNR Concise Encyclopedia of Mathematics*. Van Nostrand Reinhold, New York, 2nd edition.

Hwang, H., Jernigan, J. B., and Lin, Y.-W. (2000). "Evaluation of seismic damage to Memphis bridges and highway systems." *Journal of Bridge Engineering*, 5(4), 322–330.

Jernigan, J. B. and Hwang, H. (2002). "Development of bridge fragility curves." *7th US National Conference on Earthquake Engineering*, EERI.

Kaka, S. I. and Atkinson, G. M. (2005). "Emprical ground-motion relations for ShakeMap applications in southeastern Canada and the northeastern United States." *Seismological Research Letters*, 76(2), 274–282.

Keranen, K. M., Savage, H. M., Abers, G. A., and Cochran, E. S. (2013). "Potentially induced earthquakes in Oklahoma, USA: Links between wastewater injection and the 2011 Mw 5.7 earthquake." *Geology*, 41(6), 699–702.

Liao, Y., Zafir, Z., and Radhakrishnan, K. (2016). "Site Specific Seismic Analysis: I-35/Cimarron River Bridge." *Report No. TUL16R37714*, Kleinfelder.

Liel, A. B. (2014). "Boulder EarthquakeCodes, <https://boulderearthquakecodes.wordpress.com/>. Accessed June 10, 2015.

Lin, K., Wald, D., Appel, V., and Turner, L. (2015). *ShakeCast V3 Operator's Technical Guide*.

Mander, J. B. (1999). "Fragility curve development for assessing the seismic vulnerability of highway bridges." *Research Progress and Accomplishments*, 89–98.

Mander, J. B., Priestley, M. J. N., and Park, R. (1988). "Observed stress-strain behavior of confined concrete." *Journal of Structural Engineering*, 114(8), 1827–1849.

Mazroi, A., Wang, L. R.-L., and Murray, T. M. (1982). “Effective coefficient of friction of steel bridge bearings.” *Report No. FSEL 12*, Fears Structural Engineering Laboratory.

McGarr, A., Bekins, B., Burkardt, N., Dewey, J., P. Earle, W. E., Ge, S., Hickman, S., Holland, A., E. Majer, J. R., and Sheehan, A. (2015). “Coping with earthquakes induced by fluid injection.” *Science*, 347(6224), 830–831.

McKenna, F. and Feneves, G. L. (2000). *Open System for Earthquake Engineering Simulation (OpenSees)*. Pacific Earthquake Engineering Research Center, University of California, Berkeley, CA, 2.5.0 edition.

Nielson, B. (2005). “Analytical fragility curves for highway bridges in moderate seismic zones.” Ph.D. thesis, Georgia Institute of Technology, Georgia Institute of Technology.

ODOT (2016). “ODOT firms up earthquake bridge inspection process.” *Press Release*, Oklahoma Department of Transportation, <https://www.ok.gov/triton/modules/newsroom/newsroom_article.php?id=277&article_id=19748>.

Owens, T. J., Crotwell, H. P., Groves, C., and Oliver-Paul, P. (2004). “SOD: Standing Order for Data.” *Seismological Research Letters*, 75, 515–520.

Padgett, J. E. and DesRoches, R. (2007). “Bridge functionality relationships for improved seismic risk assessment of transportation networks.” *Earthquake Spectra*, 23(1), 115–130.

Park, R., Priestley, M. J. N., and Gill, W. D. (1982). “Ductility of square-confined concrete columns.” *Journal of Structural Engineering*, 108(ST4), 929–950.

Petersen, M., Moschetti, M., Powers, P., Mueller, C., Haller, K., Frankel, A., Zeng, Y., Rezaeian, S., Harmsen, S., Boyd, O., Field, N., Chen, R., Rukstales, K., Luco, N., Wheeler, R., Williams, R., and Olsen, A. (2014). “Documentation for the 2014 update of the United States national seismic hazard maps.” *Report No. Open-File Report 2014-1091*, U. S. Geologic Survey.

Petersen, M. D., Mueller, C. S., Moschetti, M. P., Hoover, S. M., Rubinstein, J. L., Llenos, A. L., Michael, A. J., Ellsworth, W. L., McGarr, A. F., Holland, A. A., and Anderson, J. G. (2016). “2016 one-year seismic hazard forecast for the central and eastern United States from induced and natural earthquakes.” *Report No. Open-File Report 2016-1035*, U. S. Geologic Survey.

Petersen, M. D., Mueller, C. S., Moschetti, M. P., Hoover, S. M., Shumway, A. M., McNamara, D. E., Williams, R. A., Llenos, A. L., Ellsworth, W. L., Michael, A. J., Rubinstein, J. L., McGarr, A. F., and Rukstales, K. S. (2017). “2017 one-year seismic-hazard forecast for the central and eastern United States from induced and natural earthquakes.” *Seismological Research Letters*, 88(3).

Peterson, M. D., Frankel, A. D., Harmsen, S. C., Mueler, C. S., et al. (2008). "Documentation for the 2008 update of the United States national seismic hazard maps." *Report No. Open-File Report 2008-1128*, U.S. Geological Survey.

Robert, C. P. and Casella, G. (2004). *Monte Carlo Statistical Methods*. Springer, New York, NY, 2nd edition.

Schrage, I. (1981). "Anchoring of bearings by friction." *Special Publication SP70-12*, American Concrete Institute (ACI), Detroit, MI. 197–215.

Scott, B. D., Park, R., and Priestley, M. J. N. (1982). "Stress-strain behavior of concrete confined by overlapping hoops at low and high strain rates." *ACI Journal*, 79(1), 13–27.

Shinozuka, M., Feng, M. Q., Kim, H., Uzawa, T., and Ueda, T. (2003). "Statistical analysis of fragility curves." *Report No. MCEER-03-2002*, University of Southern California.

Silva, W., Gregor, N., and Darragh, R. (2002). "Development of regional hard rock attenuation relations for central and eastern North America." *Report No. ML042310569*, Pacific Engineering and Analysis, El Cerrito, CA.

Somerville, P., Collins, N., Abrahamson, N., Graves, R., and Saikia, C. (2001). "Ground motion attenuation relations for the central and eastern United States." *Report No. Award No. 99HQGR0098*, U. S. Geological Survey.

Tavakoli, B. and Pezeshk, S. (2005). "Empirical-stochastic ground-motion prediction for eastern North America." *Bulletin of the Seismological Society of America*, 95(6), 2283–2296.

Taylor, J., Celebi, M., Greer, A., Jampole, E., Masroor, A., Melton, S., Norton, D., Paul, N., Wilson, E., and Xiao, Y. (2017). "M5.0 Cushing, Oklahoma, USA earthquake on November 7, 2016." *Report No. Oklahoma-EERI-Recon-Report-2017-02-15-Finalized*, EERI.

Toro, G. R., Abrahamson, N. A., and Schneider, J. F. (1997). "Model of strong ground motions from earthquakes in the central and eastern North America: best estimates and uncertainties." *Seismological Research Letters*, 68, 41–57.

USDOT (2015). *National Bridge Inventory*. Federal Highway Administration, Washington, D.C.

USGS (2010). "Custon v_s^{30} mapping." *Earthquake Hazards Program*, U. S. Geological Survey, <http://earthquake.usgs.gov/hazards/apps/vs30/custom.php>. Accessed June 18, 2015.

USGS (2011). "ShakeMap archive." *Earthquake Hazards Program*, U. S. Geological Survey, <http://earthquake.usgs.gov/earthquakes/shakemap/list.php?x=1>. Accessed June 11, 2015.

USGS (2015a). "Cloud installation guide." *ShakeCast V3.0*, U. S. Geological Survey, <https://my.usgs.gov/confluence/display/ShakeCast/ShakeCast+V3.0>. Accessed October 26, 2015.

USGS (2015b). "Search earthquake archives." *Earthquake Hazards Program*, U. S. Geological Survey, <http://earthquake.usgs.gov/earthquakes/search/>. Accessed June 30, 2015.

USGS (2016a). "M 5.0 - 3km W of Cushing, Oklahoma." *ShakeMap*, U. S. Geological Survey, <http://earthquake.usgs.gov/earthquakes/eventpage/us100075y8#executive>. Accessed December 22, 2016.

USGS (2016b). "M 5.1 - 31km NW of Fairview, Oklahoma." *ShakeMap*, U. S. Geological Survey, <http://earthquake.usgs.gov/earthquakes/eventpage/us20004zy8#executive>. Accessed November 28, 2016.

USGS (2016c). "M 5.7 - Oklahoma." *ShakeMap*, U. S. Geological Survey, <http://earthquake.usgs.gov/earthquakes/eventpage/usp000jadn#executive>. Accessed November 28, 2016.

USGS (2016d). "M 5.8 - 14km NW of Pawnee, Oklahoma." *ShakeMap*, U. S. Geological Survey, <http://earthquake.usgs.gov/earthquakes/eventpage/us10006jxs#executive>. Accessed November 28, 2016.

USGS (2016e). "M 5.8 - 14km NW of Pawnee, Oklahoma." *Earthquake Hazards Program*, U. S. Geological Survey, <http://earthquake.usgs.gov/earthquakes/eventpage/us10006jxs#dyfi>. Accessed November 11, 2016.

USGS (2016f). "Magnitudes for oklahoma earthquakes shift upward." U. S. Geological Survey, <https://www.usgs.gov/news/magnitudes-oklahoma-earthquakes-shift-upward>. Accessed March 24, 2017.

USGS (2017a). "Induced earthquakes." *Earthquake Hazards Program*, U. S. Geological Survey, <https://earthquake.usgs.gov/research/induced/overview.php>. Accessed February 17, 2017.

USGS (2017b). "Software to download." *Earthquake Hazards Program*, U. S. Geological Survey, <https://earthquake.usgs.gov/research/software/shakecast.php>. Accessed February 17, 2017.

Vintzeleou, E. N. and Tassios, T. P. (1987). "Behavior of dowels under cyclic deformations." *ACI Structural Journal*, 84(1), 18–30.

Wald, D., Lin, K.-W., Porter, K., and Turner, L. (2008). "ShakeCast: Automating and improving the use of ShakeMap for post-earthquake decision-making and response." *Earthquake Spectra*, 24(2), 533–553.

Worden, B. C., Wald, D. J., Allen, T. I., Lin, K., Garcia, D., and Cua, G. (2010). "A revised ground-motion and intensity and interpolation scheme for ShakeMap." *Bulletin of the Seimological Society of America*, 100(6), 3083–3096.

Yang, C. S. W., Werner, S. D., and DesRoches, R. (2015). "Seismic fragility analysis of skewed bridges in the central southeastern United States." *Eng. Struct.*, (83), 116–128.

Zwillinger, D. (1995). *CRC Standard Matematical Tables and Formulae*. CRC Press, Boca Raton, FL.

Appendix A

Calculating Median S_1 for Standard Fragility Curves

A.1 Procedure

1. Identify the bridge's main span material (NBI item 43), skew angle (NBI item 34), number of spans (NBI item 45), year built (NBI item 27), and max span length (NBI item 48).
2. Use Table A.1 to find the bridge's HAZUS Class and to determine the K_{3D} equation number. First, find the row in the "Description" column which matches the bridge's information. If the bridge's max span length is greater than 150 m, it is HWB1 or HWB2. If the bridge only has one span, it is HWB3 or HWB4. If the bridge is not either of those, find rows in the table with the bridge's main span material in the "Description" column. For bridges made of steel, the max span length is also used to determine the bridge class (see the seventh column). After the section with the bridge's information is found, use the bridge's year built to find the HAZUS Class (NOTE: All Oklahoma bridges are Non-CA (see the third column)). Once the HAZUS Class is found, look through the row once more to confirm that each column in the row matches the bridge's information. The

bridge's K_{3D} equation number is found in the eighth column.

3. Use Table A.2 to calculate K_{3D} based on the equation number. N is the number of spans. If $N = 1$ and causes division by zero, use $K_{3D} = 1$. NOTE: HWB5, HWB12, and HWB24 use $K_{3D} = 1$ regardless of number of spans.
4. Calculate K_{skew} using the following formula, where α is the skew angle in degrees:

$$K_{skew} = \sqrt{\sin(90 - \alpha)} \tag{A.1}$$

Table A.1: HAZUS Bridge Classification Scheme (FEMA, 2003, Table 7.2).

CLASS	NBI Class	State	Year Built	# Spans	Length of Max. Span (meter)	Length less than 20 m	K_{3D} (See note below)	I_{shape} (See note below)	Design	Description
HWB1	All	Non-CA	< 1990		> 150	N/A	EQ1	0	Conventional	Major Bridge - Length > 150m
HWB1	All	CA	< 1975		> 150	N/A	EQ1	0	Conventional	Major Bridge - Length > 150m
HWB2	All	Non-CA	>= 1990		> 150	N/A	EQ1	0	Seismic	Major Bridge - Length > 150m
HWB2	All	CA	>= 1975		> 150	N/A	EQ1	0	Seismic	Major Bridge - Length > 150m
HWB3	All	Non-CA	< 1990	1		N/A	EQ1	1	Conventional	Single Span
HWB3	All	CA	< 1975	1		N/A	EQ1	1	Conventional	Single Span
HWB4	All	Non-CA	>= 1990	1		N/A	EQ1	1	Seismic	Single Span
HWB4	All	CA	>= 1975	1		N/A	EQ1	1	Seismic	Single Span
HWB5	101-106	Non-CA	< 1990			N/A	EQ1	0	Conventional	Multi-Col. Bent, Simple Support - Concrete
HWB6	101-106	CA	< 1975			N/A	EQ1	0	Conventional	Multi-Col. Bent, Simple Support - Concrete
HWB7	101-106	Non-CA	>= 1990			N/A	EQ1	0	Seismic	Multi-Col. Bent, Simple Support - Concrete
HWB7	101-106	CA	>= 1975			N/A	EQ1	0	Seismic	Multi-Col. Bent, Simple Support - Concrete
HWB8	205-206	CA	< 1975			N/A	EQ2	0	Conventional	Single Col., Box Girder - Continuous Concrete
HWB9	205-206	CA	>= 1975			N/A	EQ3	0	Seismic	Single Col., Box Girder - Continuous Concrete
HWB10	201-206	Non-CA	< 1990			N/A	EQ2	1	Conventional	Continuous Concrete
HWB10	201-206	CA	< 1975			N/A	EQ2	1	Conventional	Continuous Concrete
HWB11	201-206	Non-CA	>= 1990			N/A	EQ3	1	Seismic	Continuous Concrete
HWB11	201-206	CA	>= 1975			N/A	EQ3	1	Seismic	Continuous Concrete
HWB12	301-306	Non-CA	< 1990			No	EQ4	0	Conventional	Multi-Col. Bent, Simple Support - Steel
HWB13	301-306	CA	< 1975			No	EQ4	0	Conventional	Multi-Col. Bent, Simple Support - Steel
HWB14	301-306	Non-CA	>= 1990			N/A	EQ1	0	Seismic	Multi-Col. Bent, Simple Support - Steel
HWB14	301-306	CA	>= 1975			N/A	EQ1	0	Seismic	Multi-Col. Bent, Simple Support - Steel
HWB15	402-410	Non-CA	< 1990			No	EQ5	1	Conventional	Continuous Steel
HWB15	402-410	CA	< 1975			No	EQ5	1	Conventional	Continuous Steel
HWB16	402-410	Non-CA	>= 1990			N/A	EQ3	1	Seismic	Continuous Steel
HWB16	402-410	CA	>= 1975			N/A	EQ3	1	Seismic	Continuous Steel

CLASS	NBI Class	State	Year Built	# Spans	Length of Max. Span (meter)	Length less than 20 m	K_{3D} (notes below)	I_{shape} (notes below)	Design	Description
HWB17	501-506	Non-CA	< 1990			N/A	EQ1	0	Conventional	Multi-Col. Bent, Simple Support - Prestressed Concrete
HWB18	501-506	CA	< 1975			N/A	EQ1	0	Conventional	Multi-Col. Bent, Simple Support - Prestressed Concrete
HWB19	501-506	Non-CA	>= 1990			N/A	EQ1	0	Seismic	Multi-Col. Bent, Simple Support - Prestressed Concrete
HWB19	501-506	CA	>= 1975			N/A	EQ1	0	Seismic	Multi-Col. Bent, Simple Support - Prestressed Concrete
HWB20	605-606	CA	< 1975			N/A	EQ2	0	Conventional	Single Col., Box Girder - Prestressed Continuous Concrete
HWB21	605-606	CA	>= 1975			N/A	EQ3	0	Seismic	Single Col., Box Girder - Prestressed Continuous Concrete
HWB22	601-607	Non-CA	< 1990			N/A	EQ2	1	Conventional	Continuous Concrete
HWB22	601-607	CA	< 1975			N/A	EQ2	1	Conventional	Continuous Concrete
HWB23	601-607	Non-CA	>= 1990			N/A	EQ3	1	Seismic	Continuous Concrete
HWB23	601-607	CA	>= 1975			N/A	EQ3	1	Seismic	Continuous Concrete
HWB24	301-306	Non-CA	< 1990			Yes	EQ6	0	Conventional	Multi-Col. Bent, Simple Support - Steel
HWB25	301-306	CA	< 1975			Yes	EQ6	0	Conventional	Multi-Col. Bent, Simple Support - Steel
HWB26	402-410	Non-CA	< 1990			Yes	EQ7	1	Conventional	Continuous Steel
HWB27	402-410	CA	< 1975			Yes	EQ7	1	Conventional	Continuous Steel
HWB28										All other bridges that are not classified

Table A.2: Coefficients for Evaluating K_{3D} (FEMA, 2003, Table 7.3).

Equation	A	B	K_{3D}
EQ1	0.25	1	1 + 0.25 / (N – 1)
EQ2	0.33	0	1 + 0.33 / (N)
EQ3	0.33	1	1 + 0.33 / (N – 1)
EQ4	0.09	1	1 + 0.09 / (N – 1)
EQ5	0.05	0	1 + 0.05 / (N)
EQ6	0.20	1	1 + 0.20 / (N – 1)
EQ7	0.10	0	1 + 0.10 / (N)

5. Based on the HAZUS Class, use Table A.3 to find the $S_1 = S_a(1.0 \text{ sec})$ for damage functions due to ground shaking.
6. To calculate the new median S_1 for moderate, extensive, and complete damage states, multiply the respective value found in Table A.3 by K_{3D} and K_{skew}.
7. The median S_1 for slight damage state is taken to be $0.0833g$ for all bridge types (Section 2.2).

Table A.3: Damage Algorithms for Bridges (FEMA, 2003, Table 7.7).

	Sa [1.0 sec in g's] for Damage Functions due to Ground Shaking			
CLASS	**Slight**	**Moderate**	**Extensive**	**Complete**
HWB1	0.40	0.50	0.70	0.90
HWB2	0.60	0.90	1.10	1.70
HWB3	0.80	1.00	1.20	1.70
HWB4	0.80	1.00	1.20	1.70
HWB5	0.25	0.35	0.45	0.70
HWB6	0.30	0.50	0.60	0.90
HWB7	0.50	0.80	1.10	1.70
HWB8	0.35	0.45	0.55	0.80
HWB9	0.60	0.90	1.30	1.60
HWB10	0.60	0.90	1.10	1.50
HWB11	0.90	0.90	1.10	1.50
HWB12	0.25	0.35	0.45	0.70
HWB13	0.30	0.50	0.60	0.90
HWB14	0.50	0.80	1.10	1.70
HWB15	0.75	0.75	0.75	1.10
HWB16	0.90	0.90	1.10	1.50
HWB17	0.25	0.35	0.45	0.70
HWB18	0.30	0.50	0.60	0.90
HWB19	0.50	0.80	1.10	1.70
HWB20	0.35	0.45	0.55	0.80
HWB21	0.60	0.90	1.30	1.60
HWB22	0.60	0.90	1.10	1.50
HWB23	0.90	0.90	1.10	1.50
HWB24	0.25	0.35	0.45	0.70
HWB25	0.30	0.50	0.60	0.90
HWB26	0.75	0.75	0.75	1.10
HWB27	0.75	0.75	0.75	1.10
HWB28	0.80	1.00	1.20	1.70

A.2 Example

Given: I-40 over the Arkansas River (NBI 170510000000000): 10-span; 0 deg skew; Structure Length 606 m; Max Span Length 101 m; Year Built 1967; Main Span Material Steel Continuous.

1. Identify: main span material = steel continuous; skew angle = 0°; number of spans = 10; year built = 1967; max span length = 101 m
2. Use Table A.1 to determine K_{3D} equation number based on the HAZUS Class.

CLASS	NBI Class	State	Year Built	# Spans	Length of Max. Span (meter)	Length less than 20 m	K_{3D} (See note below)	I_{shape} (See note below)	Design	Description
HWB15	402-410	Non-CA	< 1990			No	EQ5	1	Conventional	Continuous Steel
HWB15	402-410	CA	< 1975			No	EQ5	1	Conventional	Continuous Steel
HWB16	402-410	Non-CA	>= 1990			N/A	EQ3	1	Seismic	Continuous Steel
HWB16	402-410	CA	>= 1975			N/A	EQ3	1	Seismic	Continuous Steel

3. Use Table A.2 to calculate K_{3D} based on the equation number.

Equation	A	B	K_{3D}
EQ5	0.05	0	1 + 0.05 / (N)

$$K_{3D} = 1 + \frac{0.05}{N} = 1 + \frac{0.05}{10} = 1.005$$

4. Calculate K_{skew}.

$$K_{skew} = \sqrt{\sin(90 - \alpha)} = \sqrt{\sin(90 - 0)} = 1$$

5. Based on the HAZUS Class, use Table A.3 to find the S_1 for damage functions due to ground shaking.

	Sa [1.0 sec in g's] for Damage Functions due to Ground Shaking				PGD [inches] for Damage Functions due to Ground Failure			
CLASS	Slight	Moderate	Extensive	Complete	Slight	Moderate	Extensive	Complete
HWB15	0.75	0.75	0.75	1.10	3.9	3.9	3.9	13.8

6. Calculate the new median S_1 for moderate, extensive, and complete damage

states.

$$S_1(\text{Moderate}) = 0.75 \times K_{3D} \times K_{skew} = 0.75 \times 1.005 \times 1 = 0.75375g$$

$$S_1(\text{Extensive}) = 0.75 \times K_{3D} \times K_{skew} = 0.75 \times 1.005 \times 1 = 0.75375g$$

$$S_1(\text{Complete}) = 1.10 \times K_{3D} \times K_{skew} = 1.10 \times 1.005 \times 1 = 1.1055g$$

7. Calculate the new median S_1 for slight damage state.

$$S_1(\text{Slight}) = 0.0833g$$

Appendix B

ODOT Priority Bridges

Table B.1: High priority bridges by NBI No. (#####0000000000).

High Priority Bridges										
00568	00645	15532	15794	15822	16105	16174	16585	18338	19484	20850
00623	10563	15554	15795	16078	16106	16175	16623	18774	19489	22405
00641	13652	15555	15810	16085	16108	16584	17897	19470	19624	

Table B.2: Medium-high priority bridges by NBI No. (#####0000000000).

Medium-High Priority Bridges										
00611	05023	09815	13099	14417	15542	15838	16149	16782	17340	18355
03429	05027	10075	13109	15115	15543	15843	16152	16783	17498	18460
03763	05446	10725	13117	15116	15567	16019	16153	16787	17499	19233
03788	05500	11104	13512	15120	15568	16025	16160	16998	17594	19346
03984	05504	12623	13658	15170	15760	16026	16161	17014	17898	19354
04072	05505	12624	13661	15178	15761	16041	16182	17022	17900	19355
04545	06548	12820	13677	15181	15770	16079	16586	17302	17901	19614
05017	07105	12835	14135	15364	15771	16080	16587	17303	17915	19776
05019	07113	12850	14204	15372	15803	16126	16588	17304	18054	21353
05022	07292	13094	14416	15541	15834	16148	16591	17332	18308	

Table B.3: Medium priority bridges by NBI No. (#####0000000000).

Medium Priority Bridges										
03164	09814	13082	14139	15190	15842	16566	17232	18057	18727	19800
03992	09824	13087	14171	15194	15850	16567	17235	18059	18728	19980
04179	10121	13100	14404	15195	16028	16575	17236	18060	18763	20305
05003	10539	13225	14450	15320	16029	16576	17253	18068	18764	20837
05029	10545	13503	14469	15321	16030	16636	17262	18075	19047	20848
05487	10715	13507	14477	15324	16031	16742	17283	18259	19049	20860
05518	10732	13653	14478	15325	16036	16743	17284	18272	19103	21023
06058	12404	13671	14479	15524	16083	16746	17285	18279	19106	21089
06285	12410	13680	14485	15525	16117	16788	17313	18307	19248	21104
06556	12470	13819	14493	15533	16118	16959	17465	18309	19256	21111
07122	12629	13820	14503	15534	16133	16960	17497	18310	19266	21120
07295	12630	13833	15090	15569	16134	16963	17548	18467	19471	21339
07314	12631	13847	15101	15588	16432	16965	17602	18484	19472	22033
07326	12644	13848	15102	15772	16433	16968	17885	18587	19473	22068
07327	12829	13867	15122	15773	16507	16983	17902	18588	19476	22095
09434	12849	13875	15123	15788	16508	17224	18042	18589	19477	22102
09435	13046	14097	15124	15802	16521	17225	18045	18590	19616	22103
09472	13062	14111	15125	15809	16522	17226	18046	18606	19627	28579
09502	13065	14117	15167	15821	16553	17227	18056	18607	19629	30028
09510	13077	14138								

Table B.4: Variable skew bridges by NBI No. (#####0000000000).

Variable Skew Bridges										
05046	15387	16633	17355	18127	18610	19508	20324	22097	25786	28576
12846	15564	16729	17890	18128	18772	19775	20857	22100	25823	28577
14110	15565	16738	18031	18136	18773	19786	20861	22421	25825	28686
14177	16159	16818	18061	18145	18791	19839	20862	22422	27524	28963
14185	16167	16967	18097	18146	19110	20002	21088	22423	27957	29153
14190	16604	16969	18102	18353	19111	20003	21090	24271	27958	29154
14203	16622	16977	18110	18356	19479	20005	22096	24969	28395	29155
15386	16629	16986	18118	18359	19507					

Appendix C

I-35/Cimarron River Bridge Supplemental Information

C.1 Superstructure Details

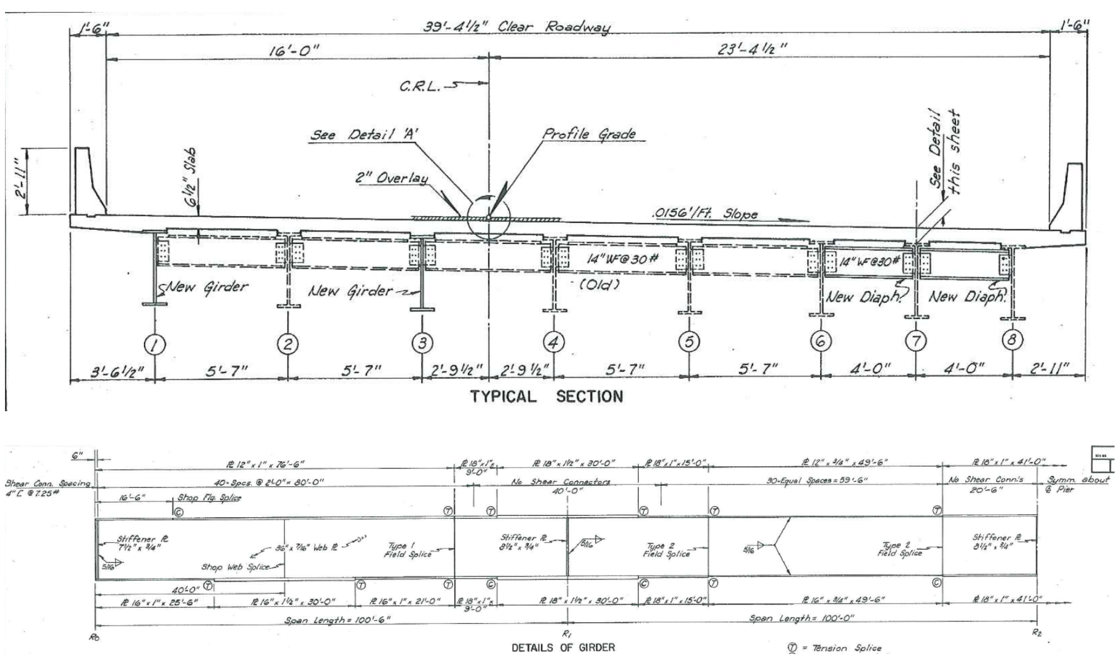

Figure C.1: Superstructure details (top) and girder details (bottom). Taken from Proj. No. I–FI–35–4(97)166 plans.

C.2 Substructure Details

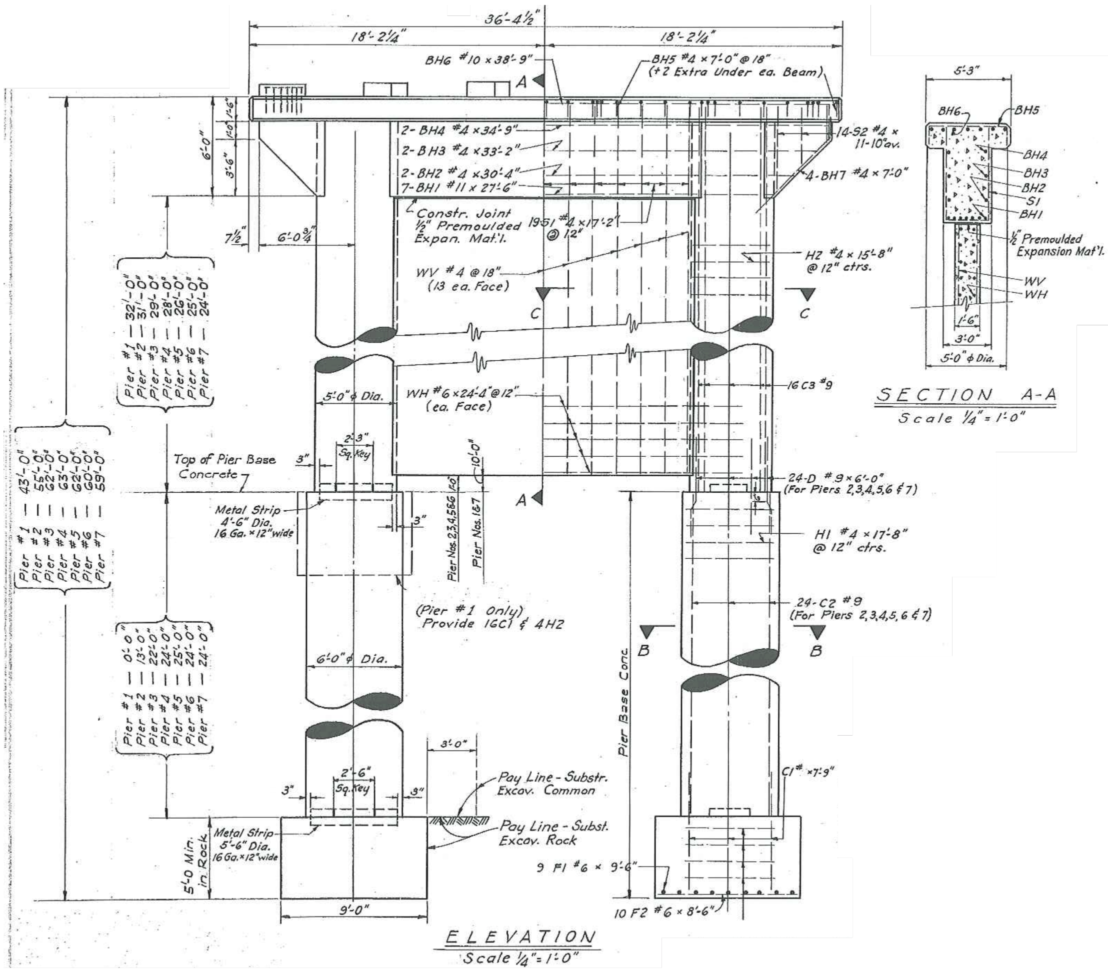

Figure C.2: Pier details. Taken from Proj. No. I–456–(16) plans.

C.3 Bearing Details

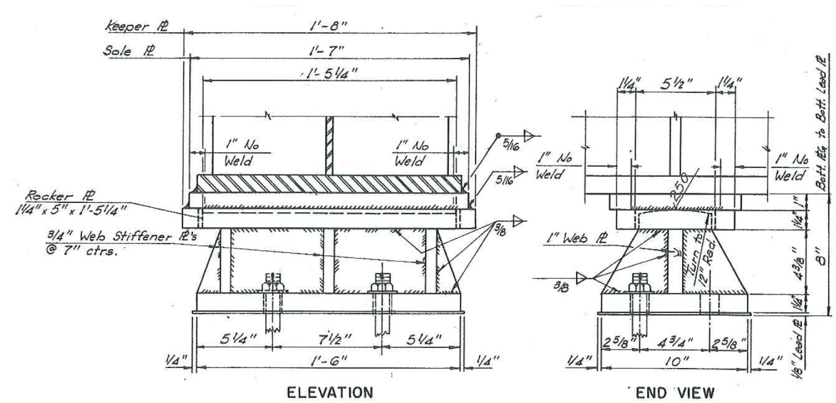

Figure C.1: High-type steel bearing details. Taken from Proj. No. I–FI–35–4(97)166 plans.

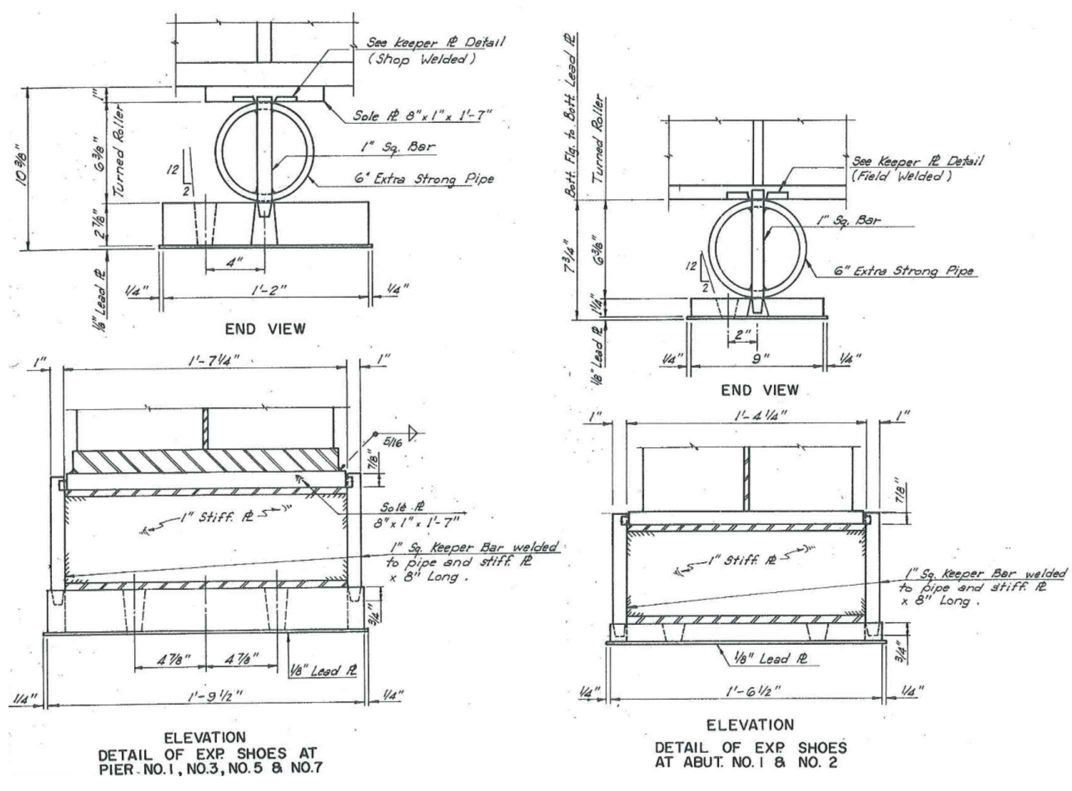

Figure C.2: Roller bearing details. Taken from Proj. No. I–FI–35–4(97)166 plans.

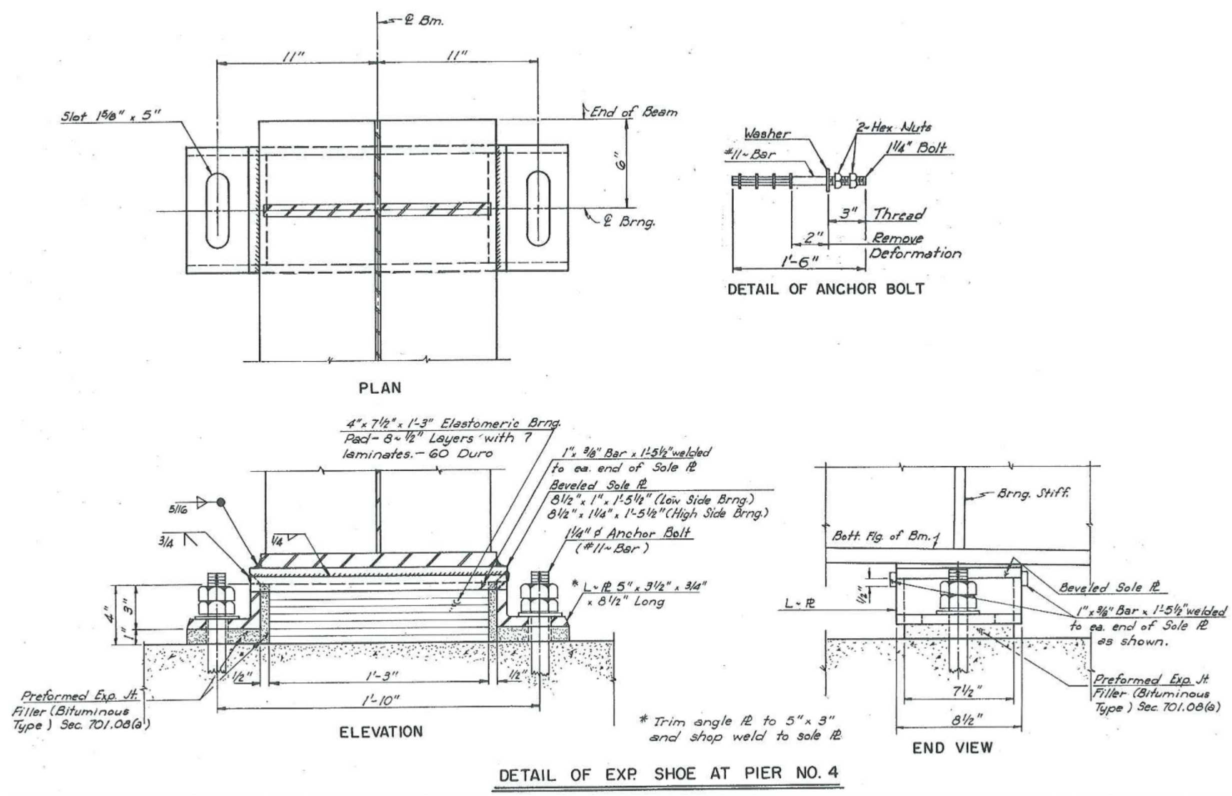

Figure C.3: Elastomeric bearing details. Taken from Proj. No. I–FI–35–4(97)166 plans.

C.4 Ground Motions

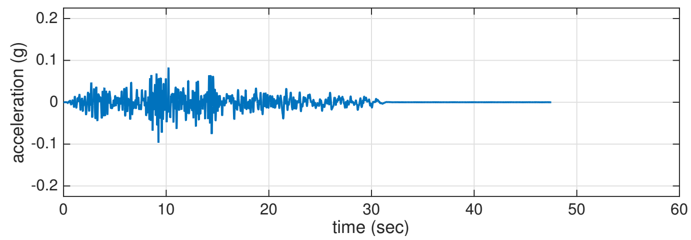

(a)

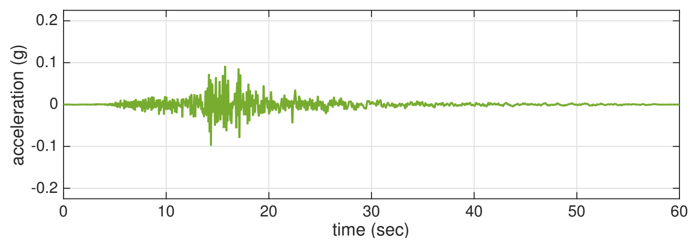

(b)

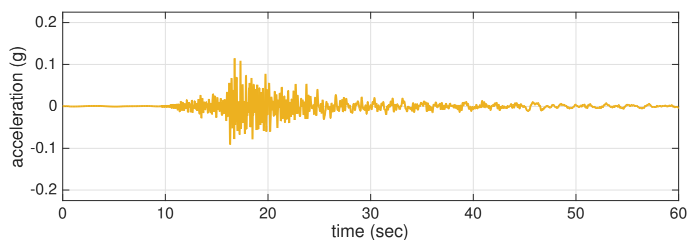

(c)

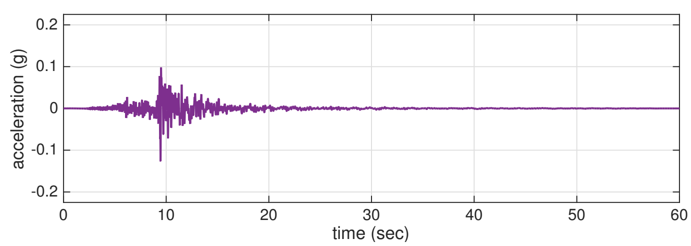

(d)

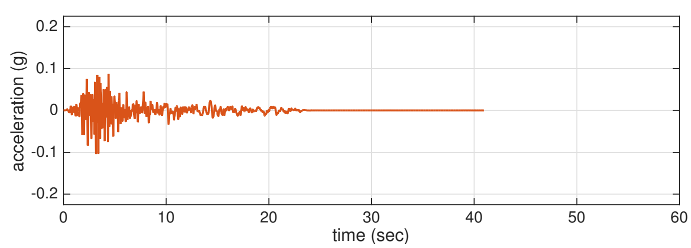

(e)

Figure C.1: Ground surface motions used in seismic analysis — 7% PE in 75 years: (a) 1980 Irpinia 294-TRC000; (b) 1991 Umbria Marche 4340-NZ1090; (c) 1991 Umbria Marche 4350-0000; (d) 2009 L'Aquila 4472-XTE; (e) 2009 L'Aquila 4503-YLN.

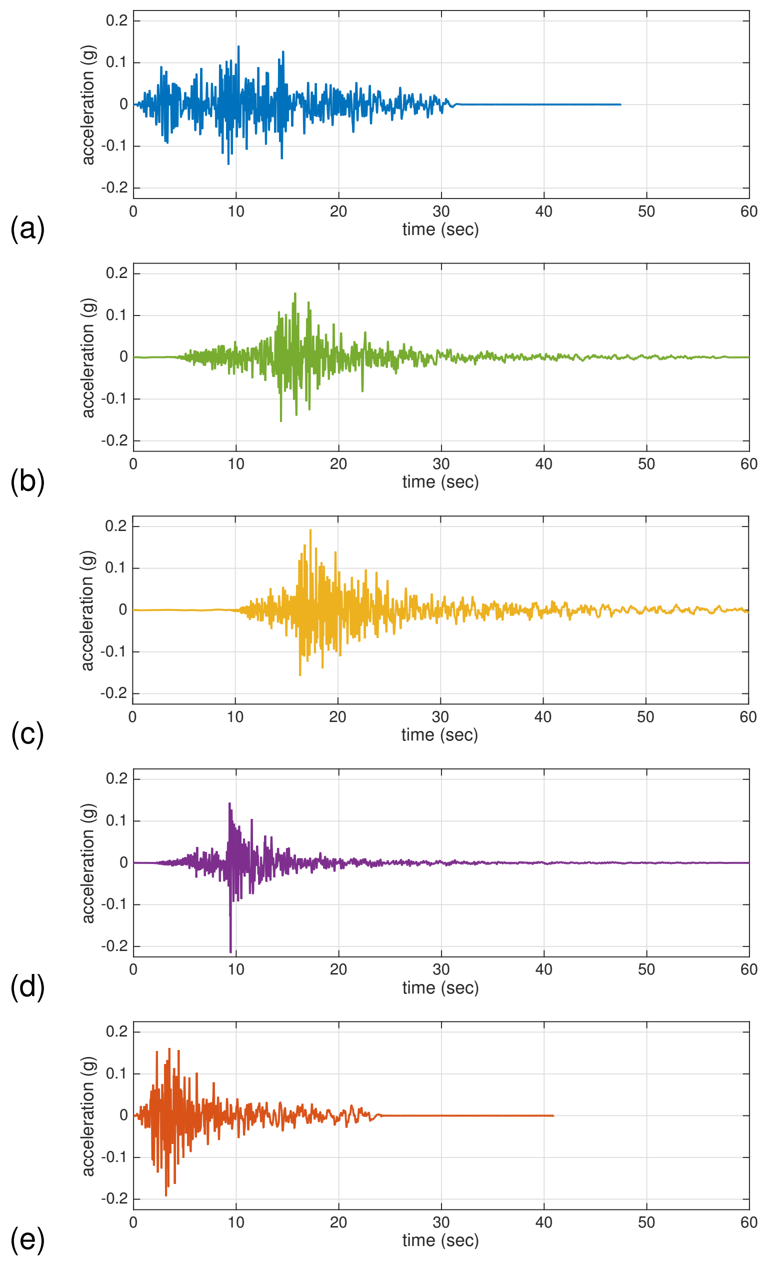

Figure C.2: Ground surface motions used in seismic analysis — 2% PE in 50 years: (a) 1980 Irpinia 294-TRC000; (b) 1991 Umbria Marche 4340-NZ1090; (c) 1991 Umbria Marche 4350-0000; (d) 2009 L'Aquila 4472-XTE; (e) 2009 L'Aquila 4503-YLN.

C.5 Nielson (2005) Limit States

Table C.1: Prescriptive limit states for bridge components taken from Nielson (2005).

Component	Slight	Moderate	Extensive	Complete
RC Column (μ_ϕ)	1.0	1.58	3.22	6.84
High-Type Steel Bearing – Fixed				
longitudinal (in.)	0.24	0.79	1.57	10.0
transverse (in.)	0.24	0.79	1.57	10.0
High-Type Steel Bearing – Rocker				
longitudinal (in.)	1.97	3.94	5.91	10.0
transverse (in.)	0.24	0.79	1.57	10.0
Expansion-type Elastomeric Bearing				
longitudinal (in.)	1.18	3.94	5.91	10.0
transverse (in.)	1.18	3.94	5.91	10.0

Table C.2: Bayesian updated limit states for bridge components taken from Nielson (2005).

Component	Slight	Moderate	Extensive	Complete
RC Column (μ_ϕ)	1.29	2.10	3.52	5.24
High-Type Steel Bearing – Fixed				
longitudinal (in.)	0.24	0.79	1.57	7.35
transverse (in.)	0.24	0.79	1.57	7.35
High-Type Steel Bearing – Rocker				
longitudinal (in.)	1.47	4.10	5.36	7.35
transverse (in.)	0.24	0.79	1.57	7.35
Expansion-type Elastomeric Bearing				
longitudinal (in.)	1.14	4.10	5.36	7.35
transverse (in.)	1.14	3.58	5.60	7.68